Interactions Between Soft Nanoparticles and Mammalian Cells

A Dissertation Presented for the

Doctor of Philosophy

Degree

The University of Tennessee, Knoxville

Mitchell Raith

May 2022

Acknowledgments

Firstly, I would like to thank my advisor Dr. Paul Dalhaimer. He gave me to the freedom to find and pursue my passions within his lab. I was able to grab the reigns and direct my research projects, which I know many graduate students don't have the privilege to do. I know he had to bestow a great amount of trust in me. I would also like to thank the other members of my committee, Dr. Steve Abel, Dr. Eric Boder, and Dr. Sherry Cox for providing support and advice. I would like to extend additional thanks Dr. Boder for allowing me the use of his lab facilities, especially the flow cytometer. Without this, I would not have been able to complete this work. I would like to thank Chris Carter for training me on mouse handling practices, and the rest of the OLAC staff for caring for my lab animals. The LAF staff, especially Peggy Kumbi-Bramble, were instrumental in allowing me to effectively manage time to complete my studies by helping to manage my mouse colony. I thank Tingting Xu for training me on the IVIS and trying her best to expedite repairs when I was the only user of the instrument during Covid lockdowns.

In the fall of 2017, I started my PhD journey full of confidence. I already had the better part of three years of laboratory experience under my belt and I thought I had all the tools at my disposal. I had no idea at the sacrifices my family would have to make in order to push me across the finish line. I would like to thank my mother Sylvia for always reminding me of the goal at hand and how much I had already accomplished in life. I would like to thank my father Robert for his constant words of encouragement. I would like to thank both my parents together for helping me buy a house, so I could keep my dog, Tucker. I don't know that I would have survived this process without Tucker by my side. I would like to thank my sister Kalie for her support and constant availability to talk. I would like to thank my cousin Olivia for sending me stupid jokes when she didn't know I needed a laugh. And finally, I

would like to thank my friend Dima for hearing every unfiltered thought from my brain for five years and never complaining.

Abstract

Nanoparticles have been of interest to the pharmaceutical industry since the 1980s. The first FDA approved nanoparticle-based therapies included liposomal anesthesia agents. Since then, the amount of FDA-approved nanoparticle therapies remains low. This is because nanoparticle-patient interactions can be very complex and are not well understood. Complicating factors also include increasing obesity rates among the patient population and many small animal pre-clinical trials are completed with healthy, lean animals. The biochemical differences between lean and obese patients prevents early studies from accurately predicting nanoparticle clinical behaviors. Many nanoparticles fail in trails. In this thesis, I aimed to uncover how nanoparticles interact with cells in an obesity-like environment.

I focused mainly on nanoparticles made from PEO-PBD di-block polymers (synthesized by Jimmy Mays's group in chemistry). The di-block polymers form into long, flexible cylinders ("filomicelles" or more generally, cylindrical nanoparticles (CNPs)). CNPs have been previously shown to have favorable circulation times compared to spherical nanoparticles, but I wanted to know how CNP enter cells. Surprisingly, this mechanism is not well-known for any nanoparticle. I focused on the potential interaction between CNPs and the major HDL receptor SR-BI. This was done with *in vitro* experiments involving the small molecule inhibition and binding site competition of SR-BI. *In vivo* experiments were also conducted with SR-BI deficient mice and co-injection of CNPs and HDL.

I then wanted to study the effects obesity would have on the pharmokinetics profile and biodistribution of CNPs and liposomal nanoparticles (LNPs). LNPs are the most used NPs in the clinic, so they provide a good control to evaluate the possibility of using CNPs in the clinic. I used a combination of controlled diet and leptin deficiency in mice to conduct this study. Interestingly, obesity caused CNPs to localize to the liver faster than lean controls. LNPs had the opposite effect. Further experimentation suggested this was due to different destination cell types within the liver for CNP vs LNP. In the third study, I developed a nucleic acid therapy that can trigger the lipolysis (breakdown) of neutral lipids in mammalian cells using a split-intein technology that I learned as an undergraduate.

Table of Contents

Chapter 1 Introduction 1
References 9
Chapter 2 Interaction between Polymeric Nanoparticles and SR-BI 13
Abstract 14
2.1 Introduction 15
2.2 Materials and Methods 17
2.3 Results 22
2.4 Discussion 32
2.5 Conclusions 36
References 38
Appendix 42
Chapter 3 Soft Nanoparticles and Obesity 52
Abstract 53
3.1 Introduction 55
3.2 Materials and Methods 57
3.3 Results 61
3.4 Discussion 70
3.5 Conclusion 75
References 76
Appendix 82
Chapter 4 Enhanced Lipid Droplet Degradation 83
Abstract 84
4.1 Introduction 85
4.2 Materials and methods 86
4.3 Results and Discussion 88
4.4 Conclusion 94
References 97
Chapter 5 Conclusions and Recommendations 99
Vita 102

Table of Figures

Figure 1. Properties of PEO-PBD filomicelles and PEO-PBD spheres used in this study. .. 21
Figure 2. Binding of PEO-PBD NPs to hHDL and rSR-BI.. 23
Figure 3. hHDL and BLT-1 block the uptake of PEO-PBD filomicelles by M1 and M2 murine macrophages.. 25
Figure 4. hHDL and BLT-1 block the uptake of PEO-PBD filomicelles by Idla7-SR-BI cells.. 27
Figure 5. PEO-PBD filomicelle localization to the liver drops when co-injected with hHDL in wild-type mice and in SCARB1-deficient mice when injected solitarily. 29
Figure 6. Entry of hHDL, filomicelles, and spheres into M1 and M2 murine macrophages and Idla7-SR-BI cells.. 31
Figure 7. SR-A does not play a role in PEO-PBD filomicelles uptake by Idla7-SR-BI cells. 33
Figure 8. Diet and leptin deficiency can be manipulated to generate mice of varying weights. 63
Figure 9. In vivo liver uptake of CNP is increased in Obese Mice.. 64
Figure 10. Effects of obesity on the 48hr distribution of CNPs and LNPs.. 66
Figure 11. Chemical Depletion of LSEC and KC..... 68
Figure 12. Obesity may promote biochemical factors that contribute to CNP localization to the liver.. 69
Figure 13. Toxicity Study of obese and lean mice injected with CNP or LNP..... 71
Figure 14. A Schematic illustrating the guidance of LDs to a lysosome with a split intein. .. 89
Figure 15. The Npu split intein causes LDs to be localized to lysosomes in NIH/3T3 fibroblasts. 90
Figure 16. LD numbers are reduced with the cleaving intein system, but not the non-cleaving intein system in NIH/3T3 fibroblasts. 93
Figure 17. Enhanced split intein mediated LD degradation is controllable with both system modification and chemical activation in NIH/3T3 fibroblasts. 95

Table of Supplementary Figures

Figure S 1. Confirmation of macrophage polarization by RT-PCR. 43
Figure S 2. Scatter plots for the PEO-PBD filomicelles-PKH67 histograms shown in Figure 3B for M1 murine macrophages..... 44
Figure S 3. Scatter plots for the PEO-PBD filomicelles-PKH67 histograms shown in Figure 3B for M2 murine macrophages..... 45
Figure S 4. Scatter plots for the PEO-PBD spheres-PKH67 histograms shown in Figure 3B for M1 murine macrophages.. 46
Figure S 5. Scatter plots for the PEO-PBD spheres-PKH67 histograms shown in Figure 3B for M2 murine macrophages. 47
Figure S 6. Scatter plots for the PEO-PBD filomicelles-PKH67 and PEO-PBD spheres-PKH67 histograms shown in Figure 3C,D for M1 and M2 murine macrophages.. 48
Figure S 7. Scatter plots for PEO-PBD filomicelles-PKH67 histograms shown in Figure 4B for Idla7-SR-BI cells..... 49
Figure S 8. Scatter plots for PEO-PBD spheres-PKH67 histograms shown in Figure 4B for Idla7-SR-BI cells. 50
Figure S 9. Scatter plots for PEO-PBD filomicelles-PKH67 histograms shown in Figure4D for Idla7 cells. 51
Figure S 10. Scatter plots for PEO-PBD spheres-PKH67 histograms shown in Figure 4D for Idla7 cells..... 45
Figure S 11. Scatter plots for PEO-PBD filomicelles-PKH26 and PEO-PBD spheres-PKH26 histograms shown in Figure 4F for Idla7 and Idla7-SR-BI cells.. 46
Figure S 12. Scatter plots for PEO-PBD filomicelles-PKH26 and PEO-PBD spheres-PKH26 histograms shown in Figure 4H. 47
Figure S 13. Scatter plots for hHDL shown in Figure 6D. 48
Figure S 14. Scatter plots for PEO-PBD filomicelles-PKH67 shown in Figure 6D..... 49
Figure S 15. Scatter plots for PEO-PBD spheres-PKH67 shown in Figure 6F.. 50
Figure S 16. Idla7-SR-BI cells do not express SR-A..... 51
Figure S 17. Spleen size and weights with varying mouse weights. 82

Chapter 1 Introduction

A major recent advancement in medicine has been the introduction of nanoparticle (NP) drug delivery systems [1]. We, as a field, are still determining the pros and cons of using NPs in mammalian patients to treat a variety of diseases. The effectiveness of NPs is typically measured by determining their biodistribution (also called “pharmacokinetic profile (PK)” when time is taken into consideration), their toxicity, and their ability to localize to the desired target(s) in the body. All three are interlinked.

The concept of using a nanoparticle in the clinic dates back to the mid-1980s [2]. The first conceptualized nanoparticle delivered drug therapies involved the use lipid nanoparticles called liposomes. Liposomes are synthetic vesicles constructed from a lipid bilayer. In the context of drug delivery, the vesicle encapsulates drug cargo. Possible cargo includes nucleic acids or crystallized small molecule drugs. Delivering a crystalized chemotherapy drug via liposomes is one way to replace traditional bulk phase chemotherapy. In traditional chemotherapy, an anticancer drug, such as paclitaxel, needs to be dissolved in aqueous solution via a co-solvent or solubilizing agent [3]. Co-solvents will enter the patients’ bloodstream after intravenous (IV) administration. Common co-solvents include castor oil, ethanol, and DMSO [4]. A NP encapsulates the drug soluble environment and protects from the aqueous phase [5]. Thus, NPs prevent the need to use co-solvents.

As of 2021, 32 nanoparticle drugs have been approved by the FDA. Of the 32 approved drugs, cancer treatments, anemia treatments, and imaging agents consist of the majority. Nanoparticles had remained relatively rare in the clinic until 2020, when the Moderna and Pfizer covid-19 vaccines received emergency clearance [2]. Both vaccines are an mRNA

vaccine delivered with a liposome [6]. Nanoparticles have now been used in hundreds of millions of patients on a global scale. I postulate this could lead to renewed enthusiasm for nanoparticle use in the clinic.

Although recent developments have led to massive administration of NPs for the first time, it can't be ignored only 32 NP drugs have FDA approval after forty years. This is because NPs continue to fail in clinical trials [7]. I suspect this is due to two main factors. Firstly, the interactions between a given nanoparticle and mammalian cells are complex and not well understood. Doxil is regarded as one of the most successful NP delivered cancer therapies, having been first brought to clinical trial in 1987 and receiving approval in 1995 [8]. Doxil is comprised of crystallized doxorubicin encapsulated with a PEGylated liposome. Twenty-seven years after FDA approval, the interaction between mammalian cells and liposomal doxorubicin is still being studied [9]. Characterizing cellular uptake of NPs may have been a neglected aspect of NP based therapy development. This creates need for further study of NP-cell interaction when developing new therapies. Secondly, I believe preclinical trials performed in animals with normal metabolic states may not provide accurate data to represent the target human population. The most used mouse strain for preclinical trials is C57BL/6 [10]. These mice are generally lean and exhibit normal metabolic states. This does not represent the patient population of the United States. Up to 2/3 of hospital patients are overweight or obese [11], meaning target patient population of a drug will likely not contain many lean patients. Using mice models that more accurately represent the obese human population may lead to increased NP usage in the clinic.

Here I considered 3 main themes. The first is determining how soft NPs with a poly-ethylene-glycol (PEG)-poly-ethylene-oxide (PEO)-based exterior enter different cell types. The second is how the pharmacokinetics of said NPs are affected by obesity – a major problem in our society - using a mouse model of obesity. Lastly, I investigated a potential nucleic acid intervention to treat obesity using a split intein system to return a patient to a normal metabolic state.

NPs are very broadly defined as any particle than can be synthesized on the sale of 1-500nm. Because of this, NPs come in a variety of chemistries and geometries, including lipid based, polymeric, metallic, and carbon-based NPs. NPs can be split into many categories, but one obvious distinction is hard vs. soft. Hard NPs, such as metal NPs, are cheaper to make but have a high propensity to bind high density lipoprotein (HDL) when injected into the patient blood stream [6,7]. A major function of HDL is to protect vasculature from plaque formation by transporting esterified cholesterol back to the liver from other tissues. HDL is then metabolized in the liver This is done by HDL docking on the major HDL receptor Scavenger Receptor Class B Type 1 (SR-BI) expressed in the liver [12]. Thus, metal NPs bound to HDL will be sequestered in the liver from their target cells. Polystyrene (PS) NPs also present issues for cell targeting. Antibodies present in human plasma harvested from polystyrene immune novel individuals bind PS NPs [13]. This is likely due to similar structures on PS NP surfaces and polysaccharides on the surface of pathogens. The resulting protein coat of antibodies triggers opsonization [14] and likely degradation of the NPs in macrophages. Strategies have been used to circumvent the immune novel PS opsonization phenomena through macrophage eradication using clodronate liposomes [11,12]. This can be problematic for clinical use because it leaves the patient immune

compromised for a few days post treatment [15]. As a result, targeting of NPs is imperative. This is expensive. I used soft NPs, such as those made from PEG/PEO (and lipids), for my experimentation. The bulky PEG/PEO blocks that make up these particles help prevent protein deposition (binding) due to steric hindrance. This includes lipoprotein.

It was previously discovered SR-BI was responsible for the importation of HDL-coated AgNPs, and to a lesser extent uncoated AgNPs in RAW 264.7 mouse macrophages [16]. This was thought to be an indirect effect caused by deactivation of the macrophages through the inhibition of SR-BI. Because polymeric NPs are unable to bind HDL, this suggests SR-BI would not affect the uptake of polymeric NPs, but the possibility of a direct interaction needed to be explored. Our lab investigated this possibility with the use of molecular dynamics simulations. Because SR-BI does not have a solved structure, we used the related protein SR-BII. Simulations showed that PEG was able to bind deep in the cholesterol transport tunnel of SR-BII, suggesting it may be possible for PEG and PEG based NPs to interact directly with SR-BI. *In vitro* experimentation showed that PEG could bind both isolated recombinant SR-BI and SR-BI on the surface of murine macrophages. PEG binding is a function of the aspect ratio of the NP. Cylindrical NPs (CNPs) had a stronger interaction with SR-BI compared to spheres, most likely due to cooperativity between one NP and several SR-BI molecules. *In vivo* experimentation confirmed the importance of SR-BI in removing CNPs from the blood stream via the liver. The liver has high levels of SR-BI expression in the body [17].

Obesity is an increasing health issue in western culture that spans much further than weight gain. Obesity alters the body's operation and causes many changes on the cellular level such as cell morphology [18], gene expression changes [19], free fatty acid (FFA) levels [20], and changes in cholesterol ratios [21]. There is a need to study NPs administered in obese animal models to predict this behavior in human patients. Our lab has previously studied the uptake of CNPs and carboxylated polystyrene (PS-COOH) beads in the major organs of mice. We have seen a decrease in filomicelle localization to the livers of obese mice in long term studies. Decreased signal could be due to a switch from liver sinusoid uptake of NPs to macrophages, leading to increased NP degradation and signal loss, or decreased overall uptake by liver cells due to fatty liver. The mechanism leading to cellular uptake in the liver needed to be investigated further to determine the fate of NPs in obese models. For these experiments I choose to focus on PEGylated CNPs. PEGylated liposomes were used for controls because they resemble the FDA approved drug Doxil.

Within the liver, resident macrophages, or Kupffer Cells (KCs) [22], and Liver Sinusoidal Endothelial Cells (LSECs) [23] [24] are the two main cells types responsible for removing foreign bodies such as NPs from circulation. Through chemical depletion, I show that KCs are the predominant cell type for removing CNPs from circulation. Both previously published data [25] and my experimentation with spherical NPs (SNPs) show that both KC and LSEC lead to liver localization for IV injected SNPs. The onset of obesity increases the number of macrophages in the liver [26] while incurring LSEC injury [27]. Through an *in vivo* PK study, I saw that obese mice localize CNPs to the liver faster than lean animals while lipid-based SNPs are localized to the liver slower. I postulated this was due to increased KC and deceased LSEC activity in obese mice.

A concern with administering nanoparticles to any patient, but especially obese patients, will be the toxicity of the NPs. Through cytokine analysis done on obese and lean mice, it was determined these NPs pose no major toxicity threat and are reversing some of the inflammatory response associated with obesity. Thus, potentially improving the health of the patient.

Although the ideal scenario is to mold treatment types to patient condition, especially in the rise of personalized medicine[28], there does exist the possibility to return patients to a normal metabolic state before treatment with NPs. Increasing obesity in western culture [29] suggests this will require the use of interventional medicine. Here, I show one possible technique to decrease the number of lipid droplets (LDs) within a murine fibroblast. One native pathway to digest LDs is chaperone mediated autophagy (CMA) [30]. CMA was augmented with a spit intein. Natively, CMA involves chaperone protein (Hsc70) mediated transport of LDs to the lysosome for degradation. I used a split intein expressed on both the LD and the lysosome via LD bound PLIN2 and lysosome bound LAMP2A. The intein system was able to traffic LDs to the lysosomal surface. Mild stress was then able to trigger rapid decrease of the LDs.

In total, I have proved that SR-BI drives the liver uptake of CNPs. SR-BI interaction, along with shape preferences of KCs and LSECs, drives CNPs to KCs over LSECs This will cause challenges for the use of CNPs in the clinic. As obesity both increases SR-BI liver

expression and liver macrophage activity, the circulation time of CNPs is shorter in obese mice.

References

1. Rudramurthy, G.R. and M.K. Swamy, *Potential applications of engineered nanoparticles in medicine and biology: an update.* J Biol Inorg Chem, 2018. **23**(8): p. 1185-1204.
2. Anselmo, A.C. and S. Mitragotri, *Nanoparticles in the clinic: An update post COVID-19 vaccines.* Bioeng Transl Med, 2021: p. e10246.
3. Veltkamp, S.A., et al., *A novel self-microemulsifying formulation of paclitaxel for oral administration to patients with advanced cancer.* Br J Cancer, 2006. **95**(6): p. 729-34.
4. Millard, J., F. Alvarez-Nunez, and S. Yalkowsky, *Solubilization by cosolvents. Establishing useful constants for the log-linear model.* Int J Pharm, 2002. **245**(1-2): p. 153-66.
5. Geng, Y., et al., *Shape effects of filaments versus spherical particles in flow and drug delivery.* Nat Nanotechnol, 2007. **2**(4): p. 249-55.
6. Hou, X., et al., *Lipid nanoparticles for mRNA delivery.* Nat Rev Mater, 2021. **6**(12): p. 1078-1094.
7. Hernandez-Camarero, P., et al., *Clinical failure of nanoparticles in cancer: mimicking nature's solutions.* Nanomedicine (Lond), 2020. **15**(23): p. 2311-2324.
8. Barenholz, Y., *Doxil(R)--the first FDA-approved nano-drug: lessons learned.* J Control Release, 2012. **160**(2): p. 117-34.
9. Kullenberg, F., et al., *In Vitro Cell Toxicity and Intracellular Uptake of Doxorubicin Exposed as a Solution or Liposomes: Implications for Treatment of Hepatocellular Carcinoma.* Cells, 2021. **10**(7).

10. Otto, G.P., et al., *Clinical Chemistry Reference Intervals for C57BL/6J, C57BL/6N, and C3HeB/FeJ Mice (Mus musculus).* J Am Assoc Lab Anim Sci, 2016. **55**(4): p. 375-86.
11. Alexopoulos, A.S., et al., *Impact of obesity on hospital complications and mortality in hospitalized patients with hyperglycemia and diabetes.* BMJ Open Diabetes Res Care, 2016. **4**(1): p. e000200.
12. Ouimet, M., J. Barrett Tessa, and A. Fisher Edward, *HDL and Reverse Cholesterol Transport.* Circulation Research, 2019. **124**(10): p. 1505-1518.
13. Lundqvist, M., et al., *Nanoparticle size and surface properties determine the protein corona with possible implications for biological impacts.* Proceedings of the National Academy of Sciences, 2008. **105**(38): p. 14265.
14. Pereira, H.A. and C.S. Hosking, *The role of complement and antibody in opsonization and intracellular killing of Candida albicans.* Clinical and experimental immunology, 1984. **57**(2): p. 307-314.
15. Kameka, A.M., et al., *Clodronate treatment significantly depletes macrophages in chickens.* Canadian journal of veterinary research = Revue canadienne de recherche veterinaire, 2014. **78**(4): p. 274-282.
16. Aldossari, A.A., et al., *Scavenger receptor B1 facilitates macrophage uptake of silver nanoparticles and cellular activation.* Journal of Nanoparticle Research, 2015. **17**: p. 313.
17. Leiva, A., et al., *Mechanisms regulating hepatic SR-BI expression and their impact on HDL metabolism.* Atherosclerosis, 2011. **217**(2): p. 299-307.
18. Covington, J.D., et al., *Intramyocellular Lipid Droplet Size Rather Than Total Lipid Content is Related to Insulin Sensitivity After 8 Weeks of Overfeeding.* Obesity (Silver Spring), 2017. **25**(12): p. 2079-2087.

19. Keller, M.P. and A.D. Attie, *Physiological insights gained from gene expression analysis in obesity and diabetes.* Annual review of nutrition, 2010. **30**: p. 341-364.
20. Boden, G., *Obesity and free fatty acids.* Endocrinology and metabolism clinics of North America, 2008. **37**(3): p. 635-ix.
21. Klop, B., J.W.F. Elte, and M.C. Cabezas, *Dyslipidemia in obesity: mechanisms and potential targets.* Nutrients, 2013. **5**(4): p. 1218-1240.
22. Sadauskas, E., et al., *Kupffer cells are central in the removal of nanoparticles from the organism.* Part Fibre Toxicol, 2007. **4**: p. 10.
23. Liu, Q., et al., *Use of Polymeric Nanoparticle Platform Targeting the Liver To Induce Treg-Mediated Antigen-Specific Immune Tolerance in a Pulmonary Allergen Sensitization Model.* ACS Nano, 2019. **13**(4): p. 4778-4794.
24. Yu, X., et al., *Immune modulation of liver sinusoidal endothelial cells by melittin nanoparticles suppresses liver metastasis.* Nat Commun, 2019. **10**(1): p. 574.
25. Park, J.K., et al., *Cellular distribution of injected PLGA-nanoparticles in the liver.* Nanomedicine, 2016. **12**(5): p. 1365-74.
26. Remmerie, A., L. Martens, and C.L. Scott, *Macrophage Subsets in Obesity, Aligning the Liver and Adipose Tissue.* Front Endocrinol (Lausanne), 2020. **11**: p. 259.
27. Miyao, M., et al., *Pivotal role of liver sinusoidal endothelial cells in NAFLD/NASH progression.* Lab Invest, 2015. **95**(10): p. 1130-44.
28. Valent, P., et al., *Precision Medicine in Hematology 2021: Definitions, Tools, Perspectives, and Open Questions.* Hemasphere, 2021. **5**(3): p. e536.
29. Jaacks, L.M., et al., *The obesity transition: stages of the global epidemic.* Lancet Diabetes Endocrinol, 2019. **7**(3): p. 231-240.

30. Kaushik, S. and A.M. Cuervo, *Degradation of lipid droplet-associated proteins by chaperone-mediated autophagy facilitates lipolysis.* Nat Cell Biol, 2015. **17**(6): p. 759-70.

Chapter 2 Interaction between Polymeric Nanoparticles and SR-BI

Elongated PEO-based nanoparticles bind the high-density lipoprotein (HDL) receptor scavenger receptor class B I (SR-BI)

Mitch Raith [a], Sarah J. Kauffman [b], Monireh Asoudeh [a], Jennifer A. Buczek [c], Nam-Goo Kang [d], Jimmy W. Mays [d], Paul Dalhaimer [a,e,*]

[a] Department of Chemical and Biomolecular Engineering, University of Tennessee, Knoxville, TN 37996, United States of America

[b] Department of Microbiology, University of Tennessee, Knoxville, TN 37996, United States of America

[c] College of Veterinary Medicine, University of Tennessee, Knoxville, TN 37996, United States of America

[d] Department of Chemistry, University of Tennessee, Knoxville, TN 37996, United States of America

[e] Department of Biochemistry, Cellular, and Molecular Biology, University of Tennessee, Knoxville, TN 37996, United States of America

[*] Correspondence: pdalhaim@utk.edu

Abstract

Targeting cell-surface receptors with nanoparticles (NPs) is a crucial aspect of nanomedicine. Here, we show that soft, flexible, elongated NPs with poly-ethylene-oxide (PEO) exteriors and poly-butadiene (PBD) interiors – PEOPBD filomicelles - interact directly with the major high-density lipoprotein (HDL) receptor and SARS-CoV-2 uptake factor, SR-BI. Filomicelles have a ~ 6-fold stronger interaction with reconstituted SR-BI than PEO-PBD spheres. HDL, and the lipid transport inhibitor, BLT-1, both block the uptake of filomicelles by macrophages and Idla7 cells, the latter are constitutively expressing SR-BI (Idla7-SR-BI). Co-injections of HDL and filomicelles into wild-type mice reduced filomicelle signal in the liver and increased filomicelle plasma levels. The same was true with SCARB1− /− mice. SR-BI binding is followed by phagocytosis for filomicelle macrophage entry, but only SR-BI is needed for entry into Idla7-SR-BI cells. PEO-PBD spheres did not interact strongly with

SR-BI in the above experiments. The results show elongated PEO-based NPs can bind cells via cooperativity among SR-BI receptors on cell surfaces.

2.1 Introduction

Given the prevalence of metabolic disorders such as obesity [1], there is great need to target surface receptors on cells that are involved in mammalian-wide lipid and cholesterol homeostasis using nanoparticles (NPs). Lipoproteins play a major role in controlling the distribution of neutral lipids and cholesterol. A subset of lipoproteins – mostly high-density lipoprotein (HDL) - bind scavenger receptor class B I (SRBI) [2]. HDL transports cholesterol from tissues and delivers it to SR-BI on the liver and on macrophages [3–6]. SR-BI is also an entry point for certain pathogens [7]. Hepatitis C virus uses SR-BI to enter cells [8,9], as does SARS-CoV-2 [10]. These viruses bind HDL, which most likely guides their cellular entry [10,11]. Thus, SR-BI is an attractive NP target for modulating metabolic imbalances and for combating certain pathogen infections. The issue is how to target SR-BI. In theory this can be done by attaching an SR-BI-targeting ligand to the exterior of the NP. However, the mechanistic molecular interactions between HDL and SRBI are unknown, thus negating the identification of a potential ligand that can be conjugated to a NP. Alternatively, lipoprotein can be modified and used to deliver drugs. However, this can be expensive and time consuming [12]. A cost-effective and biocompatible approach to targeting this crucial receptor is needed.

Here, we show that soft poly-ethylene-oxide (PEO)ylated NPs (synonymous with poly-ethylene-glycol (PEG)ylated NPs) with polybutadiene (PBD) cores that are elongated in one dimension – PEO-PBD filomicelles – achieve the above goals with respect to binding SR-BI and being internalized by cells expressing SR-BI. PEO-PBD filomicelles bind reconstituted

human SR-BI (rSR-BI) in pull down experiments. PEO-PBD filomicelle uptake by M1 and M2 murine macrophages is blocked by human HDL (hHDL) and by the small blocks-lipid-transport molecule, BLT-1, in co-incubation titration experiments. These results also hold for Idla7 cells constitutively expressing SR-BI (Idla7-SR-BI) cells. PEO-PBD filomicelles increase the expression level of SR-BI in M1 and M2 murine macrophages. In vivo, co-injections of PEO-PBD filomicelles and hHDL into wild-type mice resulted in a ~ 2-fold decrease in PEO-PBD filomicelle localization to the liver. This was also true when PEO-PBD filomicelles were injected solitarily into SR-BI-deficient mice (SCARB1− /−). PEO-PBD filomicelle levels in the plasma were increased over controls in both experiments. By using a panel of inhibitors for classic NP entry points into cells, we show that Polyinosinic (PI) acid, an SR-BI blocker, negates the uptake of PEO-PBD filomicelles by Idla7-SRBI cells. PEO-PBD filomicelles enter M1 and M2 murine macrophages by a combination of SR-BI binding and subsequent phagocytosis. In the above experiments, spherical PEO-PBD analogs did not have appreciable interactions with SR-BI. Thus, elongated filomicelles that have a PEO exterior have excellent potential in metabolic applications. These include modulating reverse cholesterol transport by increasing expression levels of SR-BI to increase uptake of HDL, delivering active agents to cells through SR-BI, and blocking SR-BI in certain situations such as foam cell progression. Blocking SR-BI with PEO-PBD filomicelles could also be a strategy for reducing pathogen uptake. Our results point to a new paradigm for binding and entering cells that express SR-BI, a major player in metabolic homeostasis and pathogenesis.

2.2 Materials and Methods

2.2.1. Nanoparticles

PEO_{56}-PBD_{46} diblock copolymers (filomicelles) were synthesized according to the methods of Ref. 13. PEO_{132}-PBD_{69} diblock copolymers (spheres) were a gift from Dr. Frank S. Bates (Univ. of Minnesota). NPs were formed at 10 mg/ml copolymer using film rehydration with phosphate buffered saline (PBS) as the aqueous buffer as described previously [14]. 50 nm spherical carboxylated polystyrene (PS)-COOH NPs were purchases from Bangs Labs (#PC2002). Nanoparticles were stained with hydrophobic PKH-26/67 or near-infrared (NIR) dyes and dialyzed overnight into PBS [15]. The PBS was changed three times.

2.2.2. SEM imaging

200 mesh copper grids with a thin carbon film were made to be hydrophilic by placing the grid with film in weak plasma for 30s. The grid with carbon film was then floated on a small drop of sample for 1 min, excess sample was quickly removed by touching the edge of the grid to a piece of filter paper. The grid with sample was washed with water then stained with 1% uranyl acetate, after 1 min excess stain was removed by touching the edge of the grid to a piece of filter paper. The images were taken by ZEISS LIBRA 200 HT FE and analyzed by ImageJ (Fiji).

2.2.3. Binding assays

hHDL was purchased from Lee BioSolutions (#361–10). The solution contained 3320 mg/dL total cholesterol, 1350 mg/dL triglyceride, and 3070 hHDL cholesterol. Electrophoresis (Helena QuickGel) preformed at Lee BioSolutions showed one major band corresponding to ApoA-I. PSCOOH NPs were pelleted by centrifugation. Filomicelles were pelleted using

immune precipitation. Briefly, filomicelles and hHDL or rSR-BI (R and D systems; #8114-SRB) were mixed for 3 h at 4 ◦C. An antibody for PEG (Abcam; #ab133471) was then added and the mixed was mixed at 4 ◦C for an additional hour. Agarose Protein L beads (Santa Cruz Bio; #sc-500,779) were then added for an additional hour. At this point filomicelles with bound Apo-AI were pelleted. The amount of unbound Apo-AI in the supernatant was quantified by spectroscopy (Nanodrop). The amount of Apo-AI bound to the filomicelles and spheres was calculated by subtracting the amount of Apo-AI in the supernatant from the total amount used in the assay.

2.2.4. Mammalian cell culture

M0 RAW 264.7 macrophages (ATCC; #TIB-71) were polarized into M1-like macrophages by adding 20 ng/ml of IFN-γ (PeproTech; #315–05) or into M2-like macrophages by adding 10 ng/ml each of IL-4 (PeproTech; #214–14) and IL-13 (PeproTech; #210–13) for 48 h [16]. Increased expression of IL-12 (M1) and IL-10 was confirmed using standard RT-PCR techniques (Fig. S1). Macrophages were maintained at 5% CO2 and 37 ◦C in DMEM supplemented with 10% FBS and 1% penicillin-streptomycin. Idal7 and Idal7-SR-BI cells were provided by Dr. Monty Krieger (MIT). Idal7 cells were maintained at 5% CO2 and 37 ◦C in F-12 K supplemented with 10% FBS and 1% penicillin-streptomycin. Idal7-SR-BI also had 200 ng/ml G418 in the media.

2.2.5. In vitro experiments

18 h prior to experiments, cells were seeded in a 24 well plate. 70–90% confluence was targeted at the start of the experiment. NPs were added to a final concentration of 400 μg/ml. Plates were swirled to mix. After 2 h, the media was removed, the cells were washed 3× times with PBS and imaged to visualize NP content with an EVOS FL Cell Imaging

System (Thermo). Cells were then trypsinized and two volumes of FACSmax (ASMBIO) buffer was added before the cells were aspirated. Cells were then quantitatively analyzed with an Accuri C6 flow cytometer (BD Biosciences). hHDL was added simultaneously with the NPs to the final concentrations stated. Plates were swirled to mix and incubated for 2 h. Analysis was done as described above. The SR-BI-GFP plasma was a gift from Dr. Sergio Grinstein (Univ. of Toronto). SR-A-GFP was in a pcDNA3.1(+)-C-eGFP backbone (Genescript). Inhibitor treatments are described in Table S1.

2.2.6. SR-BI gene expression assays

M1 and M2 RAW 264.7 macrophages were seeded in a 96 well plate. 70–90% confluence was targeted at the start of the experiment. The described NP or hHDL was added to the culture media for 2 h. NPs were added to a final concentration of 400 μg/ml and hHDL to 2.4 mg/ml. After incubation, cells were fixed by adding 1 volume of 10% buffered formalin (Fisher) to each well and incubated for 30 min at 37 ◦C. The cells were then washed 3× with PBS. Blocking and perforation was performed in one step with 10% Goat serum, 0.5%BSA, 0.1%Tween 20 PBS at 37 ◦C for 1 h. Cell were washed 3× in PBS. 0.5% BSA PBS with 0.5 μg/ml SR-BI antibody (Novus; #NB400–104) was added and the cells were incubated for 1 h at 37 ◦C. Cells were washed 3× with PBS before 0.5%BSA PBS containing 1 μg/ml Texas Red conjugated secondary antibody (Abcam; #ab6719) was added. Cells were incubated for 1 h at 37 ◦C. Cells were washed 3× with PBS and switched to PBS containing 100 nM DAPI to counter stain the nucleus for 5 minuets at 23 ◦C and washed 3× again with PBS. The plate was than analyzed with a VarioSkan LUX (ThermoFisher). Fluorescence was measured both for Texas Red and DAPI. Singly stained wells confirmed there was not significant crosstalk between the channels. The fluorescence of Texas Red was standardized for the number of cells in each well by dividing by the DAPI signal. A gene

expression score was assigned by normalizing to the standardized expression of the untreated cells.

2.2.7. Mouse experiments

All experiments were performed under the guidelines of the University of Tennessee's IACUC protocol #2231. BL6;129S-Scarb1tm1Kri/J mice were purchased from Jackson Laboratories and bred in house. Mice were genotyped with tail snip PCR analysis. Litter mates were used as experimental controls. Prior to injection, aggregates that did not form NPs were pelleted at 23 ◦C for 15 min at 15,000 x g in a Fisher Scientific AccuSpin Micro 17 centrifuge. The upper phase containing the dispersed NPs was reserved for injection although no pellet was visible because the NPs do not appear to form additional aggregates. The upper phase was imaged using SEM. NPs were loaded with 5 µl of a 2.5 mg/ml stock of NIR dye in ethanol for imaging (Life Technologies; #D-12731). The dye partitions into the hydrophobic interiors of the nanoparticles and does not leak in vivo [15]. 100 µl of 5 mg/ml NP solution in PBS was tail-vein injected into the mice. Mice were euthanized 3 h after injection by isoflurane and cervical dislocation. The HDL plasma concentration of C57BL/6 J mice is reported to be ~0.6 mg/ml [17], correlating to a blood HDL concentration of 0.35 mg/ml. The weight of the mouse was used to calculate the blood volume [18] and the resulting amount of hHDL co-injected with filomicelles. hHDL was injected to reach a level of at least 0.50 mg/ml HDL in the bloodstream to mimic the end point of the in vitro titration.

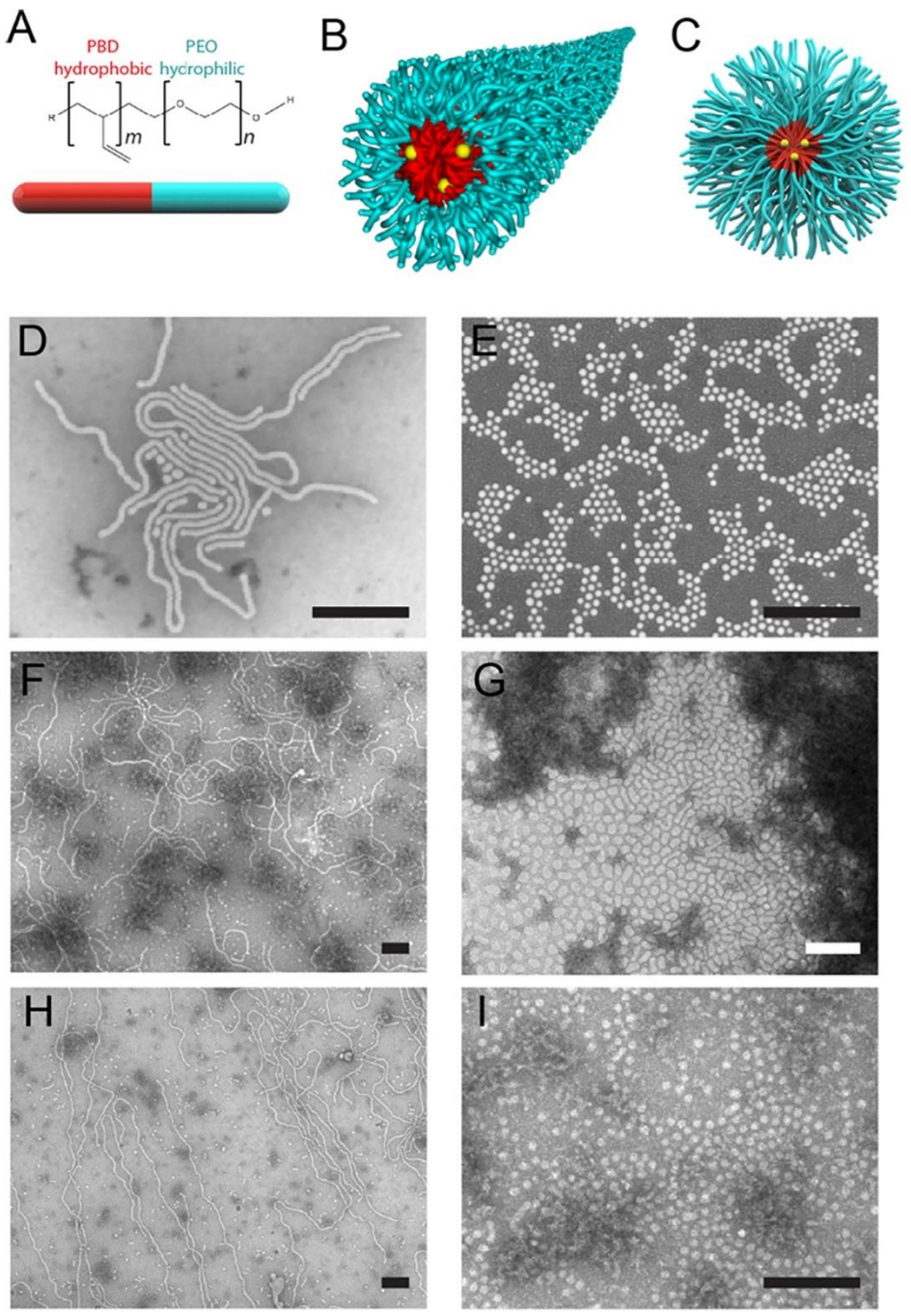

Figure 1. Properties of PEO-PBD filomicelles and PEO-PBD spheres used in this study. (A) Chemistries of the diblock copolymers. For the filomicelles: m = 46, n = 56. For the spheres: m = 69, n = 132. (B–C) Cartoons of a filomicelle (B) and a sphere (C). Yellow spheres represent dye molecules. (D–I) Electron micrographs of filomicelles in PBS (D), spheres in PBS (E), filomicelles in DMEM+FBS + P/S (macrophage media) (F), spheres in DMEM+FBS + P/S (macrophage media) (G), filomicelles in HANKS+FBS + P/S (CHO media) (H), sphere in HANKS+FBS + P/S (CHO media) (I). All incubation times were 2 h. Scale bars are 500 nm.

2.3 Results

We used two types of uncharged PEO-PBD nanoparticles (NPs) in this study: cylindrical/filomicelle and spherical. NP structural details are presented in Fig. 1A-C. Filomicelles and spheres have similar diameters: ~50 nm (Fig. 1D,E). The filomicelles have micron lengths (Fig. 1D) [13–15]. Both NPs are stable in the cell culture medias used in this study (Fig. 1F-I). We used spherical NPs as controls to determine the effects of NP geometry on NP – SR-BI interactions. Before determining possible interaction between NPs and SR-BI, we first wished to determine if human HDL (hHDL) bound filomicelles. This is a necessary control because HDL could bind a NP and guide it to SR-BI. If this is the case, HDL and not the NP would be responsible for binding SR-BI. We used 50 nm spherical carboxylated polystyrene (PS)-COOH NPs as a positive control because they have micro-molar affinities for hHDL [19]. We incubated PEO-PBD filomicelles and PS-COOH NPs separately with hHDL and determined the amount bound of Apo-AI - the main structural protein of HDL - using gel electrophoresis. Apo-AI bound PS-COOH NPs but did not bind PEO-PBD filomicelles at measurable levels (Fig. 2A). This shows that PEO-PBD filomicelles do not interact with HDL. Therefore, HDL should not be able to bind PEO-PBD filomicelles and guide them to SR-BI. Next, we wished to determine if PEO-PBD NPs interacted directly with SR-BI. We incubated PEO-PBD filomicelles and PEO-PBD spheres separately with recombinant SR-BI (rSR-BI). The amount of rSR-BI was increased for each experiment to determine how much rSR-BI is needed to saturate either PEO-PBD filomicelles or PEOPBD spheres. The mixture was allowed to come to equilibrium and the NPs were separated from rSR-BI by centrifugation of micron-size beads covered with an antibody to PEO. The amount of unbound rSR-BI in the supernatant was determined by spectroscopy and the amount of rSR-BI bound to the PEO-PBD NPs was determined by subtraction from the total

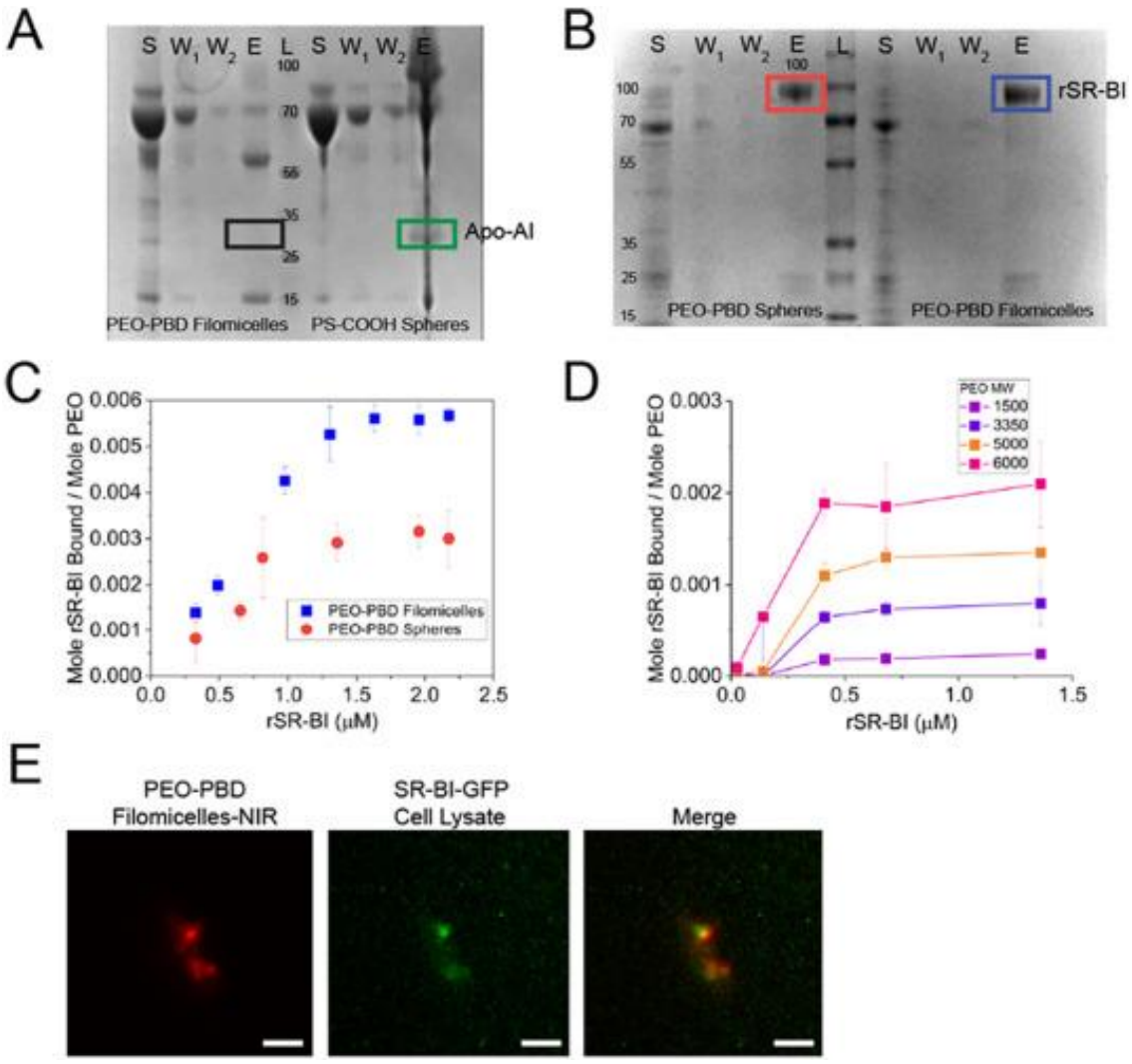

Figure 2. Binding of PEO-PBD NPs to hHDL and rSR-BI. (A) SDS-Page gel showing the results of a binding experiment where NPs were mixed with hHDL. The major structural protein of HDL, Apo-AI, does not bind PEO-PBD filomicelles (black rectangle). As a positive control we used 50 nm PS-COOH beads as a known binder of Apo-AI (green rectangle). S = supernatant, W = wash, E = elution, L = ladder. (B) SDS-Page gel showing the results of a binding experiment where PEO-PBD spheres (red rectangle) and PEO-PBD filomicelles (blue rectangle) were mixed with recombinant SR-BI (rSR-BI). (C) Plot of the binding of rSB-BI to PEO-PBD filomicelles and PEO-PBD spheres from the experiments described in (B). (D) Plot of the binding of free PEO molecules of varying MW with rSR-BI. (E) Fluorescence micrographs of PEO-PBD filomicelles-NIR that were incubated with lysed Idla7 cells expressing SR-BI-GFP. Scale bars are 5 μm.

amount of rSR-BI added to the incubation. PEO-PBD filomicelles pulled down a ~ 3-fold greater amount of rSR-BI than PEO-PBD spheres (Fig. 2B,C). The surface area of one 1μm × 50 nm cylinder/filomicelle is A = 2πrh + 2πr 2 ~ 300,000 nm^2. The surface area of one 50 nm sphere is A = 4πr 2 ~ 3000 nm^2. For 20 spheres that compare in length to a 1μm cylinder, the total surface area A = 600,000 nm^2, which is twice the exposed surface area of one cylinder. Thus, the difference in the amount of rSR-BI bound can be further increased 2-fold when the available surface areas of the spheres versus the cylinders are taken into account. The lengths of the PEO block of the copolymers are different for the filomicelles (n = 56; ~2500 Da) and the spheres (n = 132; ~5800 Da). To ensure that this PEO length difference was not the reason for different affinities of PEO-PBD filomicelles vs. PEO-PBD spheres for rSR-BI, we performed the above pull-down experiments but with single PEO molecules (not in a NP) of MW 1500, 3350, 5000, and 6000 Da. PEO affinity for rSR-BI increased as a function of PEO length (Fig. 2D). Since the PEO block of the PEO-PBD spheres is longer than the PEO block of the PEOPBD filomicelles, our NP-rSR-BI binding results are not an artifact of PEO length. Although it must be kept in mind that the conformation of free PEO (coiled) will be different from the conformation of PEO on a NP (brush-like). We wished to determine if PEO-PBD filomicelles localized with SR-BI using fluorescence microscopy. We transfected Chinese Hamster Ovary (CHO) cells that do not express SR-BI (Idla7 cells) with SR-BI-GFP [2]. We lysed the cells and added PEO-PBD filomicelles carrying near infrared dye (NIR) and added the mixture to a microscope slide. The PEO-PBD filomicelle-NIR and GFP signals overlapped (Fig. 2E). This shows that PEO-PBD filomicelles carrying NIR dye colocalize with SR-BI-GFP after CHO cell lysis. Note that the filomicelle has a short length in the micrograph most likely due to structural disruption caused by cellular factors such as lipids and fatty acids in the lysate.

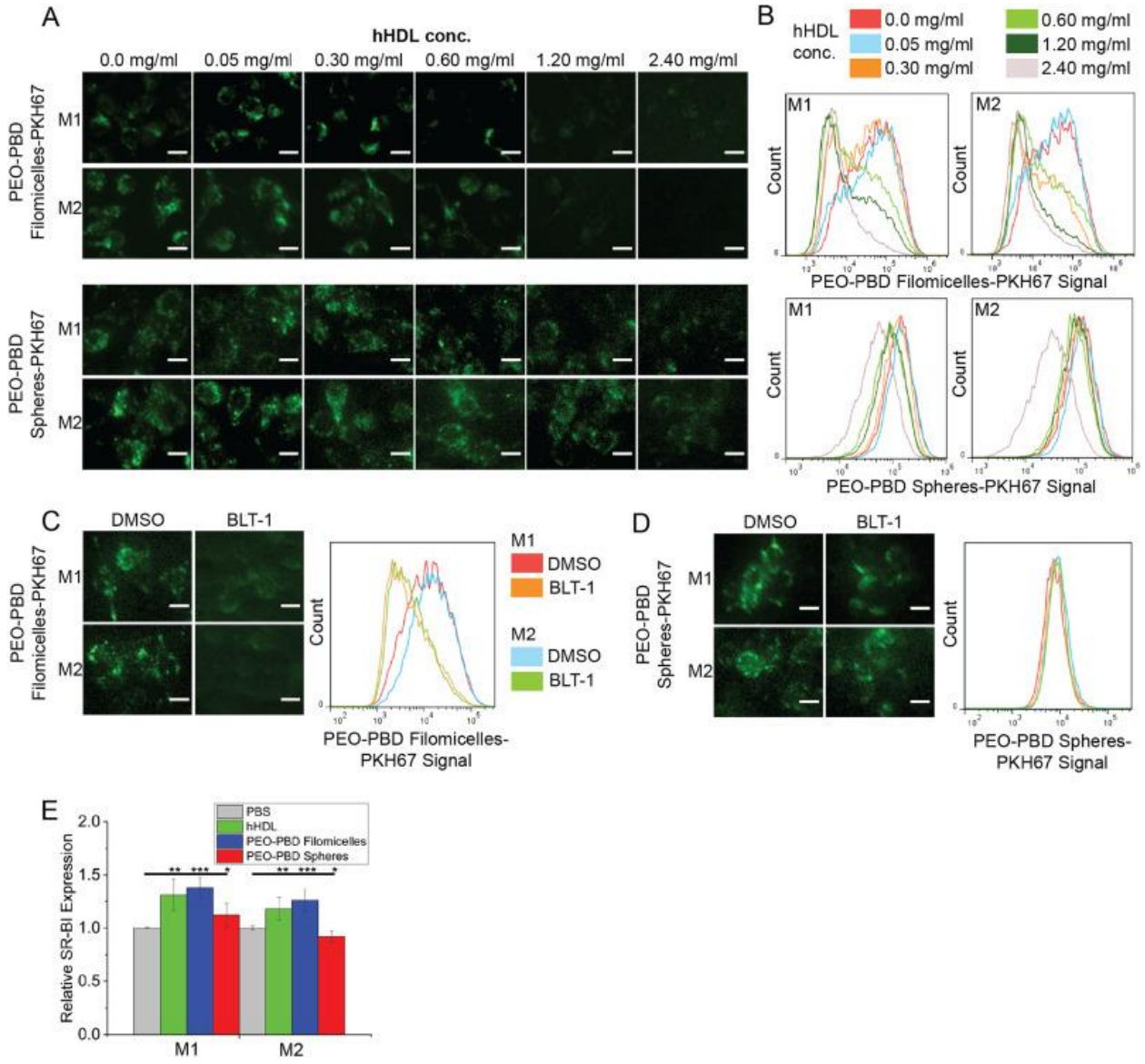

Figure 3. hHDL and BLT-1 block the uptake of PEO-PBD filomicelles by M1 and M2 murine macrophages. (A) Fluorescence micrographs of M1 and M2 murine macrophages that were incubated with either PEO-PBD filomicelles carrying PKH67 dye or PEO-PBD spheres carrying PKH67 dye and increasing amounts of unlabeled hHDL as indicated. (B) Plots of the fluorescence of the cells shown in (A) measured by flow cytometry. (C) Fluorescence micrographs of M1 and M2 murine macrophages incubated with PEO-PBD filomicelles carrying PKH67 dye in the absence and presence of BLT-1 and accompanying plot of the fluorescence of PEO-PBD filomicelles-PKH67 as measured by flow cytometry. Colour panel is for (C) and (D). (D) Fluorescence micrographs of M1 and M2 murine macrophages incubated with PEO-PBD spheres carrying PKH67 dye in the absence and presence of BLT-1 and accompanying plot of the fluorescence of PEO-PBD spheres-PKH67 as measured by flow cytometry. N = 10 k cells per curve for all plots. All scale bars are 10 μm. (E) Plot of the expression of SR-BI in M1 and M2 murine macrophages as measured by immunofluorescence against SR-BI. Experiments were performed in triplicate. * $P < 0.1$, ** $P < 0.05$, *** $P < 0.01$.

If PEO-PBD filomicelles bind SR-BI, then HDL could compete for the binding site on the cell surface of an SR-BI-expressing cell. To test this, we set up a series of titrations keeping the amount of filomicelles carrying PKH67 dye (green) at saturating concentrations and increased the amount of unlabeled hHDL in culture with RAW 264.7 M1 and M2 murine macrophages as a model in vitro system because they have high surface expression levels of SR-BI [20]. Also, macrophages are desirable targets in nanomedicine for a wide range of applications. The uptake of filomicelles carrying PKH67 (filomicelles-PKH67) decreased as the concentration of hHDL increased in fluorescence micrographs (Fig. 3A). Fluorescence quantification of the cells by flow cytometry showed a ~ 100-fold drop in signal as the hHDL concentration increased (Fig. 3B; Fig. S2–3). There was no difference in the uptake of spheres carrying PKH67 in the same experiments, except at the highest concentration of hHDL (Fig. 3A,B; Fig. S4–5). We wished to determine if the small molecule BLT-1, which blocks lipid transport at SR-BI [21], also decreased filomicelle uptake by macrophages. BLT-1 lowered the uptake of filomicelles carrying PKH67 in both M1 and M2 murine macrophages by ~10-fold but had no effect on the uptake of spheres carrying PKH67 (Fig. 3C,D; Fig. S6). We used immunofluorescence with SR-BI as the epitope tag to determine the expression levels of SR-BI in M1 and M2 murine macrophages that were incubated with either PBS, hHDL, filomicelles, or spheres for 2 h. SR-BI levels matched for hHDL and filomicelles and were slightly lower for spheres (Fig. 3E).

We wished to use a model mammalian cell system that had controllable expression of SR-BI to isolate SR-BI NP uptake from general macrophage NP uptake mechanisms, which are robust. To this end, we used CHO cells that constitutively express SR-BI (Idla7-SR-BI cells) versus CHO cells that do not express SR-BI (Idla7 cells) [22]. We performed similar hHDL titration experiments as the ones described above. As seen in the above experiments with

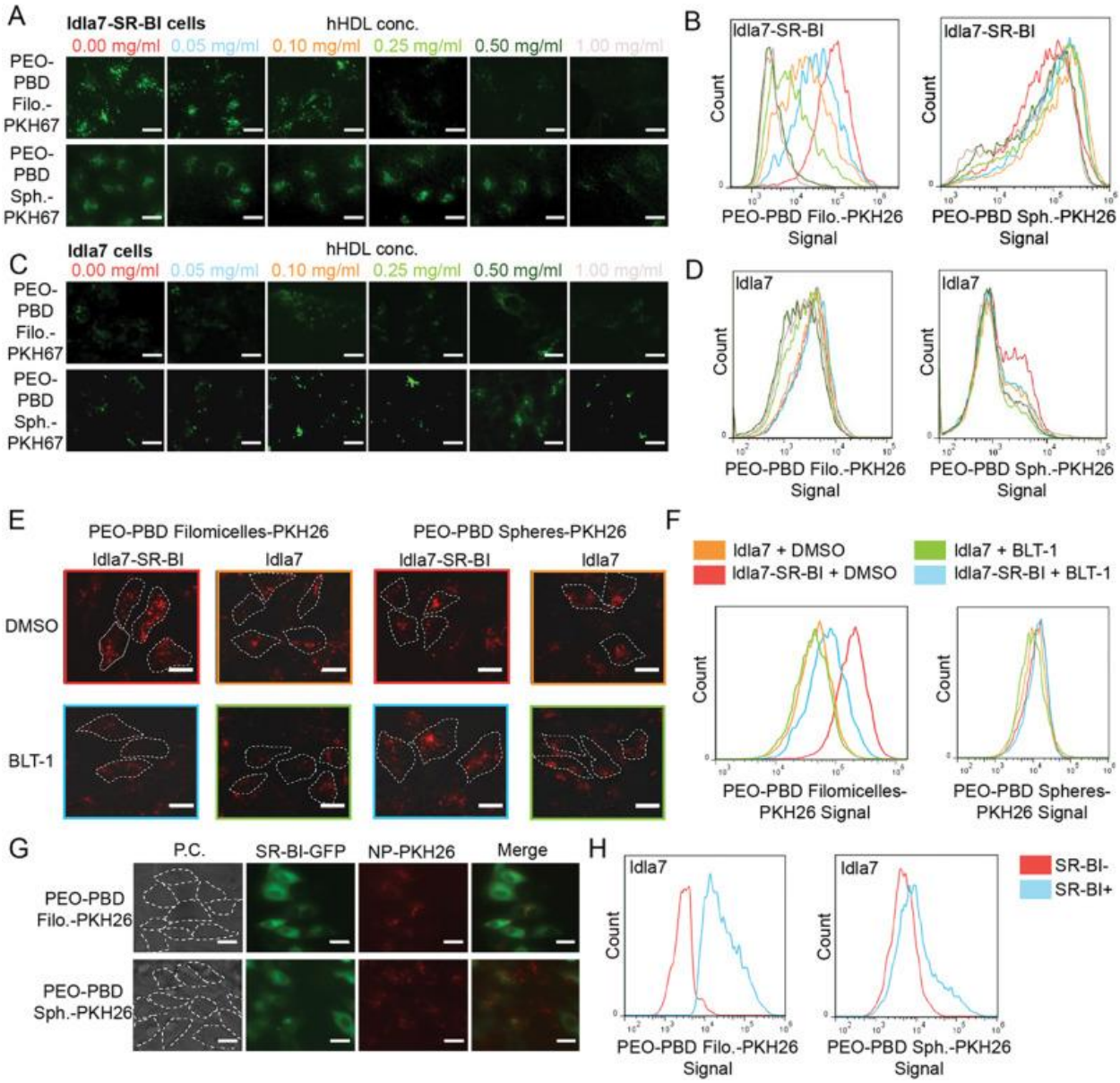

Figure 4. hHDL and BLT-1 block the uptake of PEO-PBD filomicelles by Idla7-SR-BI cells. (A) Fluorescence micrographs of Idla7-SR-BI cells incubated with PEO-PBD filomicelles carrying PKH67 or PEO-PBD spheres carrying PKH67 with increasing amounts of unlabeled hHDL as indicated. (B) Plots of the fluorescence of the cells shown in (A) measured by flow cytometry. (C) Fluorescence micrographs of Idla7 cells that were incubated with PEO-PBD filomicelles carrying PKH67 or PEO-PBD spheres carrying PKH67 with increasing amounts of unlabeled hHDL as indicated. (D) Plots of the fluorescence of the cells shown in (C) measured by flow cytometry. (E) Fluorescence micrographs of Idla7-SR-BI and Idla7 cells incubated with either PEO-PBD filomicelles carrying PKH26 or PEO-PBD spheres carrying PKH26 and DMSO (control) or BLT-1. (F) Plots of the fluorescence of the cells shown in (E) measured by flow cytometry. (G) Fluorescence micrographs of Idla7 cells that were transfected with SR-BI-GFP and incubated with either PEO-PBD filomicelles carrying PKH26 or PEO-PBD spheres carrying PKH26. (H) Plots of the fluorescence of the cells shown in (G) measured by flow cytometry. N = 10,000 cells per curve for all plots. All scale bars are 10 μm.

macrophages, hHDL titrations greatly reduced the uptake of PEO-PBD filomicelles carrying PKH67 by Idla7-SR-BI cells (Fig. 4A ,B; Fig. S7–8; Movie S1). There was little difference in the uptake of PEO-PBD spheres carrying PKH67 in the same experiments (Fig. 4A,B; Fig. S7–8). No significant uptake difference in either PEO-PBD filomicelles or PEO-PBD spheres carrying PKH67 was seen in hHDL titration experiments with Idla7 cells (Fig. 4C,D; Fig. S9–10). BLT-1 lowered the uptake of PEO-PBD filomicelles carrying PKH26 by Idla7-SR-BI cells versus DMSO controls, but had no difference on PEO-PBD filomicelle uptake by Idla7 cells (Fig. 4E,F; Fig. S11). BLT-1 had no effect on the uptake of PEO-PBD spheres carrying PKH26 by Idla7-SR-BI or Idla7 cells (Fig. 4E,F; Fig. S11). We added an additional conditional SR-BI expression system to our studies to confirm our findings in Idla7-SR-BI cells. We transiently expressed SR-BI-GFP in Idla7 cells and determined the uptake of PEO-PBD filomicelles and PEO-PBD spheres. Idla7 cells expressing SR-BI-GFP had a ~ 4–5-fold higher uptake of PEO-PBD filomicelles carrying PKH26 (red) than Idla7 cells that were not expressing SR-BI-GFP (Fig. 4G,H; Fig. S12). Again, no difference was seen in uptake of PEO-PBD spheres carrying PKH26 in these experiments (Fig. 4G,H; Fig. S12).

Since hHDL competes with PEO-PBD filomicelles for SR-BI binding in vitro, we wished to determine if hHDL could block or at least diminish PEO-PBD filomicelle uptake in vivo. We were particularly interested in any differences in PEO-PBD filomicelle and PEO-PBD sphere localization to the liver, which is the main organ that expresses SR-BI to which NPs have access. We co-injected (tail-vein) PEO-PBD filomicelles and PEOPBD spheres carrying near infrared (NIR) dye with unlabeled hHDL. We harvested the major organs and blood 3 h post-injection. We measured the NIR fluorescence of the major organs scaled by organ weight. We observed a ~ 2-fold drop in PEO-PBD filomicelle localization to the livers of wild-type C57BL/6 J mice and a ~ 2-fold increase in PEOPBD filomicelle presence in the plasma

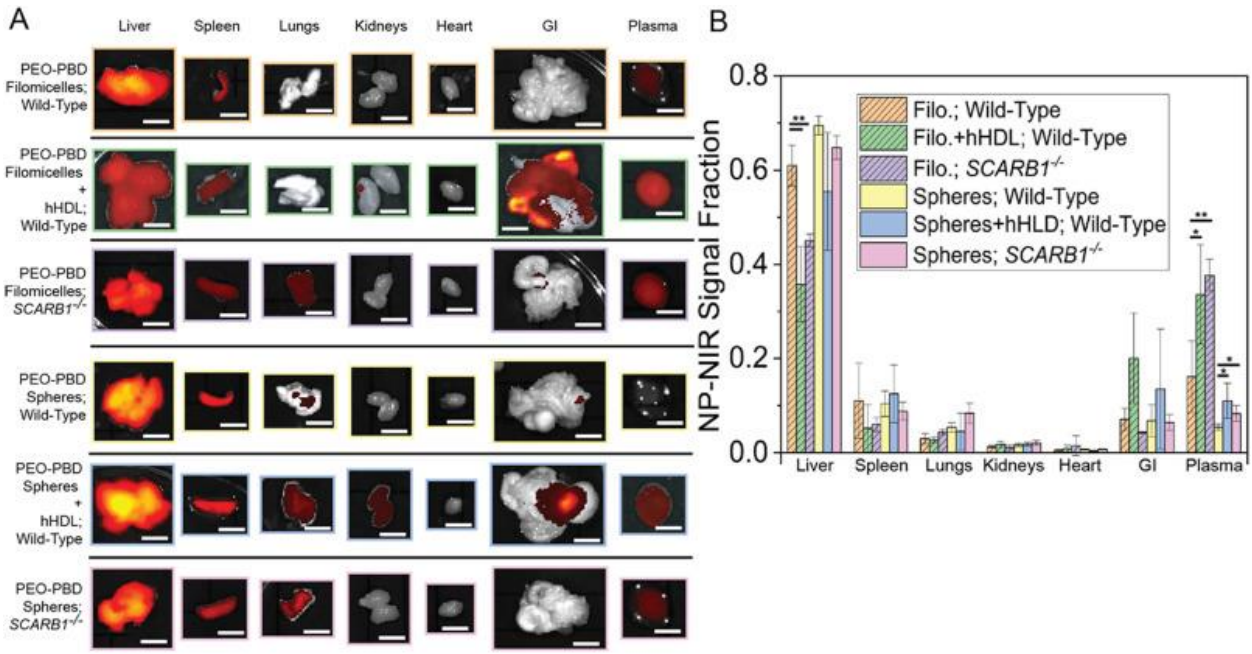

Figure 5. PEO-PBD filomicelle localization to the liver drops when co-injected with hHDL in wild-type mice and in SCARB1-deficient mice when injected solitarily. (A) Fluorescence micrographs of the major organs of wild-type mice that were harvested 3 h post tail-vein injection of either PEO-PBD filomicelles, PEO-PBD filomicelles + hHDL, PEO-PBD spheres, or PEO-PBD spheres + hHDL. The filomicelles and spheres were carrying NIR dye. PEO-PBD filomicelles and PEO-PBD spheres were also administered to SCARB1□ /□ mice as indicated. Scale bars are 10 mm. (B) Plot of the NIR signal fraction of the organs shown in (A). N = 5 mice per bar. * $P < 0.1$, ** $P < 0.05$.

and the gastrointestinal (GI) tract (Fig. 5A,B). Controls were solitary injections of PEO-PBD filomicelles into wild-type C57BL/6 J mice. With PEO-PBD spheres, we observed a slight drop in liver signal between the solitary and co-hHDL injections (Fig. 5A, B). We used SCARB1− /− mice as a model system for mice lacking SR-BI. We repeated the above experiments injecting either PEOPBD filomicelles or PEO-PBD spheres into the mice. The signal fraction of PEO-PBD filomicelles in the liver dropped ~2-fold from wild-type to SCARB1− /− mice (Fig. 5A, B). There was a corresponding ~2-fold increase in the signal fraction of PEO-PBD filomicelles in the plasma. The signal fraction of PEO-PBD spheres in the liver dropped slightly in SCARB1− /− mice versus wild-type and increased slightly in the plasma. Localization of PEO-PBD spheres was higher than that of PEO-PBD filomicelles in the lungs of wild-type and SCARB1− /− mice. The signal was statistically equivalent across the other major organs between wildtype and SCARB1− /− mice for the spheres (Fig. 5A, B). It is possible that lung macrophages take up PEO-PBD spheres more efficiently than PEO-PBD filomicelles; however, this has not been shown.

We wished to determine if filomicelles were entering macrophages and Idla7-SR-BI cells exclusively through SR-BI or if other factors were involved. We shut down a subset of typical NP entrance pathways using the following inhibitors: colchicine (pinocytosis) [23], cytochalasin B (phagocytosis) [24], rottlerin (macropinocytosis) [25], polyinosinic (PI) acid (lipoprotein endocytosis) [26], and monosdansyl cadaverine (clathrin-mediated endocytosis) [27]. PI acid had no effect on hHDL uptake by M1 and M2 macrophages (Fig. 6A,B; Fig. S13). Only rottlerin had a modest effect on hHDL uptake by M2 macrophages. However, PI acid blocked hHLD uptake by Idla7-SR-BI cells. Cytochalasin B decreased the uptake of filomicelles by M1 and M2 macrophages, whereas PI acid had the strongest effect on decreasing filomicelle uptake by Idla7-SR-BI cells (Fig. 6C,D; Fig. S14). Note the similarity

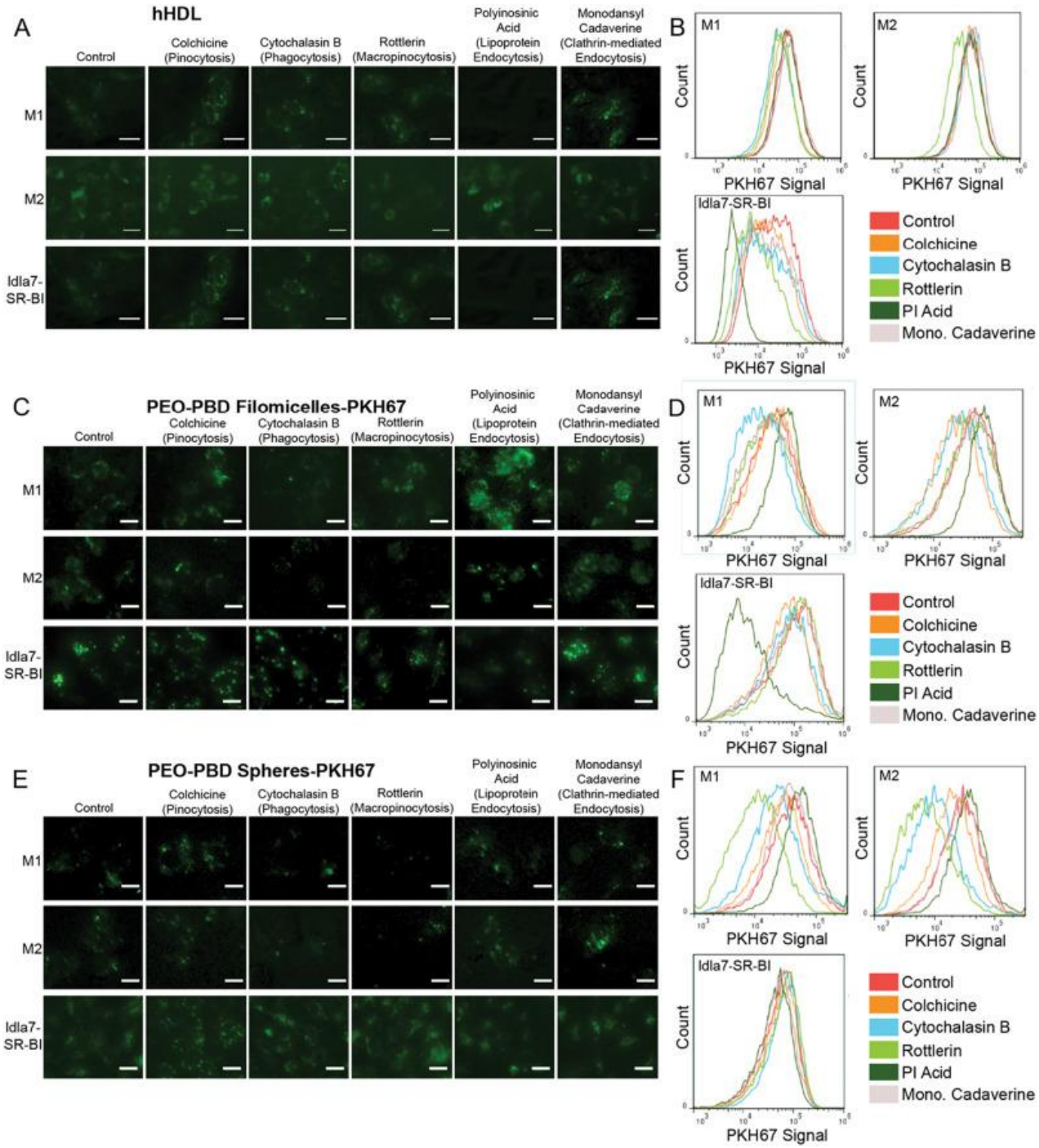

Figure 6. Entry of hHDL, filomicelles, and spheres into M1 and M2 murine macrophages and Idla7-SR-BI cells. (A) Fluorescence micrographs of M1 and M2 murine macrophages and Idla7-SR-BI cells incubated with hHDL carrying PKH67 and the indicated inhibitors. (B) Plots of the PKH67 fluorescence of the cells shown in (A) measured by flow cytometry. (C) Fluorescence micrographs of M1 and M2 murine macrophages and Idla7-SR-BI cells incubated with PEO-PBD filomicelles carrying PKH67 and the indicated inhibitors. (D) Plots of the PKH67 fluorescence of the cells shown in (C) measured by flow cytometry. (E) Fluorescence micrographs of M1 and M2 murine macrophages and Idla7-SR-BI cells incubated with PEO-PBD spheres carrying PKH67 and the indicated inhibitors. (F) Plots of the PKH67 fluorescence of the cells shown in (E) measured by flow cytometry. N = 10 k cells per curve. All scale bars are 10 μm.

in the uptake profiles of hHDL and filomicelles by M1 and M2 macrophages and Idla7-SR-BI cells when PI acid is used. Fluorescence uptake profiles of spheres by M1 and M2 macrophages showed macropinocytosis being the strongest factor followed by phagocytosis; none of the inhibitors had an effect on sphere uptake by Idla7-SR-BI cells (Fig. 6E,F; Fig. S15). This points to spherical uptake by Idla7-SR-BI cells being a passive event. PI acid mainly inhibits SR-A [26]. Macrophages express both SR-BI and SR-A [28]. Thus, PI acid is likely binding SR-A on macrophages and SR-BI is still available for binding hHDL, filomicelles, and spheres. Hence, the observed high uptake of hHDL and filomicelles by macrophages in the presence of PI acid (Fig. 6A,B). Therefore, we wished to determine if PI acid inhibits SR-BI in cells with controllable SR-A expression. We transiently transfected Idla7-SR-BI cells, which, unlike macrophages, do not express SR-A (Fig. S16), with mSR-A-GFP. GFP was used to monitor transfection efficiency, not to determine potential co-localization with filomicelles or spheres. Cells expressing mSR-A-GFP took up filomicelles in the presence of PI acid, which should now block mSR-A-GFP instead of SR-BI (Fig. 7A,B; Fig. S17). PI acid has no effect on sphere uptake in these cells (Fig. 7C,D; Fig. S16). This indicates that PI acid can inhibit SR-BI binding to PEO-filomicelles only in the absence of SR-A, its preferred binding partner. Thus, we postulate that filomicelles, like hHDL, bind SR-BI on the surfaces of M1 and M2 murine macrophages.

2.4 Discussion

PEG/PEO is used in nanomedical applications because it is biocompatible, and it has a low affinity for most proteins [29]. Thus, our discovery that PEO-PBD filomicelles have a strong affinity for SR-BI is surprising. However, there are several findings in the literature that foreshadowed our results. PEG-1500 in the crystallization buffer showed electron density in

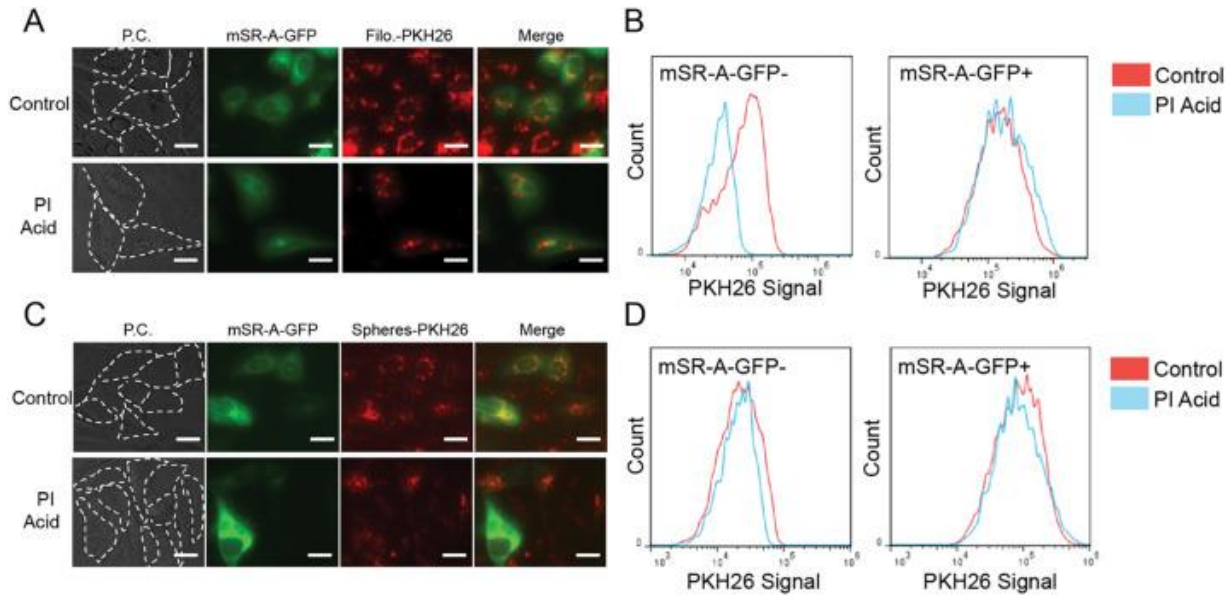

Figure 7. SR-A does not play a role in PEO-PBD filomicelles uptake by Idla7-SR-BI cells. (A) Fluorescence micrographs of Idla7-SR-BI cells that were transfected with mSR-A-GFP and incubated with PEO-PBD filomicelles-PKH26 with and without PI acid. (B) Plots of the PKH67 fluorescence of the cells shown in (A) measured by flow cytometry. (C) Fluorescence micrographs of Idla7-SR-BI cells that were transfected with mSR-A-GFP and incubated with PEO-PBD spheres-PKH26 with and without PI acid. (D) Plots of the PKH67 fluorescence of the cells shown in (C) measured by flow cytometry. N = 10 k cells per curve. All scale bars are 10 μm.

the crystal structure of LIMP-2, a member of the CD36 super family of scavenger receptor proteins, which also includes SR-BI [30]. The Pro270, Thr365, and Lys381 residues near PEG-1500 in the LIMP-2 structure were in the homologous SR-BI cavity/tunnel that is responsible for cholesterol transport [30]. This shows that single PEG/ PEO molecules can interact with proteins in the scavenger receptor superfamily. Recently, a crystallography study showed that PEG interacts with anti-PEG Fab at Trp96 of the heavy chain complementarity determining region 3 [31]. Trp53, Trp178, and Trp231 are in relatively close proximity to the PEG density in the LIMP-2 structure. They are conserved between LIMP-2 and SR-BI [30]. Given our findings that the affinity of PEG polymers - without PBD - for rSR-BI increases as a function of PEG length (Fig. 2D), we postulate that PEG may be interacting with these tryptophans in addition to its interaction with the Lys, Pro, and Thr residues listed above. Otherwise, the affinity of PEG for rSR-BI would not be a function of PEG length; each PEG molecule would bind two rSR-BI proteins. This is not what we observe. Additional structural biology and point mutation studies may shed light on the interactions between PEG and protein.

Although our spheres bound rSR-BI, they had weak affinity for cells expressing SR-BI. Spheres bind rSR-BI in pulldowns, but the binding assay showed that spheres have significantly less affinity for rSR-BI than filomicelles. This is further seen by the weak affinity spheres have for cells expressing SR-BI. Filomicelles had consistently stronger interactions with the same cells. We postulate that this is due to cooperativity among a filomicelle and a group of SR-BI receptors on the surface of a cell. HDL could also display cooperativity effects with SR-BI. Nascent HDL particles are disk-shaped molecular aggregates; only after they have taken up cholesterol esters do HDL particles mature into spheres [5]. Thus, HDL

have the potential to form elongated Rouleau structures [32]. It is possible that Rouleau HDL particles and filomicelles have binding synergies across multiple SR-BI molecules.

Our results suggest that SR-BI is directly involved in the binding of filomicelles to professional phagocytes and epithelial cells using macrophages and Idla7 as model systems. hHDL and filomicelle entry profiles match in M1, M2, and Idla7-SR-BI cells that are incubated with PI acid. PI acid had no effect on the uptake of hHDL and filomicelles by M1 and M2 macrophages. In contrast, PI acid blocked the uptake of both hHDL and filomicelles by Idla7-SR-BI cells. Macrophages express both SR-BI and SR-A, whereas the Idla7-SR-BI system is not expressing SR-A. PI acid mainly inhibits SR-A [26]. Thus, the addition of PI acid should inhibit SR-A instead of SR-BI in both M1 and M2 macrophages. Therefore, PI acid should have no effect on filomicelle binding and uptake by macrophages because SR-BI should be able to interact with filomicelles even in the presence of PI acid. This also holds for hHDL, as shown. By showing that PI acid does not reduce filomicelle uptake by Idla7 cells coexpressing SR-BI and SR-A-GFP, we confirmed that the SR-BI is still available for filomicelle binding when SR-A is inhibited.

It is not surprising that phagocytosis is the predominant filomicelle entry (but not binding) mechanism in macrophages. Indeed, particle uptake by professional phagocytes involves multiple membrane receptors, cytoskeleton action, bulk membrane flow and remodeling. We postulate SR-BI molecules expressed on macrophages bind filomicelles and bring them in proximity to other receptors that trigger phagocytosis, the main internalization pathway of foreign objects by macrophages. The identity of these receptors is currently unknown. They could include the Ig receptors FcR and CD14, and/or complement receptor CR3, which

binds C3, the only complement factor found on PEGylated liposomes after administration to mice [33].

In the context of NPs, SR-BI is responsible for the importation of HDLcoated silver NPs (AgNPs), and to a lesser extent uncoated AgNPs in RAW 264.7 mouse macrophages [34]. However, it is not clear if this is a direct interaction between AgNPs and SR-BI or if SR-BI controls AgNP uptake indirectly through macrophage activation. By using an epithelial cell line stably expressing SR-BI (Idal7-SR-BI), we were able to study an isolated PEG-SR-BI interaction and avoid effects of macrophage activity. Here we show that this is a direct interaction in the case of filomicelles. Our results point to a strategy to not only target cells expressing SR-BI, but to block the ability of SR-BI expressing phagocytes from clearing elongated PEGylated NPs by co-injection with HDL. Currently, one popular strategy to limit the clearing of NPs is to kill a large fraction of liver resident macrophages – Kupffer cells - using a pre-injection of clodronate liposomes [35]. Naturally, this will compromise the immunity of a potential patient. A strategy of using HDL in place of clodronate liposomes should not put the patient at potential risk because of a weakened immune system. This could be a new approach for extending the circulation and targeting of PEGylated NPs. Additional applications include using filomicelles to block the uptake of pathogens that use SRBI for cellular entry.

2.5 Conclusions

We show that by simply elongating a PEGylated NP in one dimension, it has a high affinity for SR-BI. SR-BI is a sought-after target in nanomedical applications from metabolism to

virology. Our strategy opens a plethora of options for delivering active agents to cells that express SR-BI. Supplementary data to this article can be found in the appendix.

Acknowledgements

The authors thank Dr. Eric Boder for the use of his flow cytometer, Dr. John R. Dunlap for electron microscopy, Deanna Riley for mouse genotyping, and the Center for Environmental Biotechnology for use of their IVIS imaging system. We also thank Dr. Monty Krieger of MIT for providing Idla7 and Idla7-SR-BI cell lines, Dr. Frank S. Bates of Univ. of Minnesota for diblock copolymers, and Dr. Sergio Grinstein of Univ. of Toronto for the SR-BI-eGFP plasmid. This work was supported in part by the National Institutes of Health R15GM116037.

References

1. C.M. Hales, M.D. Carroll, C.D. Fryer, C.L. Ogden, Prevalence of obesity and severe obesity among adults: United States, 2017–2018, NCHS Data Brief 360 (2020).
2. S. Acton, et al., Identification of scavenger receptor SR-BI as a high density lipoprotein receptor, Science 271 (1996) 518–520.
3. V.N. Sukhorukov, et al., Lipid metabolism: focus on atherosclerosis, Biomedicines 8 (2020) 262.
4. Y. Ji, et al., Scavenger receptor BI promotes high density lipoprotein-mediated cellular cholesterol efflux, J. Biol. Chem. 34 (1997) 20982–30985.
5. K. Frayn, R. Evans, Human Metabolism, 4th edition, Wiley Blackwell, 2019, pp. 304–312.
6. C. Rohrl, H. Stangl, HDL endocytosis and resecretion, Biochem. Biophys. Acta 1831 (2013) 1626–1633.
7. J. Canton, D. Neculai, S. Grinstein, Scavenger receptors in homeostasis and immunity, Nat. Rev. Immunol. 13 (2013) 621–623.
8. M.T. Catanese, et al., Role of scavenger receptor class B type I in hepatitis C virus entry: kinetics and molecular determinants, J. Virol. 84 (2010) 34–43.
9. C.C. Colpitts, P.L. Tsai, M.B. Zeisel, Hepatitis C virus entry: an intriguingly complex and highly regulated process, Int. J. Therm. Sci. 21 (2020) 2091.
10. C. Wei, et al., SARS-CoV-2 manipulates the SR-BI-mediated HDL uptake pathway for its entry, Nat. Metab. 2 (2020) 1391–1400.
11. P. Andre, G. Perlemuter, A. Budkowska, C. Brechot, V. Lotteau, Hepatitis C virus particles and lipoprotein metabolism, Semin. Liver Dis. 25 (2005) 93–104.

12. S. Busatto, et al., Lipoprotein-based drug delivery, Adv. Drug Deliv. Rev. 159 (2020) 377–390.

13. Y.-Y. Won, H.T. Davis, F.S. Bates, Giant wormlike rubber micelles, Science 283 (1999) 960–963.

14. P. Dalhaimer, F.S. Bates, D.E. Discher, Single molecule visualization of stiffnesstunable, flow-conforming worm micelles, Macromolecules 36 (2003), 68-73-6877. 15. Y. Geng, et al., Shape effects of filaments versus spherical particles in flow and drug delivery, Nat. Nanotechnol. 2 (2007) 249–255.

15. S. Zandi, et al., ROCK-isoform-specific polarization of macrophages associated with age-related macular degeneration, Cell Rep. 10 (2015) 1173–1186.

16. J.C. Link, et al., Increased high-density lipoprotein cholesterol levels in mice with XX versus XY sex chromosomes, Arterioscler. Thromb. Vasc. Biol. 35 (2015) 1778–1786.

17. A.C. Riches, et al., Blood volume determination in the mouse, J. Physiol. 228 (1973) 279–284.

18. U.C. Anozie, K.C. Quigley, A. Prescott, S.M. Abel, P. Dalhaimer, Equilibrium binding of isolated and in-plasma high-density lipoprotein (HDL) to polystyrene nanoparticles, J. Nanopart. Res. 22 (2020) 223.

19. A. Ji, et al., Scavenger receptor SR-BI in macrophage lipid metabolism, Atherosclerosis 217 (2011) 106–112.

20. T.J. Nieland, et al., Discovery of chemical inhibitors of the selective transfer of lipids mediated by the HDL receptor SR-BI, Proc. Natl. Acad. Sci. U. S. A. 99 (2002) 15422–15427.

21. K.F. Kozarsky, H.A. Brush, M. Krieger, Unusual forms of low density lipoprotein receptors in hamster cell mutants with defects in the receptor structural gene, J. Cell Biol. 102 (1986) 1567–1575.

22. C. Neubauer, A.M. Phelan, H. Kues, D.G. Lange, Microwave irradiation of rats at 2.35 GHZ activates pinocytotic-like uptake of tracer by capillary endothelial cells of cerebral cortex, Bioelectronics 11 (1990) 261–268.

23. A.T. Davis, R. Estensen, P.G. Quie, Cytochalasin-B.3. inhibition of human polymorphonuclear leukocyte phagocytosis, Proc. Soc. Exp. Biol. Med. 137 (1971) 161.

24. K. Sarkar, M.J. Kruhlak, S.L. Erlandsen, S. Shaw, Selective inhibition by rottlerin of macropinocytosis in monocyte-derived dendritic cells, Immunology 116 (2005) 513–524.

25. R. van Dijk, et al., Polyinosinic acid blocks adeno-associated virus macrophage endocytosis in vitro and enhances adeno-associated virus liver-directed gene therapy, Hum. Gene Ther. 24 (2013) 807–813.

26. P.K. Nandi, P.P. van Jaarsveld, R.E. Lippoldt, H. Edelhoch, Effect of basic compounds on the polymerization of clathrin, Biochemistry 20 (1981) 6706–6710.

27. V.N. Sukhorukov, et al., Lipid metabolism in macrophages: focus on atherosclerosis, Biomedicines 8 (2020) 262.

29. K. Kristenson, T.B. Engle, A. Stensballe, J.B. Simonsen, T.L. Andreson, The hard protein corona of stealth liposomes is sparse, J. Control. Release 307 (2019) 1–15.

30. D. Neculai, et al., Structure of LIMP-2 provides functional insights with implications for SR-BI and CD36, Nature 504 (2013) 172–176.

31. J.T. Huckaby, et al., Structure of an anti-PEG antibody reveals an open ring that captures highly flexible PEG polymers, Comm. Chem. 3 (2020) 124.

32. L. Zhang, et al., Morphology and structure of lipoproteins revealed by an optimized negative-staining protocol of electron microscopy, J. Lipid Res. 52 (2011) 175–194.
33. M. Hadjidemetriou, Z. Al-Ahmady, K. Kostarelos, Time-evolution of in vivo protein corona onto blood-circulating PEGylated liposomal doxorubicin (DOXIL) nanoparticles, Nanoscale 8 (2016) 6948–6957.
34. A.A. Aldossari, J.H. Shannahan, R. Podila, J.M. Brown, Scavenger receptor B1 facilitates macrophage uptake of silver nanoparticles and cellular activation, J. Nanopart. Res. 17 (2015) 313.
35. A.J. Tavares, et al., Effect of removing Kupffer cells on nanoparticle tumor delivery, Proc. Natl. Acad. Sci. U. S. A. 114 (2017) E10871–E10880.

Appendix

Table S1. List of Inhibitors Used

Inhibitor	Concentration	Duration	Source
BLT-1	50 µM	30 minutes	Sigma #373210
Colchicine	100 µg/ml	2 hours	Alfa Alesar #A1324003
Cytochalasin B	10 µg/ml	2 hours	Fisher #54-741-0
Rottlerin	2 µM	30 minutes	Acros #328490100
Polyinosinic Acid	10 µg/ml	30 minutes	Sigma #P4154
Monodansyl Cadaverine	200 µM	10 minutes	Sigma #30432

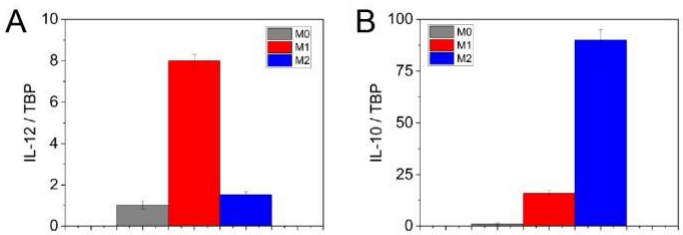

Figure S 1. Confirmation of macrophage polarization by RT-PCR. (A-B) Plots of the relative expression of IL-12 (M1 phenotype) (A) and IL-10 (M2 phenotype) (B) for the polarized macrophages used in the experiments.

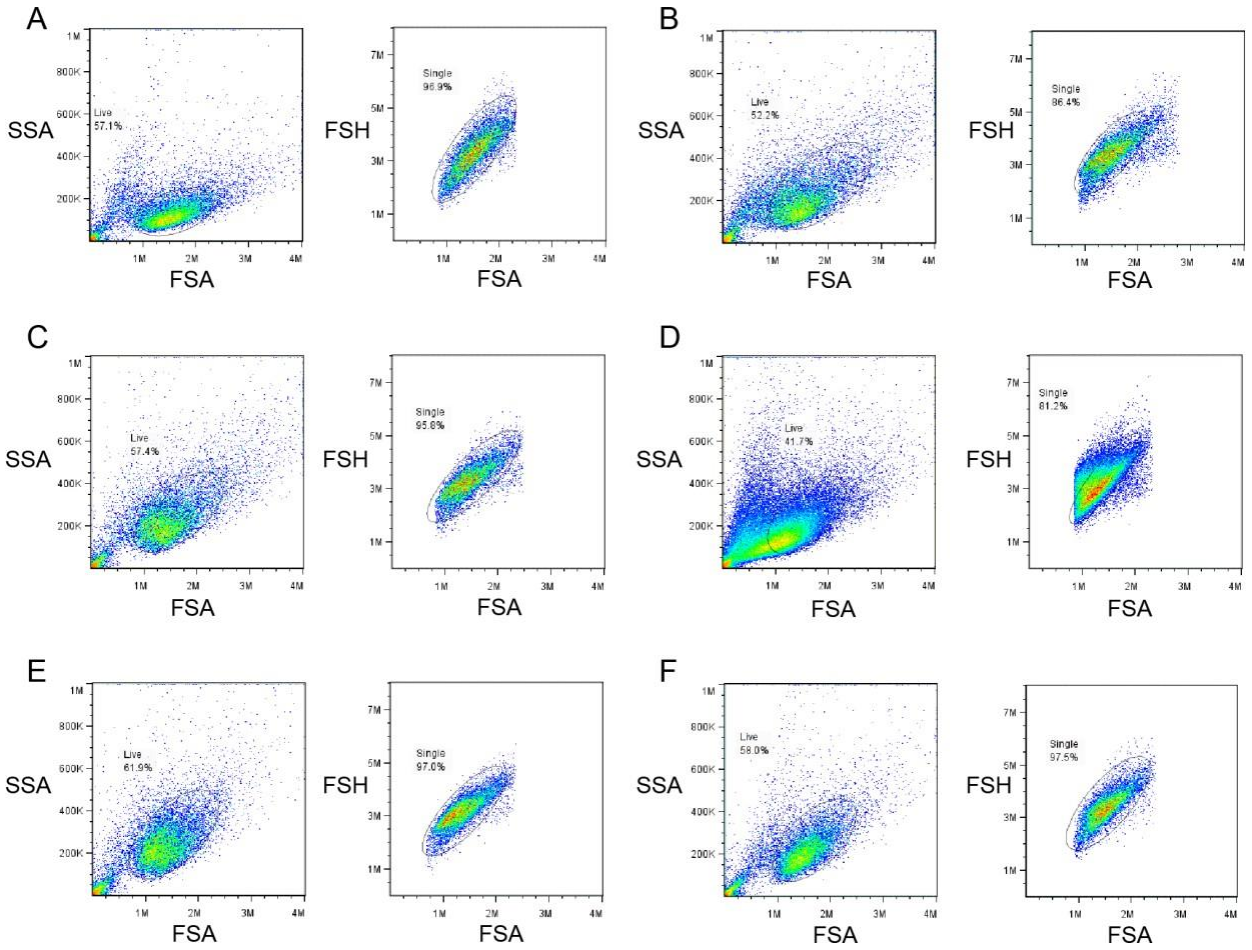

Figure S 2. Scatter plots for the PEO-PBD filomicelles-PKH67 histograms shown in Figure 3B for M1 murine macrophages. (A) 0.0 mg/ml hHDL. **(B)** 0.05 mg/ml hHDL. **(C)**0.30 mg/ml hHDL. **(D)** 0.60 mg/ml hHDL. **(E)** 1.20 mg/ml hHDL. **(F)** 2.40 mg/ml hHDL. SSA= side scatter area. FSA = forward scatter area. FSH = forward scatter height.

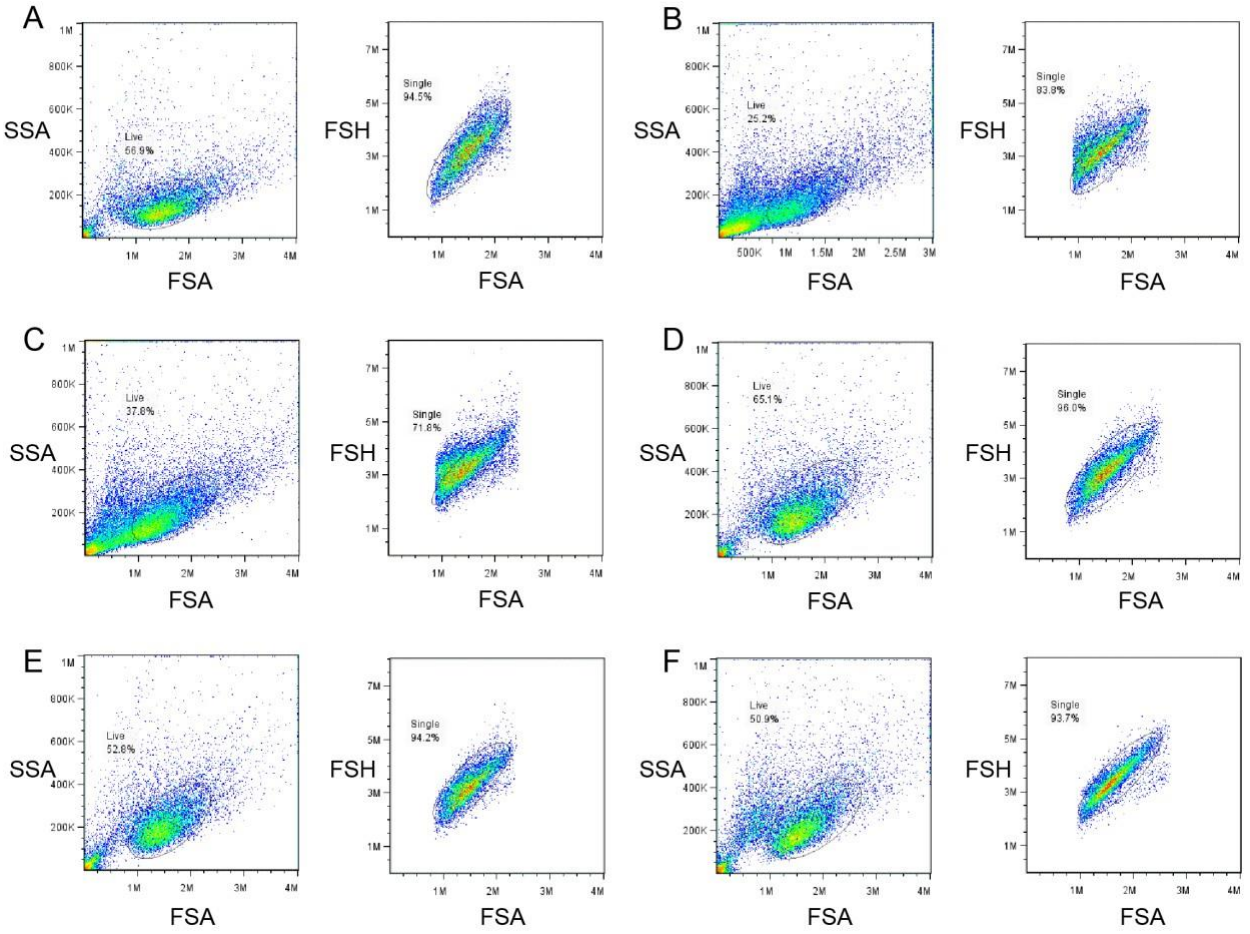

Figure S 3. Scatter plots for the PEO-PBD filomicelles-PKH67 histograms shown in Figure 3B for M2 murine macrophages. (A) 0.0 mg/ml hHDL. **(B)** 0.05 mg/ml hHDL. **(C)**0.30 mg/ml hHDL. **(D)** 0.60 mg/ml hHDL. **(E)** 1.20 mg/ml hHDL. **(F)** 2.40 mg/ml hHDL. SSA= side scatter area. FSA = forward scatter area. FSH = forward scatter height.

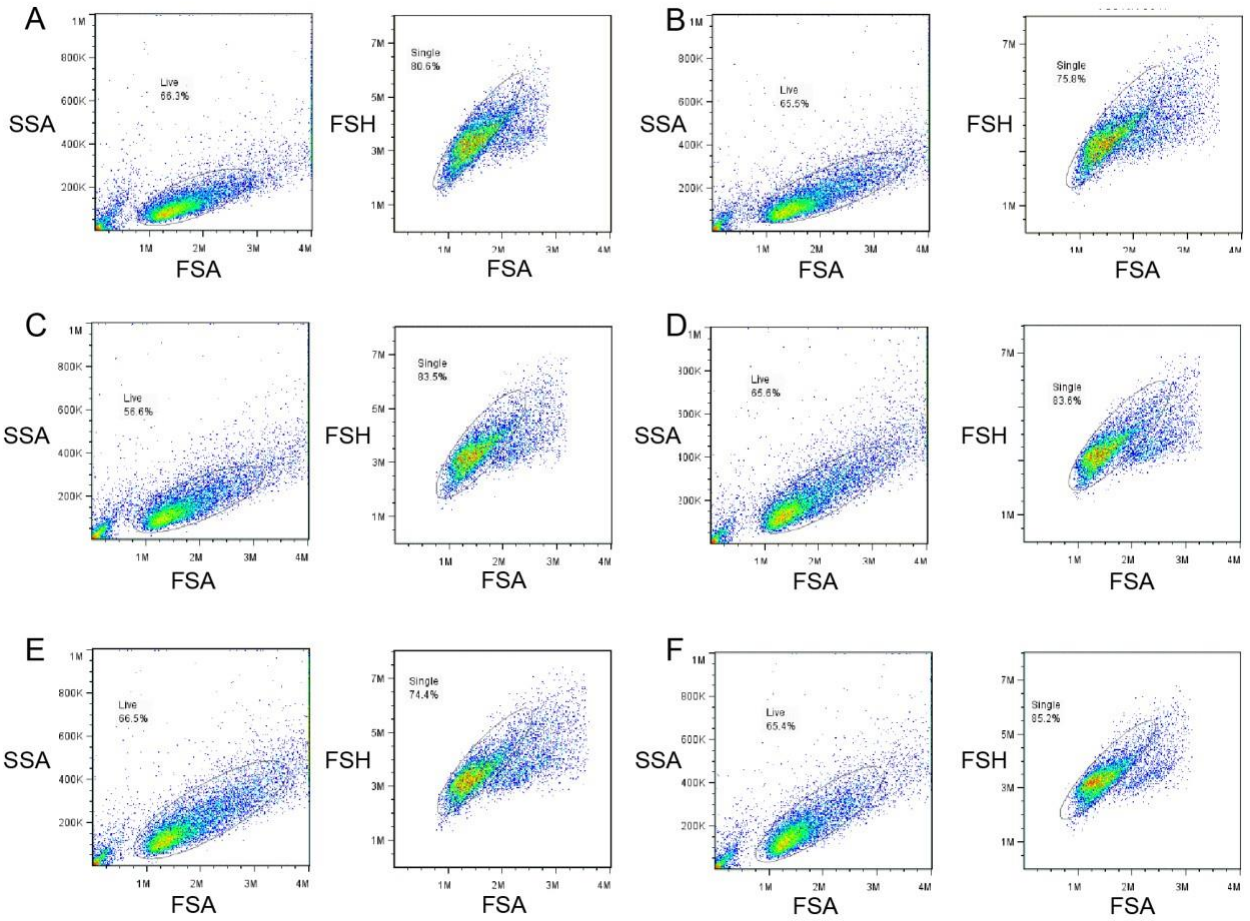

Figure S 4. **Scatter plots for the PEO-PBD spheres-PKH67 histograms shown in Figure 3B for M1 murine macrophages. (A)** 0.0 mg/ml hHDL. **(B)** 0.05 mg/ml hHDL. **(C)** 0.30 mg/ml hHDL. **(D)** 0.60 mg/ml hHDL. **(E)** 1.20 mg/ml hHDL. **(F)** 2.40 mg/ml hHDL. SSA = side scatter area. FSA = forward scatter area. FSH = forward scatter height.

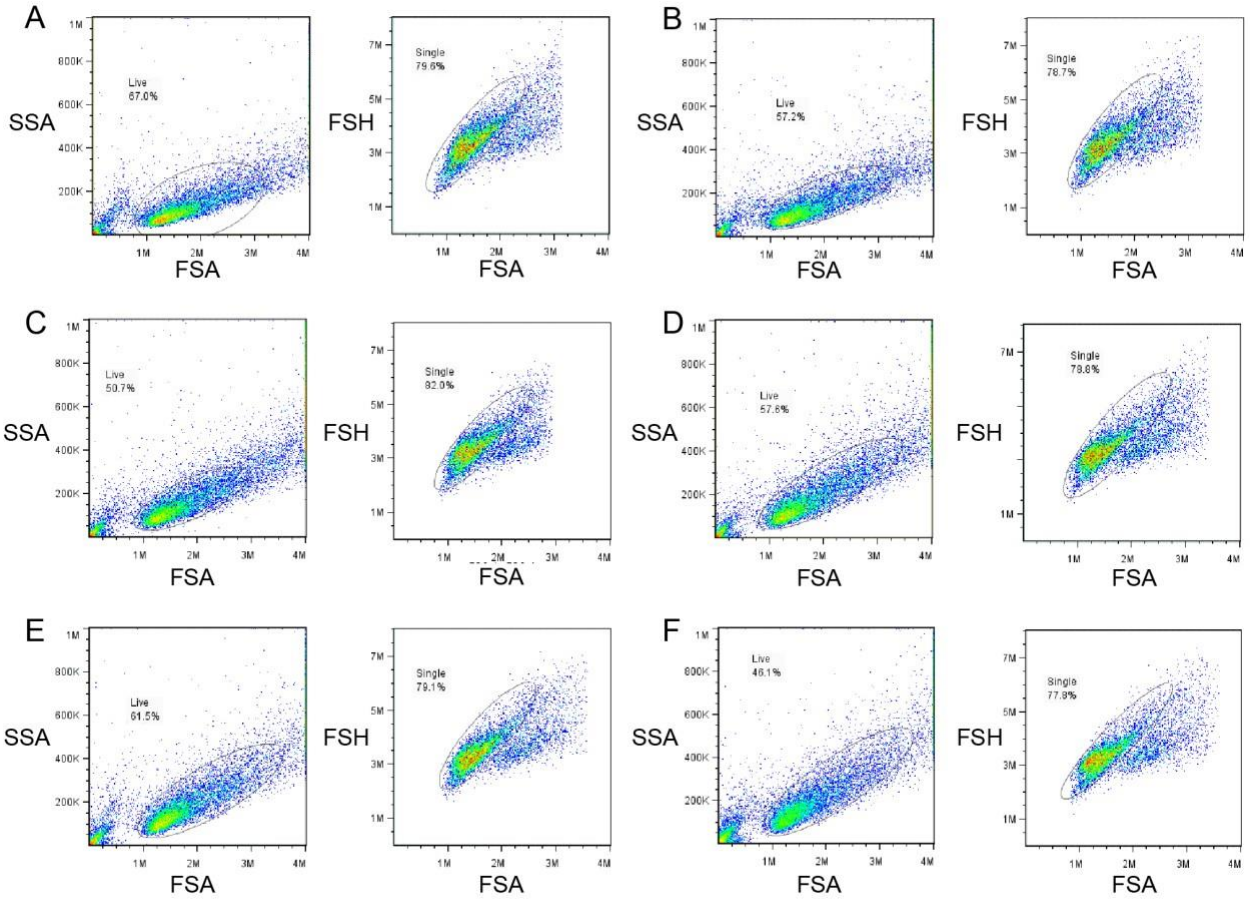

Figure S 5. **Scatter plots for the PEO-PBD spheres-PKH67 histograms shown in Figure 3B for M2 murine macrophages. (A)** 0.0 mg/ml hHDL. **(B)** 0.05 mg/ml hHDL. **(C)** 0.30 mg/ml hHDL. **(D)** 0.60 mg/ml hHDL. **(E)** 1.20 mg/ml hHDL. **(F)** 2.40 mg/ml hHDL. SSA = side scatter area. FSA = forward scatter area. FSH = forward scatter height

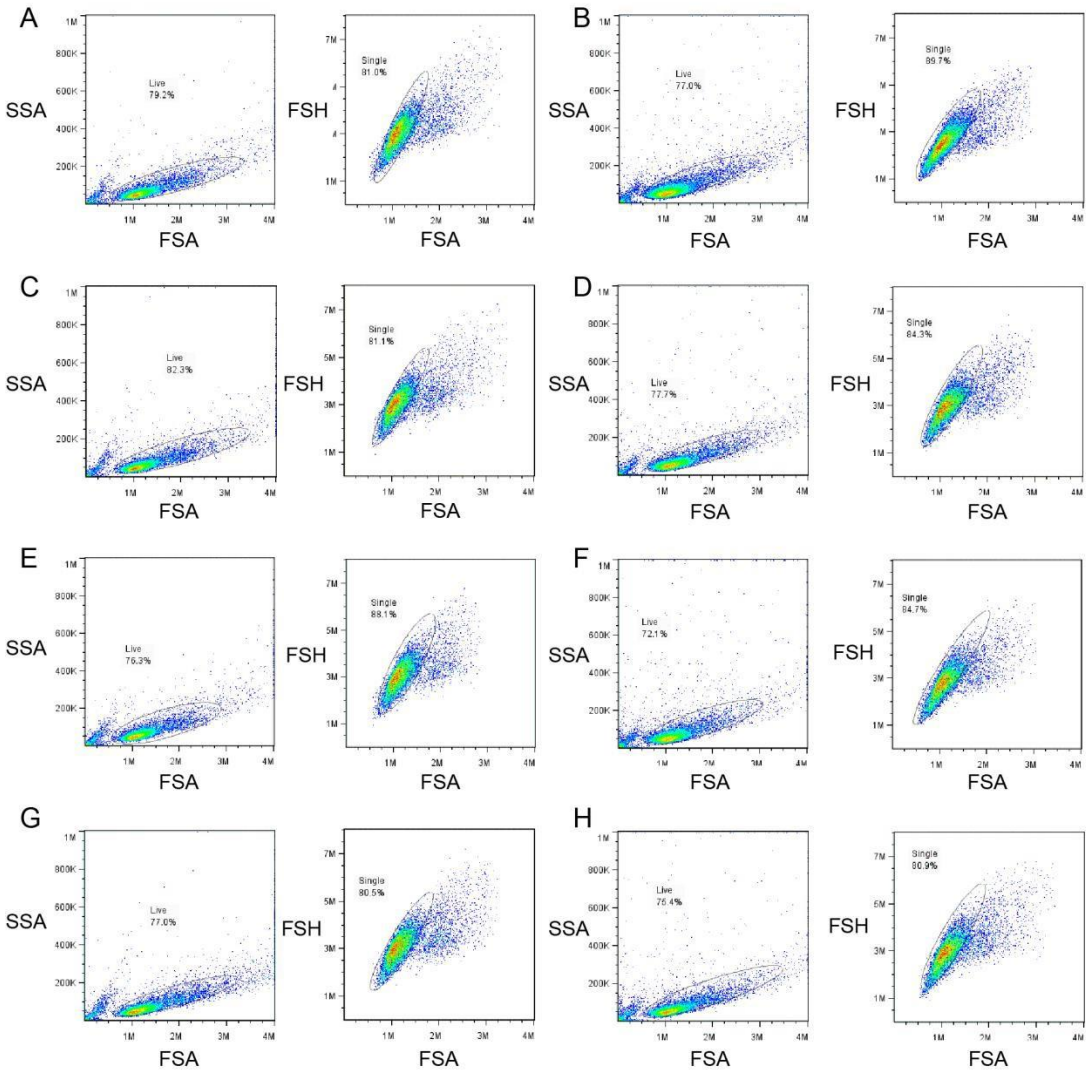

Figure S 6. Scatter plots for the PEO-PBD filomicelles-PKH67 and PEO-PBD spheres-PKH67 histograms shown in Figure 3C,D for M1 and M2 murine macrophages. (A-B) M1 macrophages incubated with PEO-PBD filomicelles-PKH67 with DMSO (A) or BLT-1 (B). **(C-D)** M2 macrophages incubated with PEO-PBD filomicelles-PKH67 with DMSO (C) or BLT-1 (D). **(E-F)** M1 macrophages incubated with PEO-PBD spheres-PKH67 with DMSO (E) or BLT-1 (F). **(G-H)** M2 macrophages incubated with PEO-PBD spheres-PKH67 with DMSO (G) or BLT-1 (H). SSA = side scatter area. FSA = forward scatter area. FSH = forward scatter height.

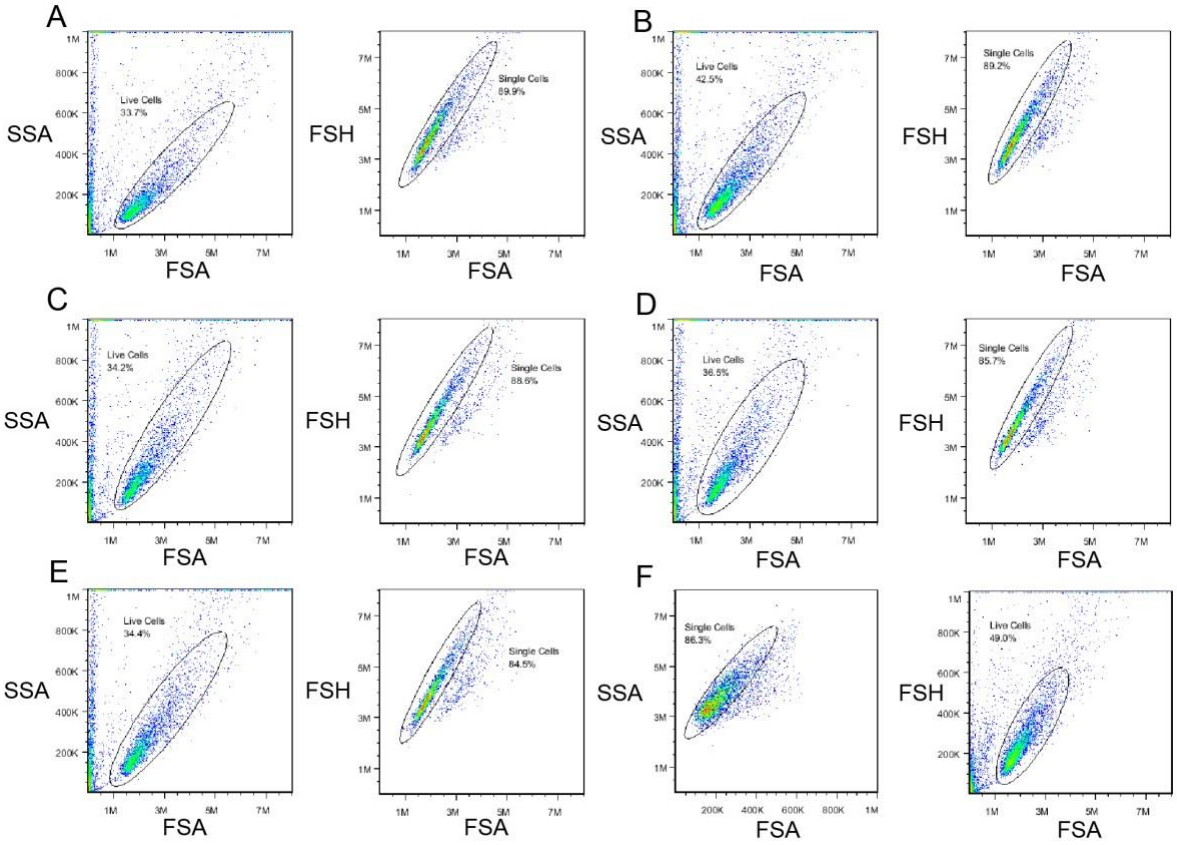

Figure S 7. Scatter plots for PEO-PBD filomicelles-PKH67 histograms shown in Figure 4B for Idla7-SR-BI cells. (A) 0.0 mg/ml hHDL. **(B)** 0.05 mg/ml hHDL. **(C)** 0.10 mg/ml hHDL. **(D)** 0.25 mg/ml hHDL. **(E)** 0.50 mg/ml hHDL. **(F)** 1.00 mg/ml hHDL. SSA = side scatter area. FSA = forward scatter area. FSH = forward scatter height.

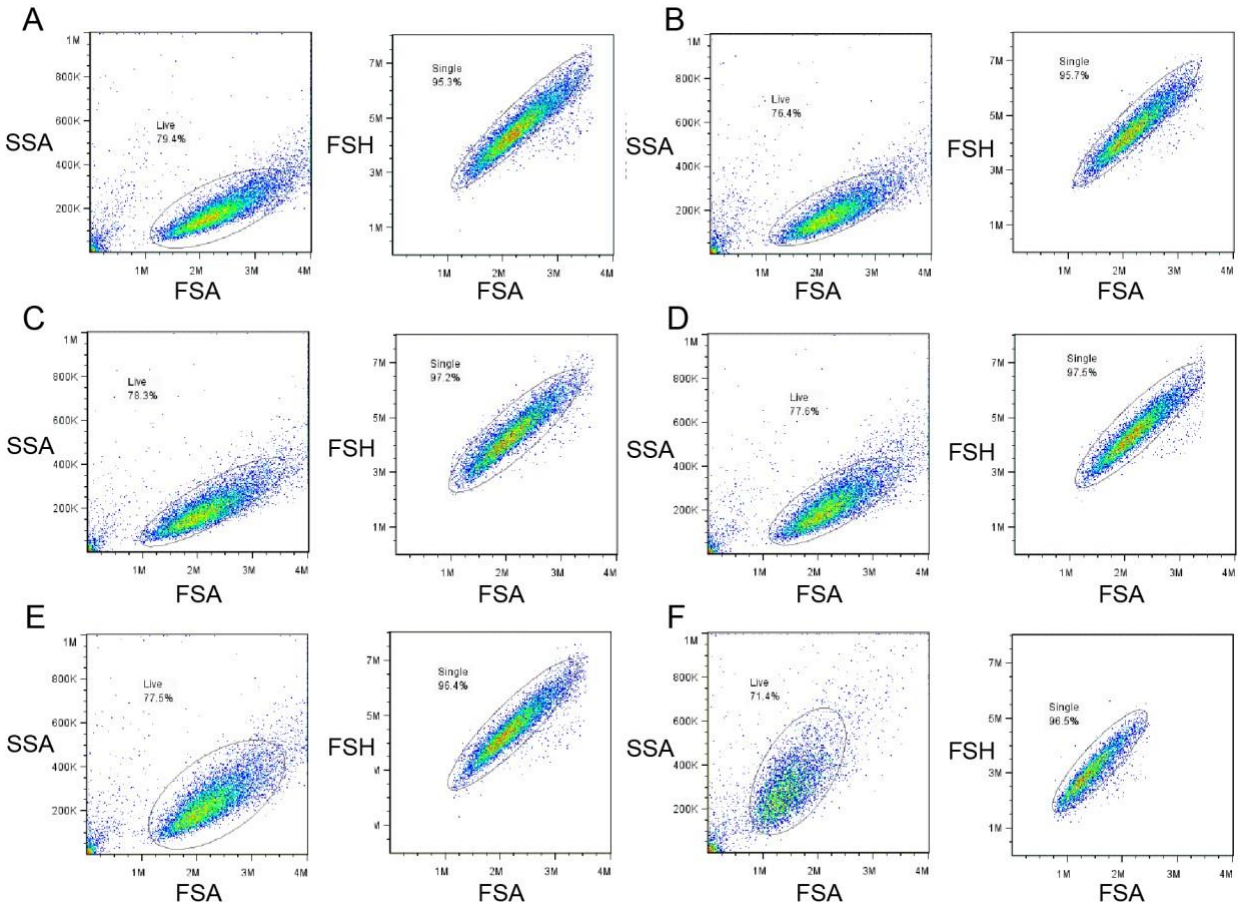

Figure S 8. Scatter plots for PEO-PBD spheres-PKH67 histograms shown in Figure 4B for Idla7-SR-BI cells. (A) 0.0 mg/ml hHDL. **(B)** 0.05 mg/ml hHDL. **(C)** 0.10 mg/ml hHDL. **(D)** 0.25 mg/ml hHDL. **(E)** 0.50 mg/ml hHDL. **(F)** 1.00 mg/ml hHDL. SSA = side scatter area. FSA = forward scatter area. FSH = forward scatter height.

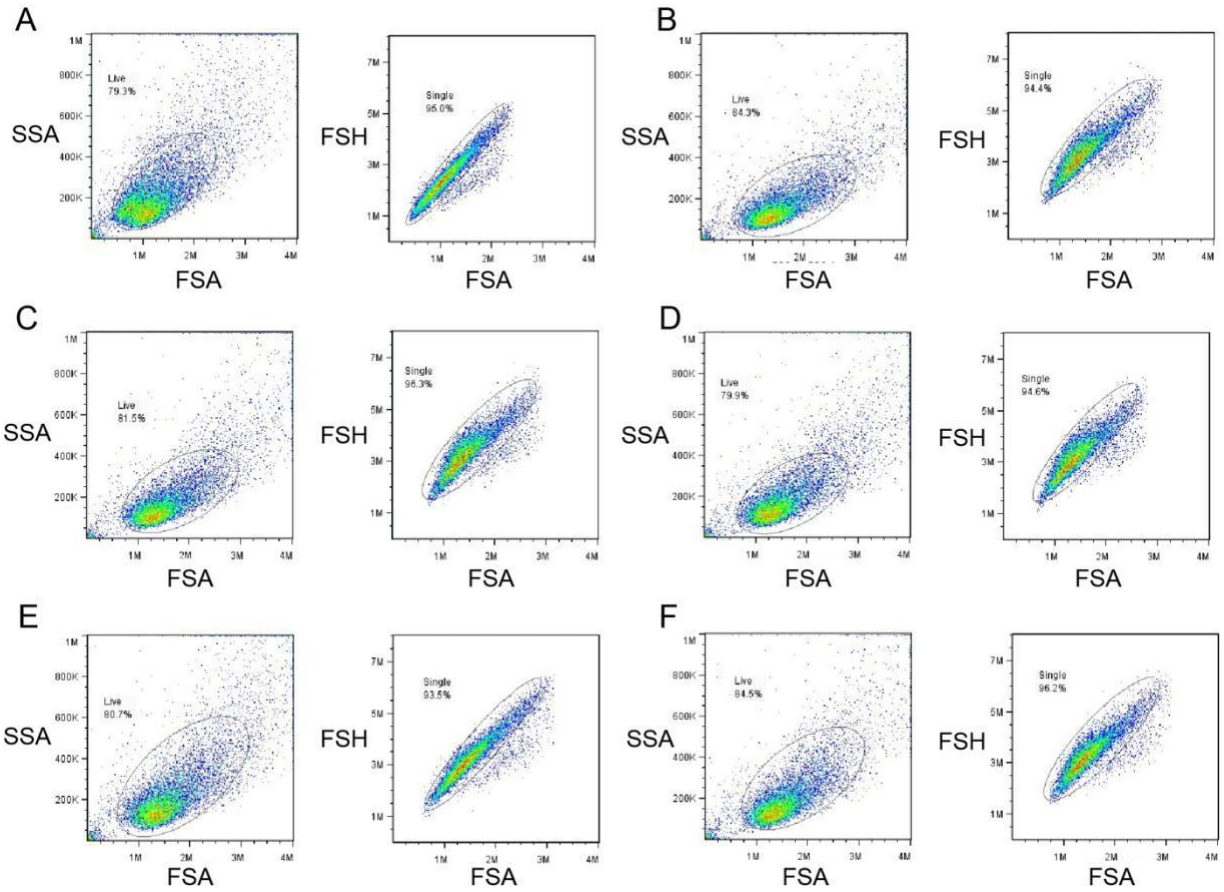

Figure S 9. Scatter plots for PEO-PBD filomicelles-PKH67 histograms shown in Figure4D for Idla7 cells. (A) 0.0 mg/ml hHDL. **(B)** 0.05 mg/ml hHDL. **(C)** 0.10 mg/ml hHDL. **(D)**0.25 mg/ml hHDL. **(E)** 0.50 mg/ml hHDL. **(F)** 1.00 mg/ml hHDL. SSA = side scatter area. FSA = forward scatter area. FSH = forward scatter height.

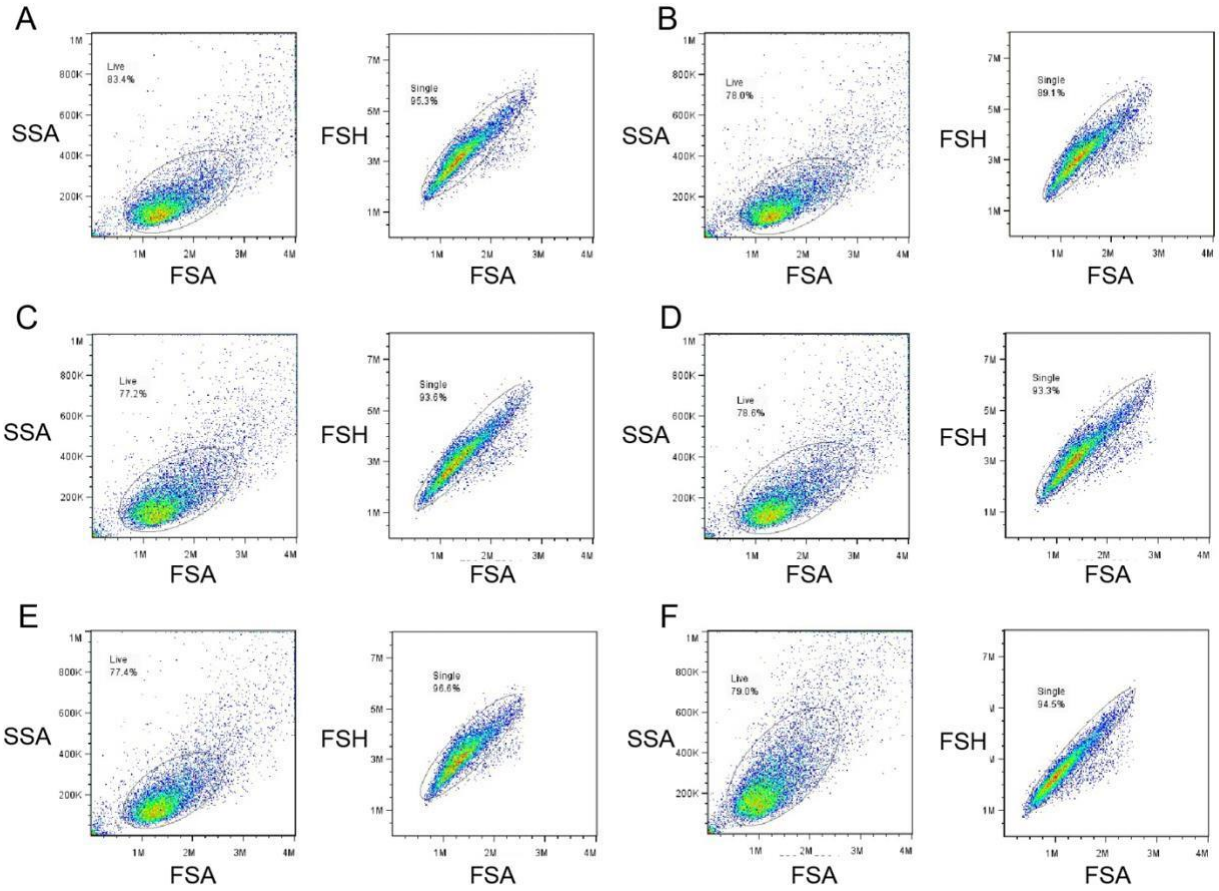

Figure S 10. Scatter plots for PEO-PBD spheres-PKH67 histograms shown in Figure 4D for Idla7 cells. (A) 0.0 mg/ml hHDL. **(B)** 0.05 mg/ml hHDL. **(C)** 0.10 mg/ml hHDL. **(D)** 0.25 mg/ml hHDL. **(E)** 0.50 mg/ml hHDL. **(F)** 1.00 mg/ml hHDL. SSA = side scatter area. FSA = forward scatter area. FSH = forward scatter height.

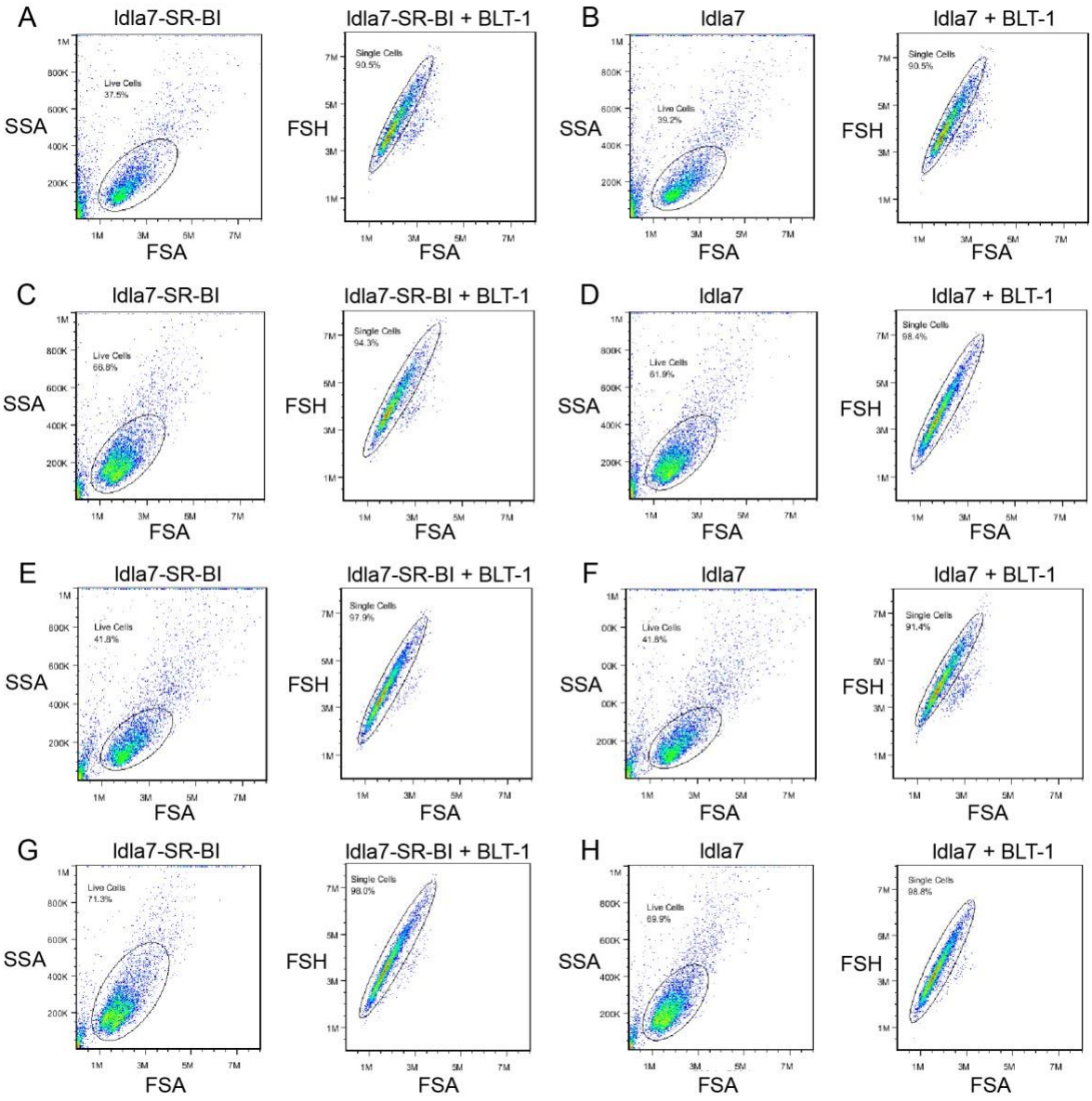

Figure S 11. Scatter plots for PEO-PBD filomicelles-PKH26 and PEO-PBD spheres- PKH26 histograms shown in Figure 4F for Idla7 and Idla7-SR-BI cells. (A-D) Plots for PEO-PBD filomicelles-PKH26. **(E-H)** Plots for PEO-PBD spheres-PKH26. SSA = side scatter area. FSA = forward scatter area. FSH = forward scatter height.

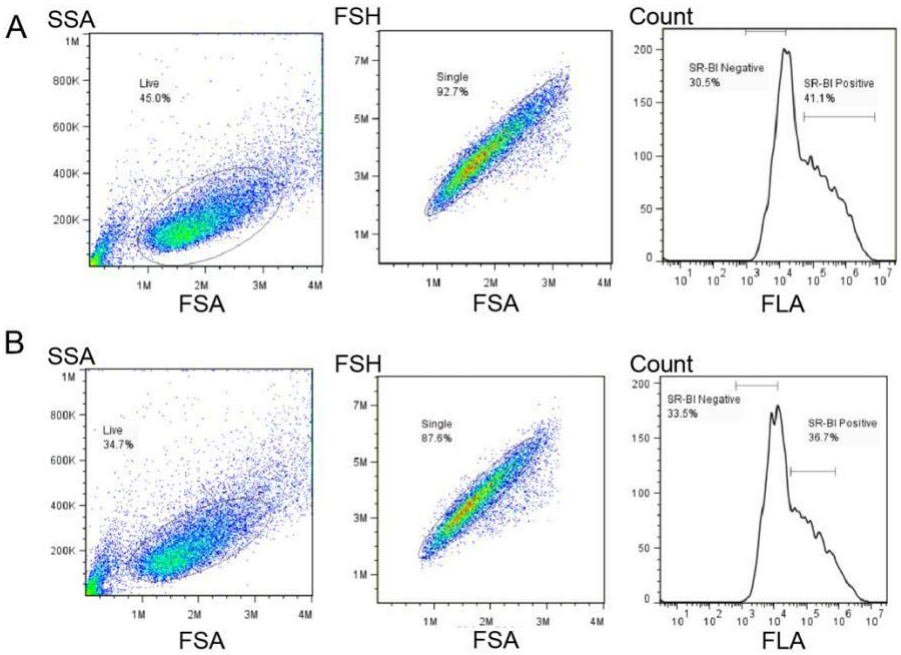

Figure S 12. Scatter plots for PEO-PBD filomicelles-PKH26 and PEO-PBD spheres- PKH26 histograms shown in Figure 4H. (A) Plots for PEO-PBD filomicelles-PKH26. **(B)** Plots for PEO-PBD spheres-PKH26. SSC-A = side scatter area. FSC-A = forward scatter area. FSC-H = forward scatter height. FLA-1 = PKH26 fluorescence.

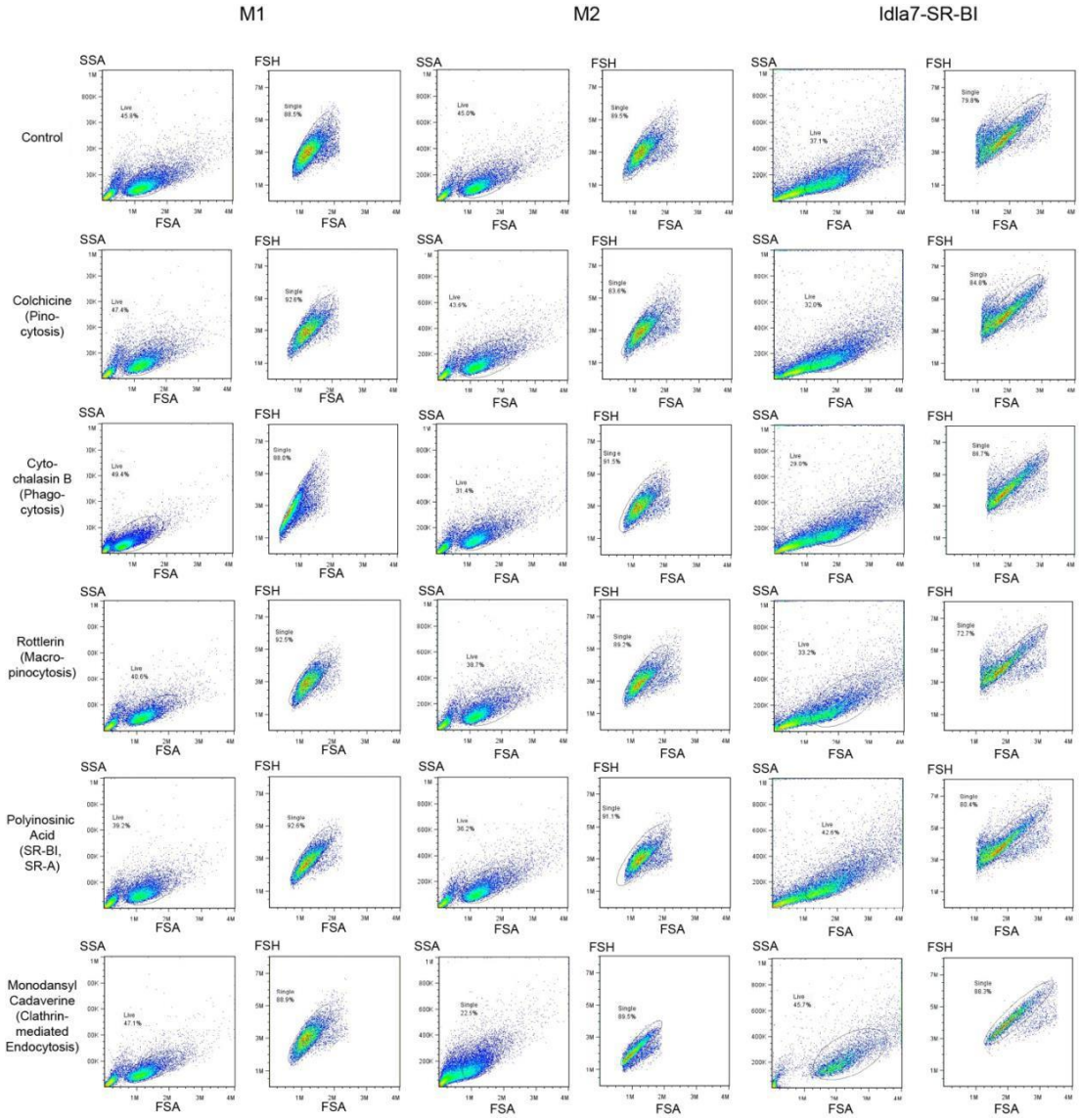

Figure S 13. Scatter plots for hHDL shown in Figure 6D. SSA = side scatter area. FSA = forward scatter area. FSH = forward scatter height.

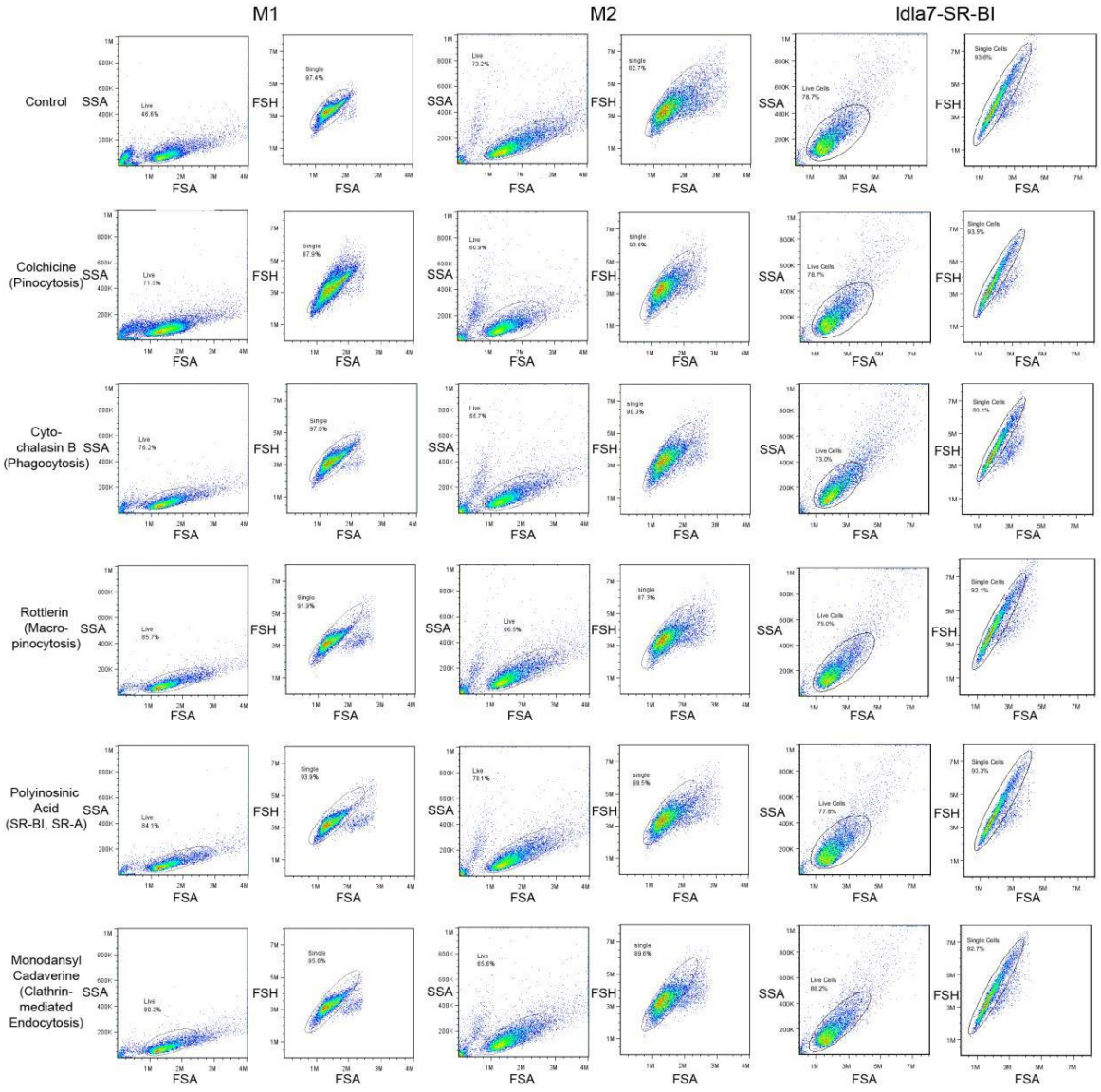

Figure S 14. **Scatter plots for PEO-PBD filomicelles-PKH67 shown in Figure 6D.** SSA =side scatter area. FSA = forward scatter area. FSH = forward scatter height.

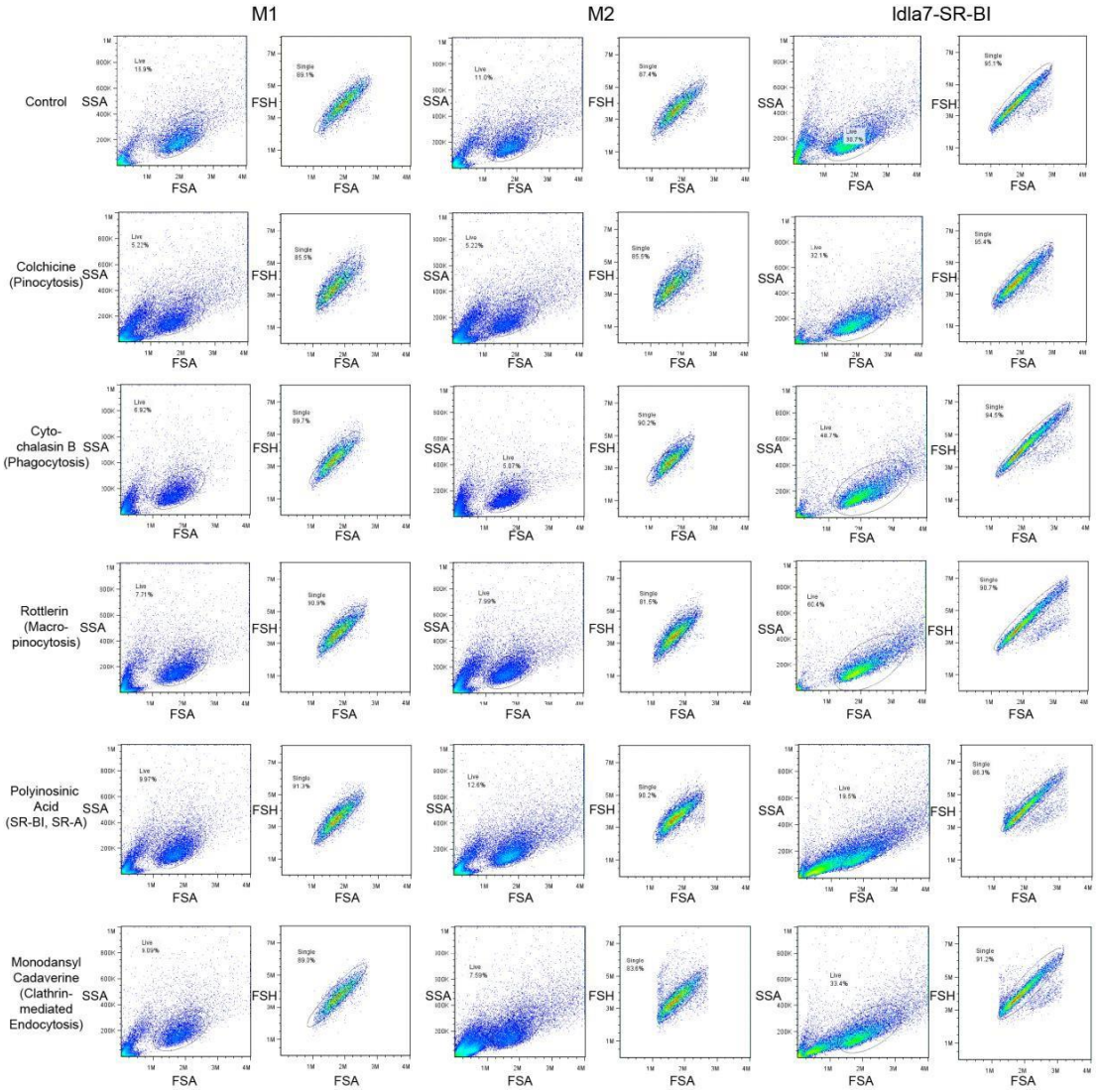

Figure S 15. Scatter plots for PEO-PBD spheres-PKH67 shown in Figure 6F. SSA = side scatter area. FSA = forward scatter area. FSH = forward scatter height.

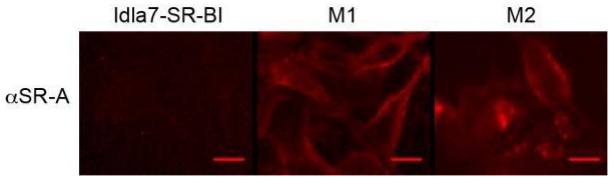

Figure S 16. Idla7-SR-BI cells do not express SR-A. Fluorescence micrographs of Idla7- SR-BI cells, M1, and M2 murine macrophages that have been stained with an antibody for SR-A with a fluorescent secondary antibody. Scale bars are 10 microns

Chapter 3 Soft Nanoparticles and Obesity

Obesity changes the pharmacokinetics of cylindrical and lipid nanoparticles in mice with Kupffer cells and LSECs playing different roles in nanoparticle uptake depending on the state of obesity

Mitch Raith[a], Uche Anozie[a] and Paul Dalhaimer[a,b,*]

[a] Department of Chemical and Biomolecular Engineering

[b] Department of Biochemistry, Cellular, and Molecular Biology

University of Tennessee

Knoxville, TN 37996

Correspondence: Paul Dalhaimer

Email: pdalhaim@utk.edu

Abstract

Understanding the mammalian response to nanoparticles (NPs) in an obesity environment is an unmet crucial need in nanomedicine because more than two-thirds of adults in the U.S. are overweight to obese. Thus, patients that will be treated with nanoparticles (NPs) will have Nonalcoholic Fatty Liver Disease (NAFLD) and chronic inflammation. Yet, NP pharmacokinetics (PK) and toxicity (TOX) are determined in lean rodents with healthy livers and low inflammation. Thus, we have little understanding of how NPs will behave in a metabolically realistic environment. To bridge this knowledge gap, we determined the PK and TOX of PEG-based cylindrical nanoparticles (CNPs) and lipid-based nanoparticles (LNPs) as a function of diet- and genetic-induced obesity in *ob/ob* and wild-type mice. *ob/ob* mice lack the hormone leptin, which gives mammals the sensation of being “full” after eating. In PK studies, CNPs localized to fatty livers in *ob/ob* mice on a high-fat diet (HFD) more quickly than to healthy livers in *ob/ob* mice on a restricted low-fat diet (LFD). LNP liver signal PK is greatly affected by mouse weight. LNP liver signal peaks 6 hours post-injection in lean mice, 24 hours post-injection in heavy mice, and 48 hours post-injection in obese

mice. We next aimed to determine the reasons for these observations. In lean mice, most NPs rapidly localize to Kupffer cells (KCs) and liver sinusoidal endothelial cells (LSECs) after intravenous injection. But the distribution of NPs between these liver cells is unknown in both lean and obese mice. In lean mice, clodronate liposome-induced depletion of KCs decreased both CNP and LNP liver localization, with a much stronger reduction in CNP localization. MCT-induced depletion of LSECs increased CNP liver localization and decreased LNP liver localization. This suggests that CNPs interact more strongly with KCs than LSECs and that LNPs interact with both KCs and LSECs. These experiments were not possible in obese mice because of lethality. To determine why CNP localization to fatty livers is higher than to lean livers, we focused on the expression of SR-BI, which binds CNPs and causes CNP cellular uptake. SR-BI expression was increased in *ob/ob* mice fed HFD. SR-BI was also increased in RAW 264.7 murine macrophages cultured in HFD conditions. The marker of macrophage activation CD86 was also upregulated in both obesity conditions over lean controls. Thus, we see that SR-BI and CD86 expression differences may play a role in increased CNP liver localization. To determine if obesity-driven inflammation played an additional role in CNP liver localization, we administered the leaky-gut endotoxin lipopolysaccharide (LPS) to wild-type mice on LFD. LPS triggers inflammation in obese mammals. LPS increased the liver localization of CNPs but decreased the liver localization of LNPs. Therefore, LPS-induced inflammation plays a role in the increased CNP localization to the liver. CNPs and LNPs reduced most cytokine and chemokine levels that were elevated in obese *ob/ob* mice. Interestingly, CNPs and LNPs greatly increased IL-5 levels which promotes the survival, differentiation, and chemotaxis of eosinophils.

3.1 Introduction

For the first time in history, nanoparticles have been used in the clinic on a mass scale [2]. This is due to the development of lipid nanoparticles (LNPs) that carry RNA. Recent success of the Pfizer and Moderna covid-19 vaccines has seen LNPs administered to hundreds of millions of patients on a global scale[6]. But, before academia and industry invest billions of dollars in this technology, we must understand how they affect mammalian physiology at the cellular level. For the better part of forty years, the development of NP drug delivery has failed to make a large impact on medicine. This is due in large part to the continued failure of NP based drug delivery in human clinical trials [7]. The development of any NP based therapy will involve the use of small animal preclinical trials [31]. The knowledge gained from these mouse experiments has provided a glimpse into NP performance in humans. However, NP cures for human diseases remain rare [2]. Many NP technologies appear to have impressive efficacy in lean, young mice, but fail in human clinical trials [32]. We postulate that a reason for this is that the mice being used in these experiments have near-ideal metabolic states (in leu of the disease model) whereas the human patients that will receive the NP therapy in the clinic will be overweight to obese. Indeed, the number of overweight and obese people in the US has increased dramatically over the past three decades. At least 65% of hospital patients that could be treated with NP technologies will be overweight to obese [33]. Yet, NP pharmacokinetics (PK), toxicity (TOX), and efficacy are tested in lean – not obese – mice. We postulate that obesity will greatly affect nanoparticle PK, TOX, and efficacy. This is an especially valid concern because the immune system, which strongly interacts with NPs, is greatly affected by obesity.

Obesity and immune response converge at the liver. The liver is also the major center for nanoparticle clearance from the blood stream [34]. Thus, it is our focal point. Upon the onset of the obesity associated metabolic disorder, Nonalcoholic Fatty Liver Disease (NAFLD), the liver undergoes massive changes. A lean liver is comprised of hepatocytes, stellate cells, resident macrophages (Kupffer Cells, KCs), and liver endothelial sinusoidal cells (LSECs, sinusoids). Obesity drives changes in each cell population. Hepatocytes become overwhelmed with fat storage and can no longer preform their native functions [35]. Stellate activation upon the onset of fatty liver causes the formation of scar tissue [36]. LSECs also undergo injury during the very early stages of fatty liver development [27]. While most of the liver is injured during the progression of fatty liver, KCs are activated [27] [37] .Additionally, macrophages are recruited to the liver [38]. Increased liver macrophage activity associated with fatty liver is due to increased obesity associated endotoxemia [39]. We hypothesized these changes would dramatically alter NP behavior and created a need to study NPs administered to an obese mouse.

To study the effects of obesity on NPs, we choose to use polymeric cylindrical nanoparticles because they demonstrate better drug delivery properties than spherical NPs [40] [5]. Additionally, we used PEGylated liposomes as a control. This is because the FDA approved cancer treatment Doxil uses PEGylated liposomes to delivery doxorubicin [8]. We also had to generate mice of different weights. This was accomplished using a combination of controlled diet and a leptin deficiency model (ob/ob mice). Leptin deficient ob/ob mice were preferred over KK/A^y to generate obese mice at a consistent young age. Mice were tail vein injected with dyed NPs and studied for 48hrs.

Our data show significant shifts in the localization of polymer-based cylindrical NP micelles “filomicelles” (CNPs) and FDA-approved liposomal NPs (LNPs) in the livers of obese mice versus lean counterparts. Obese mice can remove CNPs from circulation faster while LNPs are removed slower compared to lean counterparts. Therefore, mammalian response to NPs is different in obese versus lean mice. We postulate this is due to a preference for liver sinusoids to uptake spherical NPs such as liposomes vs elongated cylindrical NPs. We probed this by doing chemical depletion of KCs and LSECs in lean mice prior to NP injection. KC depletion greatly affects liver uptake of CNPs while both KC and LSEC depletion affect liver uptake of LNP. Macrophages, specifically KCs, can uptake NPs of either geometry while LSEC prefer the smaller LNP. During obesity and the onset of fatty liver, sinusoids are damaged while macrophage population in the liver is increased. Thus, allowing fatty liver to remove CNPs at an increased rate, while LNPs are removed at a decreased rate. Toxicity studies were also done to determine if NPs pose a threat to further detriment the health of obese patients. Cytokine analysis determined no noticeable damaging effects.

3.2 Materials and Methods

3.2.1 Nanoparticles

PEO_{56}-PBD_{46} diblock copolymers that assembled into CNPs were synthesized by Namgoo Kang and Jimmy Mays. CNPs were formed by film rehydration and dyed as previously described [40].

LNPs were purchased from ForumuMax (#f30204b-c). LNPs closely resemble the liposomes used in the clinical cancer treatment Doxil. Both CNPs and LNPs were diluted in PBS to 3.33 mg/ml prior to injection.

3.2.2 Mouse Experiments

All experiments were performed under the guidelines of the University of Tennessee's IACUC protocol #2231. B6.Cg-*Lep*^{ob}/J mice were purchased from Jackson Laboratories (#000632) and bred in house. Mice were genotyped with tail snip PCR analysis using the protocol suggested by Jackson Laboratories. Litter mates were used as experimental controls. Mouse weight was manipulated with diet. At 5-7 weeks, genotyped ob/ob or wt mice were placed and individual cages and fed a controlled diet for 6 weeks. Research Diets 60% fat diet (#D12492) was used for HFD and Purina Rodent Chow (#5001) was used for LFD. 100 ml of 3.33 mg/ml NP solution in PBS was tail vein injected into the mice via a 28-guage insulin needle (BD # 329461). Mice were euthanized at the described times, ranging from 2 to 48hrs.

3.2.3 LSEC/KC Depletion

LSEC depletion experiments were carried out with an IP injection of MCT 48hrs prior to the NP IV injection. MCT (Selleck Chem, #S3812) was dissolved in DMSO and diluted with PBS such that 500 ml delivered a 250 mg/kg dose to a mouse. Injection was done in the lower right quadrant of the abdomen and the needle was aspirated to ensure no structures were punctured. Control experiments were done with PBS containing DMSO.

KC depletion was done by IV injection of clodronate liposomes (FormuMax, #F70101C-N) 48 hours prior to the NP IV injection. 200 mL of clodronate liposome was injected as is with no dilution. Control experiments were conducted with an unloaded control liposome (FormuMax, #F70101-N).

Animals treated with either chemical agent were observed closely during the 48-hour incubation period.

3.2.4 LPS induced inflammation

LPS (Sigma, #L2630) was dissolved in PBS to a working concentration of 0.2 mg/ml and 500 ml was injected into the IP cavity of healthy weight mice. PBS containing no LPS was used as the control. After 6 hours, the mice were tail vein injected with NPs and euthanized after 2 hours.

3.2.5 In Vivo Imaging

The day of injection the mice had the hair on their stomach removed with depilatory cream. Mice where anesthetized with isoflurane via the open drop method. Body heat was maintained with a heating pad while Nair was applied. After 45 seconds, the cream was removed with damp gauze and the bare abdomen was dried off. Mice were then injected with either CNP or LNP. At 0.5, 2, 6, 24, and 48 hours, the mice were imaged. Mice were first deeply anesthetized with an isoflurane vaporization chamber. Mice were imaged with an IVIS Lumina K. The stage was heated to 37°C to maintain mouse body temperature.

Mice with euthanized at 48 hours using isoflurane followed by cervical dislocation. Organs were removed and imaged using the IVIS.

3.2.6 Histology

Immediately after euthanasia, the hepatic portal hepatic portal vein was catheterized with a 23gauge butterfly needle. Using a Harvard apparatus, 15 mL of PBS was flowed at 2 mL/min to flush the liver. 10% neutral buffered formalin was then flowed for 1hr at 0.5ml/min. After fixation, livers were stored in 70% ethanol. Slides of the right lobe were made by Ridge Microtome (Knoxville, TN).

3.2.7 Toxicity Studies

Mice where prepared on diet as previously described and injected with NPs when noted. After 48 hours, the mice with deeply anesthetized and blood was harvested via cardiac puncture using a 23-guage needle. ~500 ml of blood was harvested in a lithium heparin serum separator tube (BD, # 365985) and centrifuged at 1300g for 5 minutes. Plasma was collected and set to Eve Technologies (Calgary, AB, Canada) for analysis.

3.2.8 Mammalian Cell Culture

M0 RAW 264.7 macrophages (ATCC; #TIB-71) were polarized into M1 macrophages as previously described (Raith et al 2021). Macrophages were maintained at 5% CO_2 and 37^{o}C in DMEM supplemented with 10% FBS and 1% penicillin-streptomycin.

3.2.9 qRT-PCR Gene Analysis

Cells were seeded in 6 wells plates such that they reach ~75% confluence after 18 hours. At this point oleic acid or PBS was added in the described concentration. After 24 hours, the media was removed, and the wells were washed 3 times with sterile PBS. RNA was extracted with a Qiagen RNeasy mini prep kit (#74004). qRT-PCR Primers for CD86 and SCARBI were purchased from Sino Biologicals (#MP200099,#MP200340). Reactions were carried out using a 1 step kit (Applied Biosciences, #4391178) in a BioRad CFX. Analysis was carried out using LinRegPCR.

3.3 Results

This study involved the use of 2 NPs. The first was lab synthesized PEO-b-PBD co-block polymer cylindrical nanoparticles, CNPs. Previously work has demonstrated these to have favorable PK profiles compared to spherical NPs, both polymeric and liposomes [5], and to interact directly with the major HDL report SR-BI [40]. The second NP was a LNP resembling the PEGylated liposomes in the FDA approved cancer treatment Doxil.

In order to the study the effects of weight on the PK profile of CNP and LNP, we had to generate mice of different weights. This was done via the use of a leptin deficient mouse model (*ob/ob*) abd wild type C57Bl/6 mice and a high fat vs low fat diet. The combination of genotype and diet was manipulated to generate mice in 4 different weight classes (Figure 8A,B). Wild type mice on either LFD or HFD produced relatively normal weighted animals (23.9g vs 27.1g) with only a slight increase in liver size among HFD fed animals (0.87g vs 1.05g). It should be noted the ratio of liver weight to total animal weight was similar (27.5 vs

25.8). H&E staining of the right liver lobe also shown no significant changes in liver structure, and importantly, no increase in the fat deposits seen in the liver. In leptin deficient mice, feeding an unlimited HFD leads to gross weight gain (54.8g). These mice are referred to as obese mice. Feeding *ob/ob* mice a restricted LFD (4g/day) diet leads to modest weight gain (38.0g) compared to normal weight animals. These are referred to as heavy mice. Analysis of the right liver lobe with H&E staining also shows heavy mice have increased liver fat deposits compared to healthy weighted animals, but a significant amount less than livers from obese mice. Livers from all four combinations of diet and genotype were analyzed for the expression of the pro inflammatory protein IL-1β (Figure 8E). Weight gain shows an increase in IL-1β expression, signifying obesity leads to liver inflammation. Although not the main aim of this study, we did note that leptin deficiency dramatically decreases the size of the spleen. This phenotype can then be partially recused with obesity, suggested that weigh gain may be associated with increased splenic mass. This was not investigated further. (Figure S17).

10 (5m and 5F) mice of each genotype and diet combination were injected with either CNP or LNP labeled with NiR dye (Figure 9A). At times of 0.5, 2, 6, 24, and 48hrs, the mice were imaged using an IVIS *in vivo* imaging system (Figure 9B). Obese mice injected with CNP were able to remove the NPs from circulation at an increased rate (Figure 9C). Tracking the liver signal over the 48hr experimental period shows that LFD fed WT, HFD fed WT, and LFD fed *ob/ob* mice injected with CNP behaved similarly, with the highest liver signal reached at the end point (Figure 9C, F). A positive derivative at 48hr signifies livers were not yet saturated and still removing CNP from circulation. Obese mice injected with CNP reached saturation after 24hrs. Mice injected with LNP did not behave similarly. As mouse

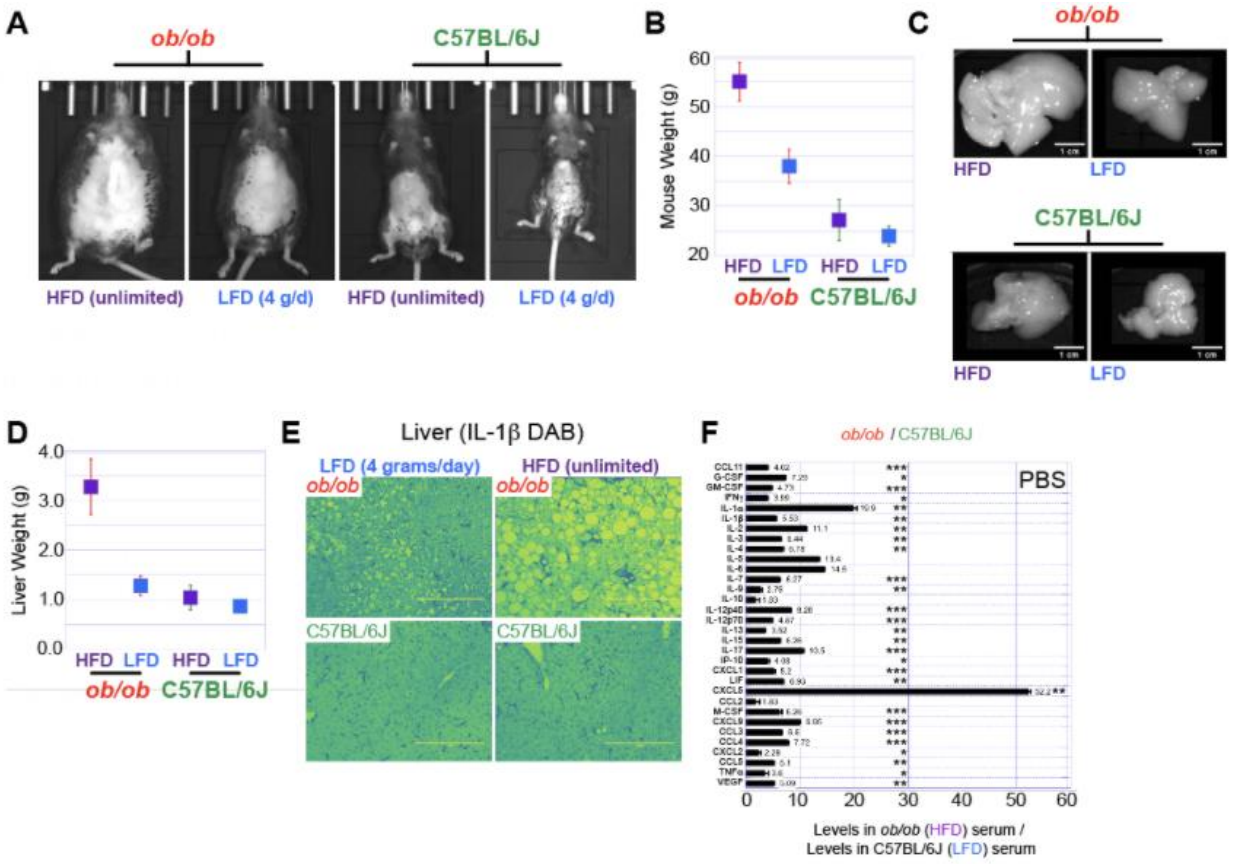

Figure 8. Diet and leptin deficiency can be manipulated to generate mice of varying weights. (A) Pictures of mice with and without leptin deficiency fed with HFD or LFD. Resulting mice were obese, heavy, or normal weighted. Data for the weights is shown graphically in (B). (C) Generating obese mice causes the development of fatty liver. Obese mice had expanded livers compared to all other mice. Liver weight data is shown graphically in (D). (E) DAB staining of IL-1β shows obese mice have elevated levels of inflammation. It also shows that obese mice have more fatty deposits in their livers. Heavy mice had some fatty deposits while WT mice on LFD or HFD had none. (F) Obesity increases the plasma levels of many pro inflammatory cytokines compared to lean animals.

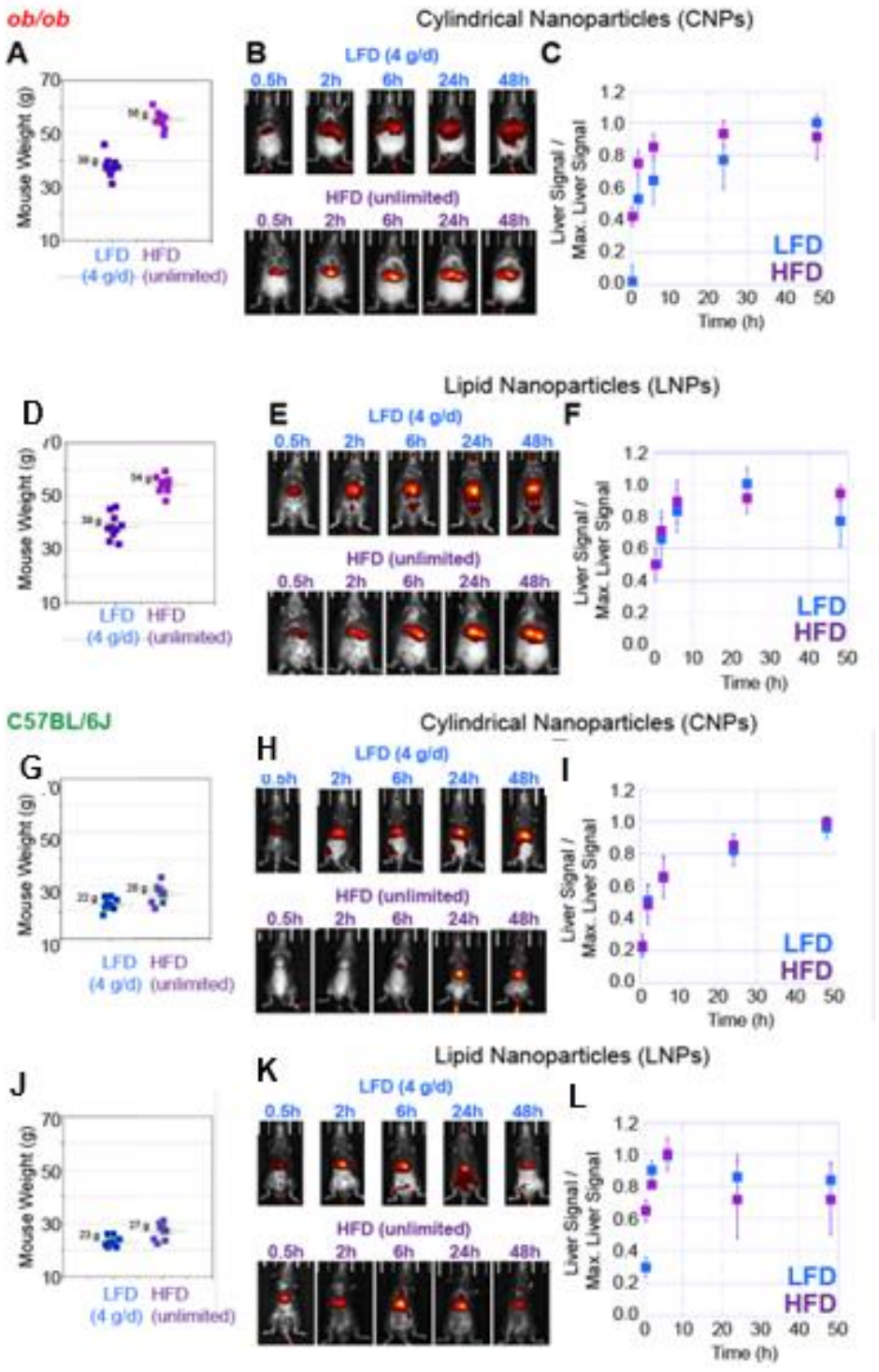

Figure 9. In vivo liver uptake of CNP is increased in Obese Mice. (A-C) ob/ob mice on HFD vs LFD (obese vs heavy) injected with CNP. Obese mice can localize CNP to the liver after 24hrs. Heavy mice are still removing CNP at 48hr. (D-F). ob/ob mice on HFD vs LFD (obese vs heavy) injected with LNP. Heavy mice livers are saturated at 24hr while obese mice livers have max signal at 48hrs. (G-I) Wild type mice on LFD HFD behave almost identically. Livers are still removing CNPs at 48hrs. (J-L) WT on HFD or LFD saturate at 6hrs.

weight increased, the time to remove LNPs from circulation increased. Lean animals were able to remove LNPs from circulation after 6hrs. Heavy and obese animals appeared to have longer circulation times with peak liver signals at 24 and 48hrs respectively (Figure 9 G-L).

After 48hrs, the mice were euthanized, and the major organs were analyzed as previously described [40]. Blood volumes for the heavy and obese animal were calculated assuming a mouse twice the body weight of a lean animal had 125% the blood volume [41]. After 48hrs, the fraction of CNP in the liver was roughly 10% higher in the obese animals. All other weighted mice had similar liver fractions. Plasma fraction was inversely related to liver fraction. Obese animals had roughly half the fraction of WT mice on either LFD or HFD when injected with CNP. Weight didn't appear to influence the biodistribution of LNP 48hrs post injection. All four animals injected with LNP had similar liver fractions and low plasma fraction. For both CNP and LNP injected animals, the spleen signal of ob/ob animals on LFD was decreased. The NPs appear to have been diverted to the plasma. (Figure 10)

As expected, the liver is the organ largely responsible for removing NPs from circulation. Within the liver, there exists several cell types, but we have focused on LSECs and KCs. These cell types have been shown to be the dominant cell types for nanoparticle uptake in the liver [24] [22] [25] [23]. We examined the results of chemical depleting LSECs and KCs *in vivo* followed by NP injection[42]. Lean WT animals fed LFD diet were used for all experiments. KCs were depleted with Clodronate liposomes (CL) followed by a 48hr incubation period before injection with NPs (Figure 11 A, D). Control mice were injected with

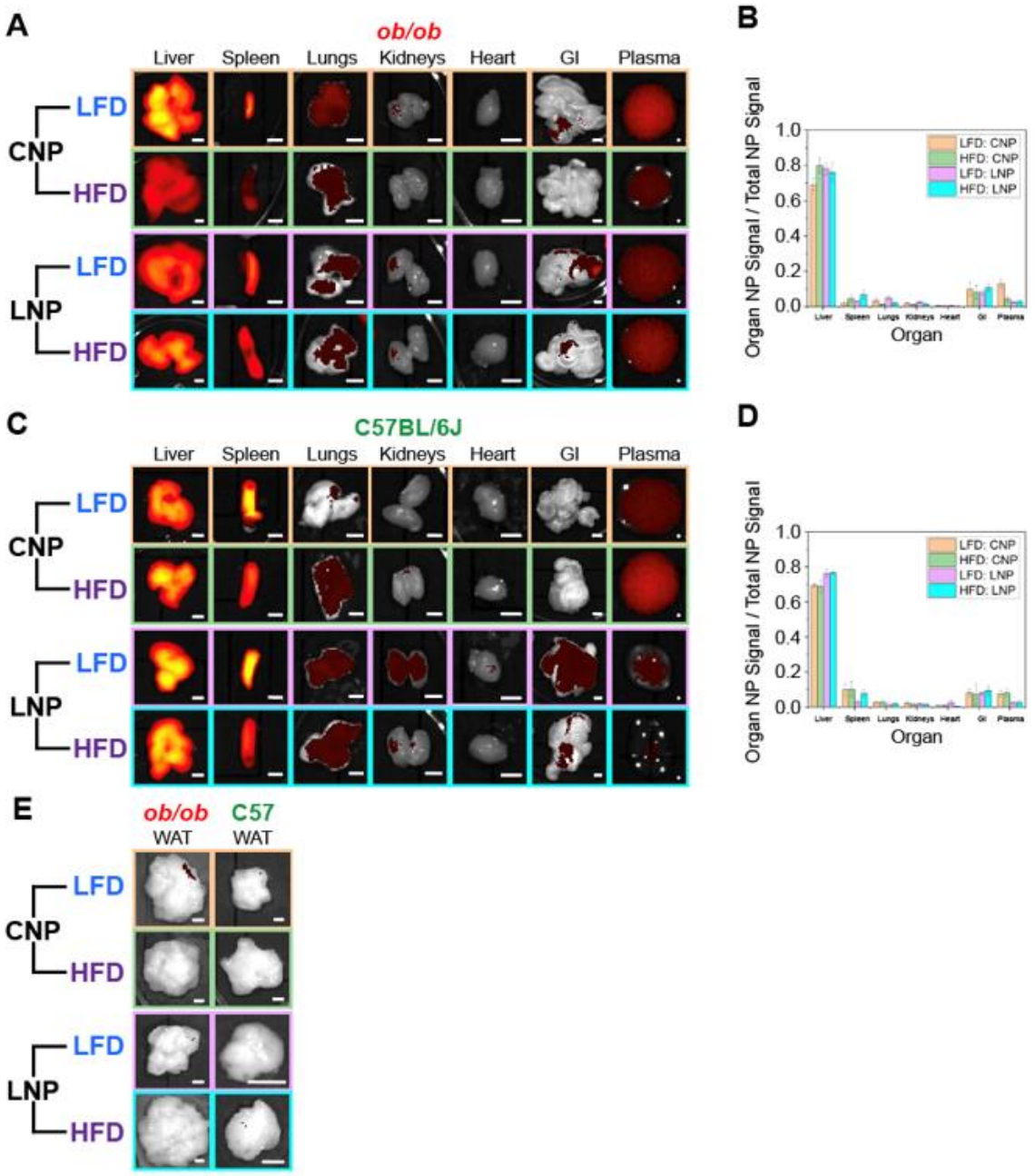

Figure 10. Effects of obesity on the 48hr distribution of CNPs and LNPs. (A-B). Organs from heavy and obese mice 48 hrs after CNP or LNP. Please note obese livers are expanded and the signal appears diluted in images. Analysis and graphical representation of the signals (B) shows CNP injected obese livers have increased signal fraction. (C-D). Organs from WT mice injected with CNP or LNP on HFD or LFD. Diet has no impact on the biodistribution of either NP in normal weighted animals. (E) Neither LNPs or CNPs localize to adipose tissue in obese, heavy, or lean mice.

unloaded liposomes. LSECs were depleted with intraperitoneal monocrotaline (MCT) injection followed by 48hr incubation period. Control mice were injected with PBS. NPs were injected and mice were euthanized after 2hrs. CL treated mice injected with CNP had a decreased liver fraction from 72% to 25%, about a 3fold decrease (Figure 11C). A corresponding 3fold increase in the plasma fraction, from 11% to 32%, was also seen after CL treatment. MCT treated mice injected with CNP didn't show any decrease in the liver faction, but instead a slight increase from 64% to 74% (Figure 11B). Plasma fraction was also decreased from 12% to 4%. Repeating the experiments with LNP injected mice yielded different results. Both depletion of KC and LSEC lead to a modest decrease in liver fraction. CL injection decreased liver fraction from 75% to 64%. MCT decreased liver fraction from 73% to 49%. (Figure 11 D-F).

Our lab has previously discovered SR-BI is an important factor in the localization of CNP to the liver of mice [40]. The role of SR-BI in the in the increased rate of liver localization of CNP in obese had to be investigated. Studies done on the expression levels of SR-BI were done both in vitro utilizing RAW 264.7 murine macrophages and in vivo with HFD mice. In vitro experiments were carried with and without the presence of oleic acid in the media. Mouse experiments were carried with ob/ob mice (n=4 for each condition) on both LFD and HFD. After 6 weeks of diet, the liver was removed, and the RNA was extracted. For *both in vitro* and *in vivo* experiments, the high fat condition led to an increased expression of SR-BI (Figure 12 A, B). We also looked at CD86, an indicator of proinflammatory M1 macrophage activity, levels in the same samples and saw increased expression levels that closely paralleled SR-BI expression (Figure 12 C, D). Because of this, we wanted to explore the

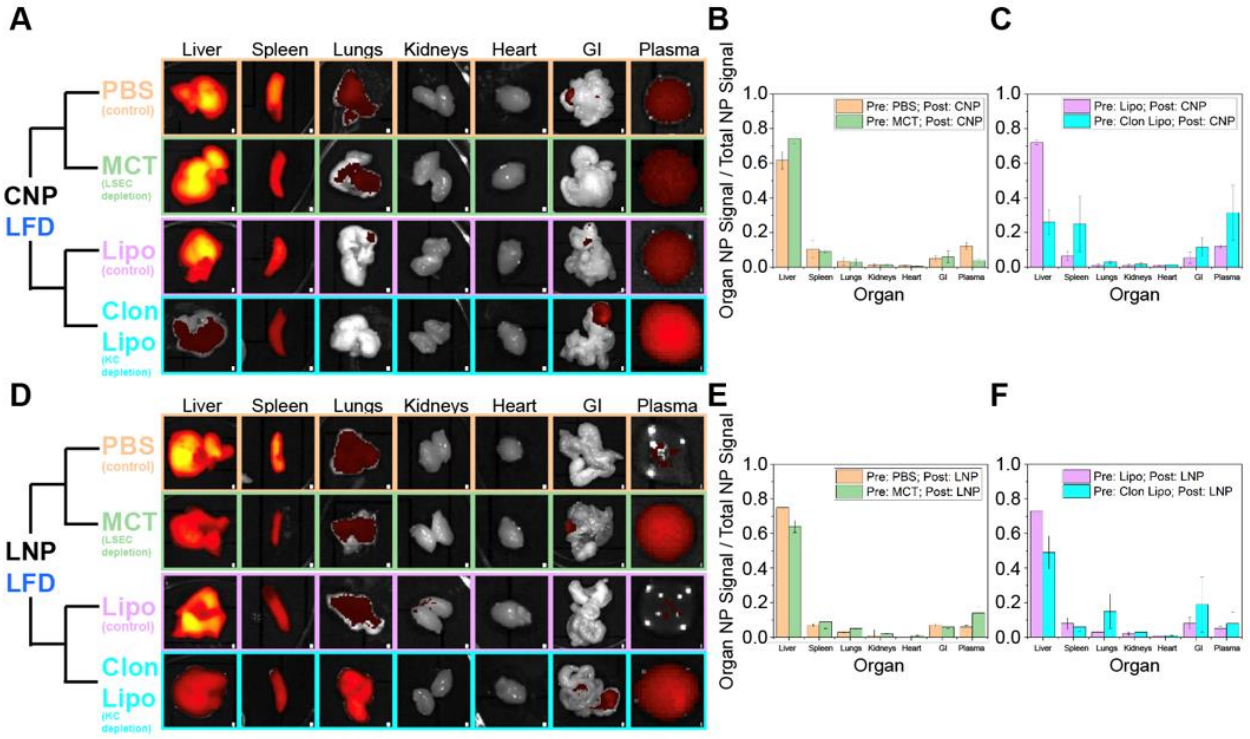

Figure 11. Chemical Depletion of LSEC and KC. (A-C). Lean mice were treated with either MCT or Clodronate liposomes to chemically deplete LSECs or KCs respectively before CNP injection. Only CL was able decrease liver signal fraction 2 hours after injection, suggesting CNPs go to KCs. (D-F) The experiment was repeated with LNP. MCT and CL decrease liver fraction of LNP. This suggests LNP goes to both LSEC and KCs.

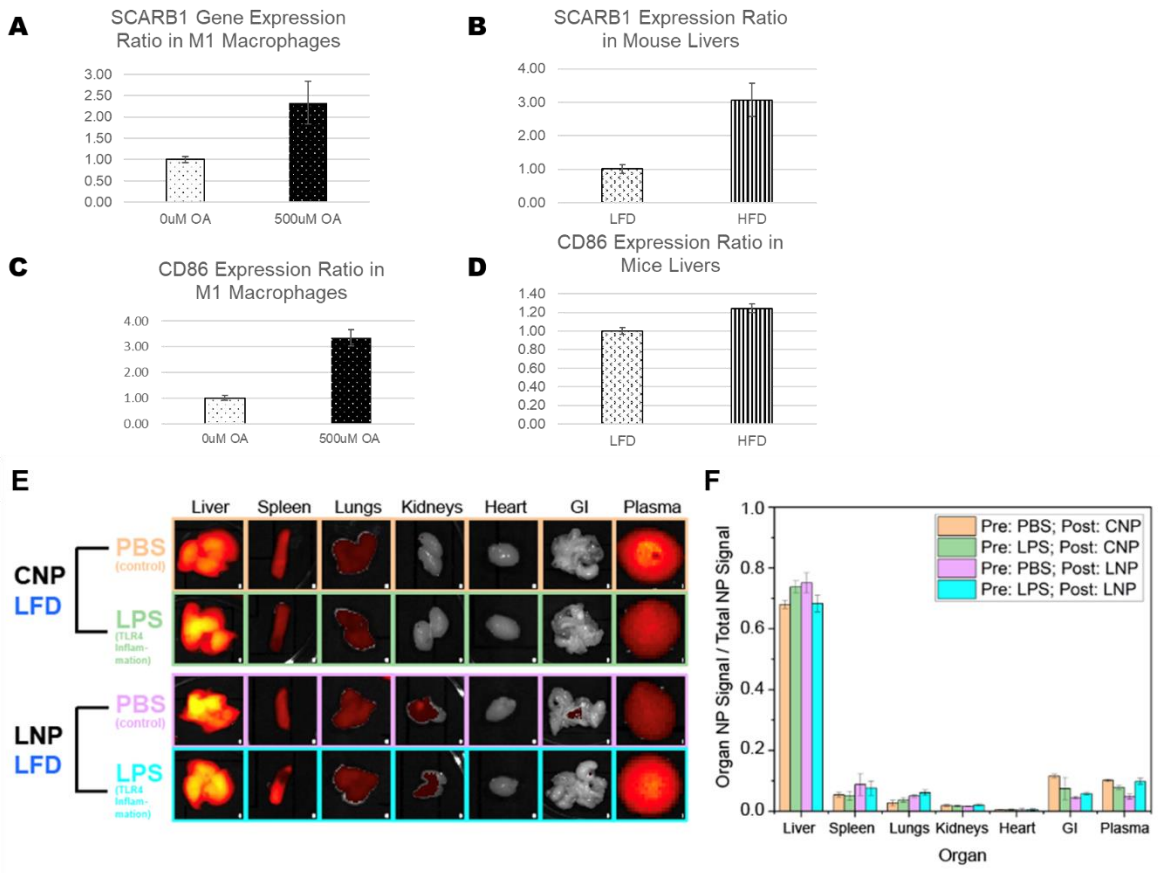

Figure 12. Obesity may promote biochemical factors that contribute to CNP localization to the liver. SCARBI, the gene responsible for SR-BI, was analyzed for gene expression changes caused by high fat both in vitro (A)and in vivo (B). Both experiments showed increased expression of SCARBI. (C-D) Similar experiments were done analyzing CD86.(E-F) LPS was then administered to lean mice to induce inflammation. Inflammation increased CNP localization to the liver 2hrs after injection. Obesity associated inflammation may directed CNPs to the liver.

possibility obesity associated inflammation [43] [44] [45] was contributing to increased CNP uptake. 100ug of LPS was administered via IP injection to the lean WT animals on LFD diet to induce inflammation. Control mice were injected with sterile PBS. 6hrs after IP injection, the mouse was tail vein injected with either CNP or LNP. 2hrs post IV injection (8 hours total from LPS administration), the mouse was sacrificed. Analysis of the organs shown an increased liver fraction of CNP in the mice injected with LPS. LPS injected caused a decrease in LNP liver fraction. (Figure 12E, F)

As obesity leads to a general decline in health, it is important to know if a metabolically imbalanced patient would be able to withstand treatment with NPs. Slides were prepared of the right lobe from lean and obese animals injected with PBS, CNP, or LNP. NPs didn't appear to negatively affect liver health of any animal. Fatty liver in LNP injected obese mice appears to be mildly alleviated. Cytokine levels also support improved patient health in NP injected obese animals. LNP and CNP increased the plasma concentration of cytokines associated with cell proliferation, namely IL-5 and IL-2. (Figure 13).

3.4 Discussion

Since the FDA approval of the mRNA Covid-19 vaccines, the largest scale administration of a nanoparticle carried therapy has been carried out. Although interest in developing nanoparticle delivered drugs has dated back to the 1980s with liposomal anesthesia agents, there remains very few FDA approved nanoparticle treatments. As of 2021, 32 nanoparticles have been authorized for FDA use [2]. Most approved NP treatments involve liposomal cancer agents.

Figure 13. Toxicity Study of obese and lean mice injected with CNP or LNP. (A) H&E staining of obese mouse livers injected with PBS, CNP, or LPN. Fat globules in LNP appear smaller. (B)H&E mouse livers injected with PBS, CNP, or LNP. No difference is noticeable. (C-F) Analysis of obese and lean mouse plasma before and after NP injection.

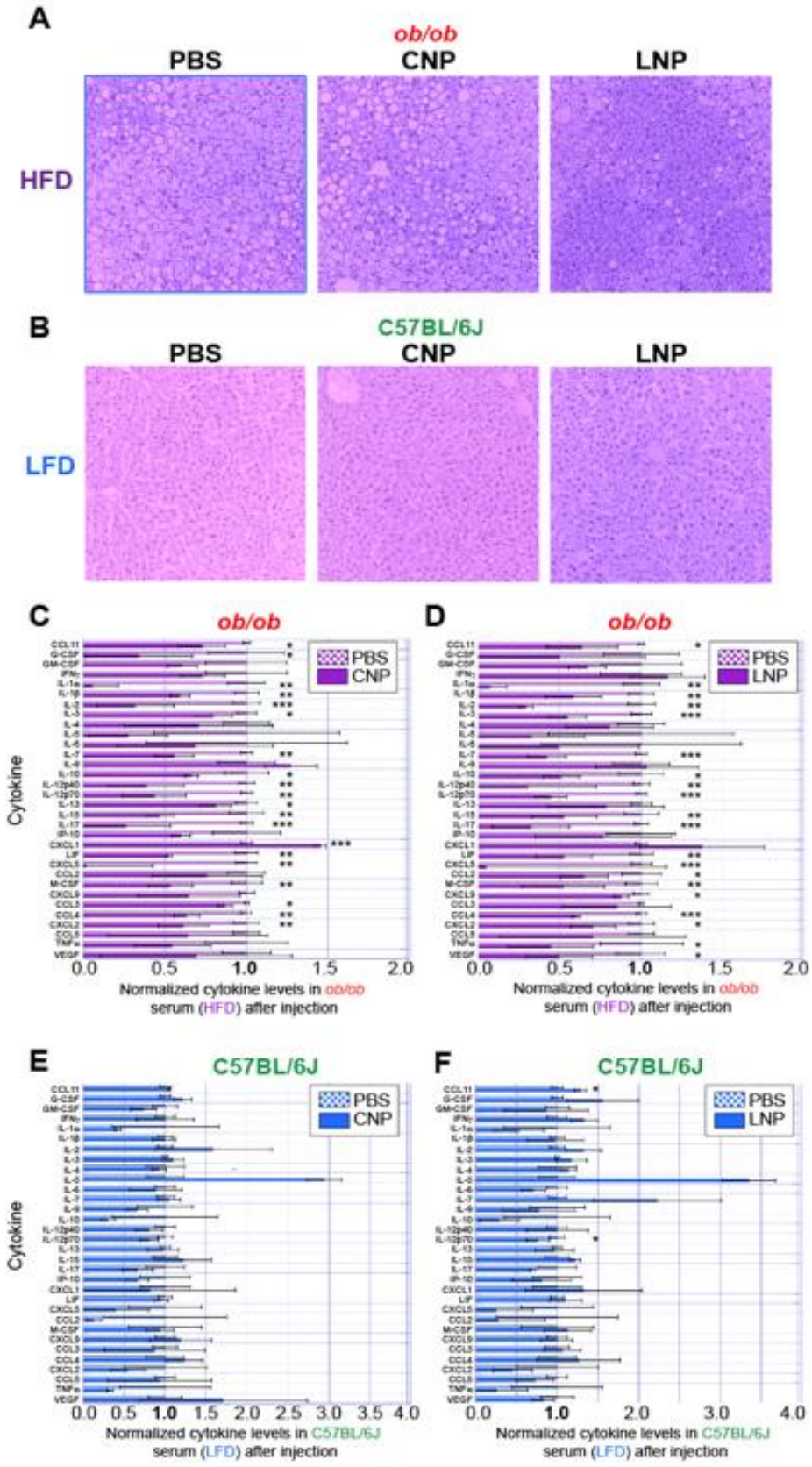
A
ob/ob
PBS
CNP
LNP
HFD
B
C57BL/6J
PBS
CNP
LNP
LFD
C
ob/ob
PBS
CNP
Cytokine
0.0 0.5 1.0 1.5 2.0
Normalized cytokine levels in ob/ob serum (HFD) after injection
D
ob/ob
PBS
LNP
0.0 0.5 1.0 1.5 2.0
Normalized cytokine levels in ob/ob serum (HFD) after injection
E
C57BL/6J
PBS
CNP
Cytokine
0.0 0.5 1.0 1.5 2.0 2.5 3.0 3.5 4.0
Normalized cytokine levels in C57BL/6J serum (LFD) after injection
F
C57BL/6J
PBS
LNP
0.0 1.0 2.0 3.0 4.0
Normalized cytokine levels in C57BL/6J serum (LFD) after injection

One reason for the lack of FDA approved NP based therapies is the failure rate in clinical trials [7]. We postulate this is because many small animal trials do not accurately represent the patient population in terms of obesity rate. The current obesity rate amongst adults in the United States is 42% according to the CDC. This number is expected to grow, meaning over half of the patient population will be obese. To get a realistic representation of the patient population, small animal models most employ the use of obese animal models.

To generate an obese mouse, the commonly used approaches include diet induced obesity (DIO) in C57BL/6J mice [46], leptin deficiency [47], and hormonal weight gain [48]. We choose to use leptin deficiency overfed with HFD as our model of obesity. This is because obesity and fatty liver can be observed in 6 weeks. DIO in C57BL/6J mice and hormonal weight gain in KK-A^y take on the order of several months to develop obesity [46] [48]. We wanted to use mice around 3 months of at the end point of our experimentation to avoid any affects from age. Leptin deficient mice will gain weight even on LFD. Because of this, it was imperative mice be placed on either LFD or HFD at 5-7 weeks old for 6 weeks. This allowed weight gain of *ob/ob* to be controlled on a restricted LFD and prevent gross weight gain.

While administering NPs to the animals, we decided to use a constant dosage across all animals for consistency. When analyzing the *in vivo* imaging, it became apparent a system had to be developed to analyze the data. The expanded size of obese livers made them more visible to the IVIS imaging system, and they consistently had higher values than lean livers. To overcome this, the NP signal for each *in vivo* time point was divided by the max

signal seen during the 48hr imaging period. This allowed us to determine the kinetics of NP localization to the liver and the saturation point of the liver.

We saw that obese animals injected with CNP were able to rapidly localize the NPs to the liver. Conversely, LNP had an increased time to liver saturation. We postulate this is because of a preference of LSEC to uptake the smaller LNPs. CNPs have a diameter of 50nm but can be microns long in length. The LNPs are 40-80nm diameter spheres. LSECs preform liver filtration function by performing pinocytosis. Roughly half of the pinocytic vesicles in the liver are within LSECs [49] while LSECs consist of ~10% of the liver cell mass [50]. Pinocytotic vesicles are around 100nm in diameter. Even a coiled up CNP cannot be entrapped in a pinocytotic vesicle because of its length dimension. Although CNP are flexible and can assume a coiled shape, shape appears to hinder LSEC driven liver uptake of CNP *in vivo*. Chemical depletion of LSEC prior to CNP or LNP injection agreed with this postulation. While MCT pretreatment caused a decrease in the fraction of LNP in the liver, it led to increased CNP. KCs remain after treatment with MCT. We hypothesize these cells interact predominantly with CNP and are responsible for liver localization of CNP. Previous work in the lab has shown that murine macrophage cultured *in vitro* are able to uptake CNP via phagocytosis [40]. Complementary experiments with chemical depletion of KCs further confirm this hypothesis. CNP localization in the liver was affected more by KC depletion than LNP liver localization.

It is possible the attraction to KCs is mediated through the CNP-SRBI interaction previously probed [40]. A healthy liver consists of 4 main cell types. Hepatocytes, stellate cell, LSECs,

and KC. Obesity causes changes each of the cellular populations upon the onset of fatty liver. Hepatocytes have to store excess fat in the liver, stellate cells become scar tissue [51], LSEC undergo injury [27], and KCs are repolarized to the inflammatory state [52]. Additionally, macrophages are recruited to the liver because of leaky gut derived inflammation [26]. These leaves macrophages as the only protected cell population that can effectively remove NPs from circulation. The gene expression analysis conducted on CD86, a marker of M1 activation, confirms the activity of M1 macrophages is increasing in the liver of obese mice. Unsurprisingly, HFD also lead to the increased expression of SR-BI. Expression of SR-BI and CD86 have previously been linked [53]. These findings further contribute to the conclusion increased macrophage activity is driving increased uptake rate of CNP in obese livers.

3.5 Conclusion

We show that cellular destination within the liver of an IV administered NP, is based, at least partially, on NP geometry. Elongated polymeric CNP cannot effectively enter LSEC, causing them to favor phagocytic KC. The smaller and spherical LSEC can enter both KC and LSEC. This has major implications in obesity because of LSEC injury and KC proliferation. The modulated activity of KC and LSEC in NAFLD causes the increased uptake of CNP and decreased uptake of LNP.

References

1. Rudramurthy, G.R. and M.K. Swamy, *Potential applications of engineered nanoparticles in medicine and biology: an update.* J Biol Inorg Chem, 2018. **23**(8): p. 1185-1204.
2. Anselmo, A.C. and S. Mitragotri, *Nanoparticles in the clinic: An update post COVID-19 vaccines.* Bioeng Transl Med, 2021: p. e10246.
3. Veltkamp, S.A., et al., *A novel self-microemulsifying formulation of paclitaxel for oral administration to patients with advanced cancer.* Br J Cancer, 2006. **95**(6): p. 729-34.
4. Millard, J., F. Alvarez-Nunez, and S. Yalkowsky, *Solubilization by cosolvents. Establishing useful constants for the log-linear model.* Int J Pharm, 2002. **245**(1-2): p. 153-66.
5. Geng, Y., et al., *Shape effects of filaments versus spherical particles in flow and drug delivery.* Nat Nanotechnol, 2007. **2**(4): p. 249-55.
6. Hou, X., et al., *Lipid nanoparticles for mRNA delivery.* Nat Rev Mater, 2021. **6**(12): p. 1078-1094.
7. Hernandez-Camarero, P., et al., *Clinical failure of nanoparticles in cancer: mimicking nature's solutions.* Nanomedicine (Lond), 2020. **15**(23): p. 2311-2324.
8. Barenholz, Y., *Doxil(R)--the first FDA-approved nano-drug: lessons learned.* J Control Release, 2012. **160**(2): p. 117-34.
9. Kullenberg, F., et al., *In Vitro Cell Toxicity and Intracellular Uptake of Doxorubicin Exposed as a Solution or Liposomes: Implications for Treatment of Hepatocellular Carcinoma.* Cells, 2021. **10**(7).

10. Otto, G.P., et al., *Clinical Chemistry Reference Intervals for C57BL/6J, C57BL/6N, and C3HeB/FeJ Mice (Mus musculus).* J Am Assoc Lab Anim Sci, 2016. **55**(4): p. 375-86.
11. Alexopoulos, A.S., et al., *Impact of obesity on hospital complications and mortality in hospitalized patients with hyperglycemia and diabetes.* BMJ Open Diabetes Res Care, 2016. **4**(1): p. e000200.
12. Ouimet, M., J. Barrett Tessa, and A. Fisher Edward, *HDL and Reverse Cholesterol Transport.* Circulation Research, 2019. **124**(10): p. 1505-1518.
13. Lundqvist, M., et al., *Nanoparticle size and surface properties determine the protein corona with possible implications for biological impacts.* Proceedings of the National Academy of Sciences, 2008. **105**(38): p. 14265.
14. Pereira, H.A. and C.S. Hosking, *The role of complement and antibody in opsonization and intracellular killing of Candida albicans.* Clinical and experimental immunology, 1984. **57**(2): p. 307-314.
15. Kameka, A.M., et al., *Clodronate treatment significantly depletes macrophages in chickens.* Canadian journal of veterinary research = Revue canadienne de recherche veterinaire, 2014. **78**(4): p. 274-282.
16. Aldossari, A.A., et al., *Scavenger receptor B1 facilitates macrophage uptake of silver nanoparticles and cellular activation.* Journal of Nanoparticle Research, 2015. **17**: p. 313.
17. Leiva, A., et al., *Mechanisms regulating hepatic SR-BI expression and their impact on HDL metabolism.* Atherosclerosis, 2011. **217**(2): p. 299-307.
18. Covington, J.D., et al., *Intramyocellular Lipid Droplet Size Rather Than Total Lipid Content is Related to Insulin Sensitivity After 8 Weeks of Overfeeding.* Obesity (Silver Spring), 2017. **25**(12): p. 2079-2087.

19. Keller, M.P. and A.D. Attie, *Physiological insights gained from gene expression analysis in obesity and diabetes.* Annual review of nutrition, 2010. **30**: p. 341-364.
20. Boden, G., *Obesity and free fatty acids.* Endocrinology and metabolism clinics of North America, 2008. **37**(3): p. 635-ix.
21. Klop, B., J.W.F. Elte, and M.C. Cabezas, *Dyslipidemia in obesity: mechanisms and potential targets.* Nutrients, 2013. **5**(4): p. 1218-1240.
22. Sadauskas, E., et al., *Kupffer cells are central in the removal of nanoparticles from the organism.* Part Fibre Toxicol, 2007. **4**: p. 10.
23. Liu, Q., et al., *Use of Polymeric Nanoparticle Platform Targeting the Liver To Induce Treg-Mediated Antigen-Specific Immune Tolerance in a Pulmonary Allergen Sensitization Model.* ACS Nano, 2019. **13**(4): p. 4778-4794.
24. Yu, X., et al., *Immune modulation of liver sinusoidal endothelial cells by melittin nanoparticles suppresses liver metastasis.* Nat Commun, 2019. **10**(1): p. 574.
25. Park, J.K., et al., *Cellular distribution of injected PLGA-nanoparticles in the liver.* Nanomedicine, 2016. **12**(5): p. 1365-74.
26. Remmerie, A., L. Martens, and C.L. Scott, *Macrophage Subsets in Obesity, Aligning the Liver and Adipose Tissue.* Front Endocrinol (Lausanne), 2020. **11**: p. 259.
27. Miyao, M., et al., *Pivotal role of liver sinusoidal endothelial cells in NAFLD/NASH progression.* Lab Invest, 2015. **95**(10): p. 1130-44.
28. Valent, P., et al., *Precision Medicine in Hematology 2021: Definitions, Tools, Perspectives, and Open Questions.* Hemasphere, 2021. **5**(3): p. e536.
29. Jaacks, L.M., et al., *The obesity transition: stages of the global epidemic.* Lancet Diabetes Endocrinol, 2019. **7**(3): p. 231-240.

30. Kaushik, S. and A.M. Cuervo, *Degradation of lipid droplet-associated proteins by chaperone-mediated autophagy facilitates lipolysis.* Nat Cell Biol, 2015. **17**(6): p. 759-70.

31. da Silva Morais, A., J.M. Oliveira, and R.L. Reis, *Small Animal Models.* Adv Exp Med Biol, 2018. **1059**: p. 423-439.

32. He, H., et al., *Survey of Clinical Translation of Cancer Nanomedicines-Lessons Learned from Successes and Failures.* Acc Chem Res, 2019. **52**(9): p. 2445-2461.

33. Hossain, M.A., et al., *Recognizing Obesity in Adult Hospitalized Patients: A Retrospective Cohort Study Assessing Rates of Documentation and Prevalence of Obesity.* J Clin Med, 2018. **7**(8).

34. Ray, K., *Liver: Clearance of nanomaterials in the liver.* Nat Rev Gastroenterol Hepatol, 2016. **13**(10): p. 560.

35. Overi, D., et al., *Hepatocyte Injury and Hepatic Stem Cell Niche in the Progression of Non-Alcoholic Steatohepatitis.* Cells, 2020. **9**(3).

36. Zisser, A., D.H. Ipsen, and P. Tveden-Nyborg, *Hepatic Stellate Cell Activation and Inactivation in NASH-Fibrosis-Roles as Putative Treatment Targets?* Biomedicines, 2021. **9**(4).

37. Lanthier, N., et al., *Kupffer cell activation is a causal factor for hepatic insulin resistance.* Am J Physiol Gastrointest Liver Physiol, 2010. **298**(1): p. G107-16.

38. Miura, K., et al., *Hepatic recruitment of macrophages promotes nonalcoholic steatohepatitis through CCR2.* Am J Physiol Gastrointest Liver Physiol, 2012. **302**(11): p. G1310-21.

39. Boulange, C.L., et al., *Impact of the gut microbiota on inflammation, obesity, and metabolic disease.* Genome Med, 2016. **8**(1): p. 42.

40. Raith, M., et al., *Elongated PEO-based nanoparticles bind the high-density lipoprotein (HDL) receptor scavenger receptor class B I (SR-BI).* J Control Release, 2021. **337**: p. 448-457.

41. Yen Tt Fau - Stienmetz, J., P.J. Stienmetz J Fau - Simpson, and P.J. Simpson, *Blood volume of obese (ob-ob) and diabetic (db-db) mice.* (0037-9727 (Print)).

42. Huang, S., et al., *Local Stimulation of Liver Sinusoidal Endothelial Cells with a NOD1 Agonist Activates T Cells and Suppresses Hepatitis B Virus Replication in Mice.* J Immunol, 2018. **200**(9): p. 3170-3179.

43. Gurses, S.A., et al., *Nod2 protects mice from inflammation and obesity-dependent liver cancer.* Sci Rep, 2020. **10**(1): p. 20519.

44. Alzahrani, B., T.J. Iseli, and L.W. Hebbard, *Non-viral causes of liver cancer: does obesity led inflammation play a role?* Cancer Lett, 2014. **345**(2): p. 223-9.

45. Sun, B. and M. Karin, *Obesity, inflammation, and liver cancer.* J Hepatol, 2012. **56**(3): p. 704-13.

46. Lin, S., et al., *Development of high fat diet-induced obesity and leptin resistance in C57Bl/6J mice.* Int J Obes Relat Metab Disord, 2000. **24**(5): p. 639-46.

47. Hao, Z., et al., *Leptin deficient ob/ob mice and diet-induced obese mice responded differently to Roux-en-Y bypass surgery.* Int J Obes (Lond), 2015. **39**(5): p. 798-805.

48. Heaberlin, J.R., et al., *Obese and diabetic KKAy mice show increased mortality but improved cardiac function following myocardial infarction.* Cardiovasc Pathol, 2013. **22**(6): p. 481-7.

49. Kjeken, R., et al., *Fluid phase endocytosis of [125I]iodixanol in rat liver parenchymal, endothelial and Kupffer cells.* Cell and Tissue Research, 2001. **304**(2): p. 221-230.

50. Pfeiffer, E., et al., *Featured Article: Isolation, characterization, and cultivation of human hepatocytes and non-parenchymal liver cells.* Exp Biol Med (Maywood), 2015. **240**(5): p. 645-56.

51. Lee, U.E. and S.L. Friedman, *Mechanisms of hepatic fibrogenesis.* Best Pract Res Clin Gastroenterol, 2011. **25**(2): p. 195-206.

52. Mayoral Monibas, R., et al., *Distinct Hepatic Macrophage Populations in Lean and Obese Mice.* Front Endocrinol (Lausanne), 2016. **7**: p. 152.

53. Aldossari, A.A., et al., *Scavenger receptor B1 facilitates macrophage uptake of silver nanoparticles and cellular activation.* Journal of Nanoparticle Research, 2015. **17**(7): p. 313.

Appendix

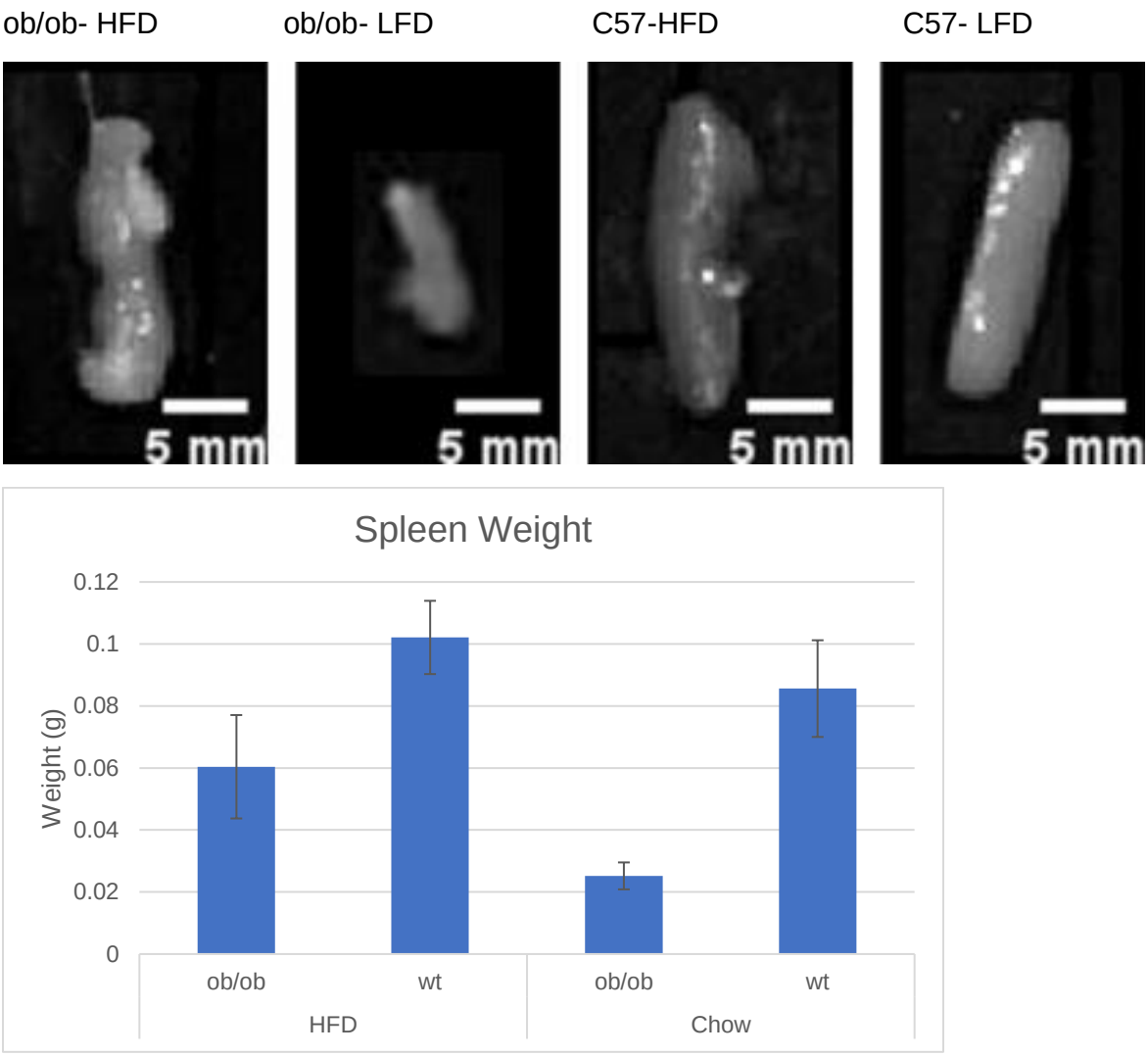

Figure S 17. Spleen size and weights with varying mouse weights.

Chapter 4 Enhanced Lipid Droplet Degradation

Enhanced lipid droplet degradation by split-intein-mediated lipid droplet targeting to lysosomes in mammalian cells

Mitch Raith[a]

Paul Dalhaimer [a,b]

[a]Chemical and Biomolecular Engineering, University of Tennessee- Knoxville, Knoxville, Tennessee, United States

[b]Biochemistry, Cellular and Molecular Biology, University of Tennessee- Knoxville, Knoxville, Tennessee, United States

Correspondence: Paul Dalhaimer, Chemical and Biomolecular Engineering, Street, 37996, Knoxville, Tennessee, United States

E-mail: pdalhaim@utk.edu

Keywords: Autophagy, Chaperone Mediated Autophagy, Lipid Droplet, Lysosome, Split Intein

Abbreviations: [**CMA**, Chaperone Mediated Autophagy; **LD,** Lipid Droplet; **PLIN2,** Perilipin 2; **LAMP2A**, Lysosome Associated Membrane Protein variant 2A;]

Abstract

Lipid droplets (LDs) are endoplasmic-reticulum-derived neutral lipid storage organelles. An overabundance of LDs in mammalian cells is characteristic of the progression of the metabolic syndromes. Thus, the development of technologies to increase controlled LD breakdown could provide therapy to treat metabolic-associated disorders. Chaperone-mediated autophagy (CMA) plays a key role in LD breakdown. In CMA, LDs are guided to lysosomes where perilipins (PLINs) are degraded so that adipose tissue triglyceride lipase (ATGL) can convert the neutral lipids into free fatty acids for energy or materials for phospholipids. Here, we used a naturally spit intein to target LDs to lysosomes to enhance CMA. DNA constructs were introduced into NIH/3T3 fibroblasts where the C-terminal segment (NpuC) of the split was linked to PLIN2 and the N-terminal segment of the split intein (NpuN) was linked to the lysosomal surface protein LAMP2A. We showed that NpuC-

mCherry-PLIN2/LDs colocalized with LAMP2A-NpuN-GFP/lysosomes in NIH/3T3 fibroblasts. These fibroblasts had a ~4-fold decrease in the number of LDs versus non-transfected control cells and cells expressing a non-cleaving version of the intein system: NpuC(N136A)-mCherry-PLIN2. These results point to the possibility of using technologies to guide entire organelles or protein complexes to lysosomes to control cellular autophagy and upkeep.

4.1 Introduction

Obesity, non-alcoholic fatty liver disease, cardiovascular disease, and type 2 diabetes are in part a consequence of an excessive cellular fraction of neutral lipids, which are sequestered in organelles called lipid droplets (LDs) [54, 55]. Neutral lipids are mostly triacylglyceride ("fat") or cholesterol ester. LDs form from the endoplasmic reticulum but exact mechanisms are lacking [56]. Efforts to treat these metabolic diseases on the cellular scale by inhibiting the acyl-CoA:diacylglycerol acylteransferase (DGAT) enzymes [55], which control the final step of triacylglyceride synthesis. For the purpose of inhibiting LD formation, these are tenuous because mutations in these genes can cause acute diarrhea and death in infant humans [57]. Thus, attention to reducing LD presence in cells has shifted towards increasing LD breakdown (lipolysis) [58]. Lipolysis is a natural process that occurs when cells need energy or materials to synthesize phospholipids. Lipolysis occurs through multiple pathways. Here we focus on lipolysis that occurs via Chaperone Mediated Autophagy (CMA) [30]. During CMA, the heat shock cognate protein of 70 kDa (Hsc70) binds proteins with a pentapeptide sequence/motif on a target protein [59]. In CMA breakdown of LDs, the target protein is Perilipin 2 (PLIN2). PLIN2 is ubiquitously expressed on the surfaces of LDs and is responsible for the maintenance and stability of LDs [60]. Hsc70 guides LD-associated PLIN2 to the lysosome surface where they bind Lysosomal Associated Membrane Protein 2 variant A (LAMP2A), forming a complex [30]. PLIN2 then unfolds, dissociates from the LD, and is

transported across the lysosome membrane [8]. Hsc70 mediated transport of LDs to the lysosome is the rate limiting step in CMA [30]. As PLIN2 breaks down, the neutral lipids in the LD are now accessible to lipases such as cytosolic adipose triglyceride lipase (ATGL), which converts the neutral lipids into free fatty acids and glycerol, although the mechanism is unknown. CMA breakdown of LDs is a stress response because it relies on adenosine monophosphate (AMP) [61]. AMP is a signaler for low energy state in the cell (i.e. starving or nutrient deficiency) and activates AMPK [62]. Once AMPK is activated, it can phosphorylate PLIN2 and which allows Hsc70 binding [61].

We hypothesize that targeting LDs to lysosome will increase LD degradation upon the onset of cellular stress (i.e. starving) and will up regulate CMA. This scheme is depicted in Figure 14A, B. Our goal is to increase the concentration of PLIN2 – which is bound to the LD - at lysosomes whereby locally high concentrations of PLIN2 may increase the activity of Hsc70 and prevent cellular Hsc70 scavenging to detect substrate, resulting in increased LD degradation through CMA.

4.2 Materials and methods

4.2.1 Bacterial Strains, Plasmids and Growth Media

E. coli strain XL1-Blue (*recA1 endA1 gyrA96 thi-1 hsdR17 supE44 relA1 lac [F´ proAB lacIq ZΔM15 Tn10 (Tetr)]*) was used for plasmid construction. Chemically component cells for cloning were prepared by the Inoue method [63] . SOC medium was used for recovery of Inoue cells and Luria-Bertani lysogeny broth (LB) medium was used for growth, transformations, and recovery of frozen storage cultures using standard methods [63] . NaCl, tryptone and yeast extract (DIFCO) were purchased from Fisher Scientific. For plasmid

maintenance, ampicillin (ACROS Organics) was added as appropriate to the media at 200 µg/mL. Cells were grown at 37°C for cloning.

cDNA for mPLIN2 and mLAMP2A was purchased from Sino Biological. All protein fusions were constructed using standard overlap extension with Phusion polymerase (Thermo Scientific; #F530S). All constructs containing NpuC were cloned into pcDNA3.1(+) (Invitrogen; #V79020) between NheI and NotI restriction sites. mLAMP2A-NpuN-eGFP was cloned into pIRES (Clontech; #631605) between XhoI and NotI. This replaced the IRES sequence with the target gene and removed the bicistronic functionality of the vector

pET vectors containing both intein segments were gifted by Dr. David Wood at Ohio State University.

4.2.2 Cell Culture and Treatment

NIH/3T3 fibroblasts (Gift from Dr. Eric Boder at University of Tennessee, Knoxville) were cultured in DMEM media (Corning; #10013CV) supplemented with 10% FBS (Corning; #35010CV) and maintained at 37^{o}C-5%CO_2. All media was filtered through 0.22 mm syringe filters to prevent contamination. Oleic acid (OA) (Fisher; #A195-500) was conjugated to bovine albumin by dissolving 1g of BSA (Sigma; #A8806) in 7mL Tris-HCl pH 9 and adding 26uL of oleic acid. The mixture is then mixed at RT for one hour on an orbital shaker. When a high fat diet was simulated to induce LD production, OA was added to a final concentration of 50 mM. The treatment lasted for 24hr. The cells were then washed (3x) with PBS pH7.4 and serum free DMEM was added to simulate a starved condition for an additional 24hr. Before imaging, the cells were washed once more with PBS and the media was replaced with phenol red free Opti-MEM (Gibco; #11-058-021). For Metformin-HCL treatments, cells were exposed to OA as described above. The media was then

switched to complete media containing 20 mM Metformin-HCL (MP Biomedicals; #0215169101) for 24hrs.

4.2.3 Cell Imaging

All imaging done was live cell on an EVOSfl Digital Inverted Fluorescent Microscope. LD staining was done as previously described with monodansylpentane [64]. Images were captured as JPEGS and edited in ImageJ. Colocation analysis was done with JACoP in ImageJ

4.3 Results and Discussion

4.3.1 A split intein can be used to localize LDs at the lysosome surface

To facilitate targeting of LDs to lysosomes, we used a naturally split intein from *Nostoc Purfuctium DNAe*. This intein was selected based on its high intersegmental affinity (K_d ~1.2 nM) and fast cleaving rate [65]. The two intein segments are referred to here as NpuN and NpuC. Mutations have been made to the intein as previously described to promote C-terminal cleavage as opposed to native splicing activity [66]. NpuN was fused to the C-terminus of LAMP2A and NpuC was fused to the N-terminus of PLIN2 using polymerase chain reaction. Both proteins have been previously reported to be unaffected by tags fused to the stated termini [67]. To determine if the system could be used to target LDs to the lysosome, we first verified both constructs localized to their respective organelles. LAMP2A-NpuN-GFP and the CytoPainter tracker for lysosomes closely overlapped each other (Figure 15A). It should also be noted that expressing LAMP2A-NpuN-GFP alone did not cause a colocalization of LDs and lysosomes (Figure 15B). When the non-cleaving version of NpuC-mCherry-PLIN2 (NpuC(N136A)-mCherry-PLIN2) was expressed alone, it was seen that while NpuC-mCherry-PLIN2 puncta existed at LDs, a significant portion of the protein was also present in the

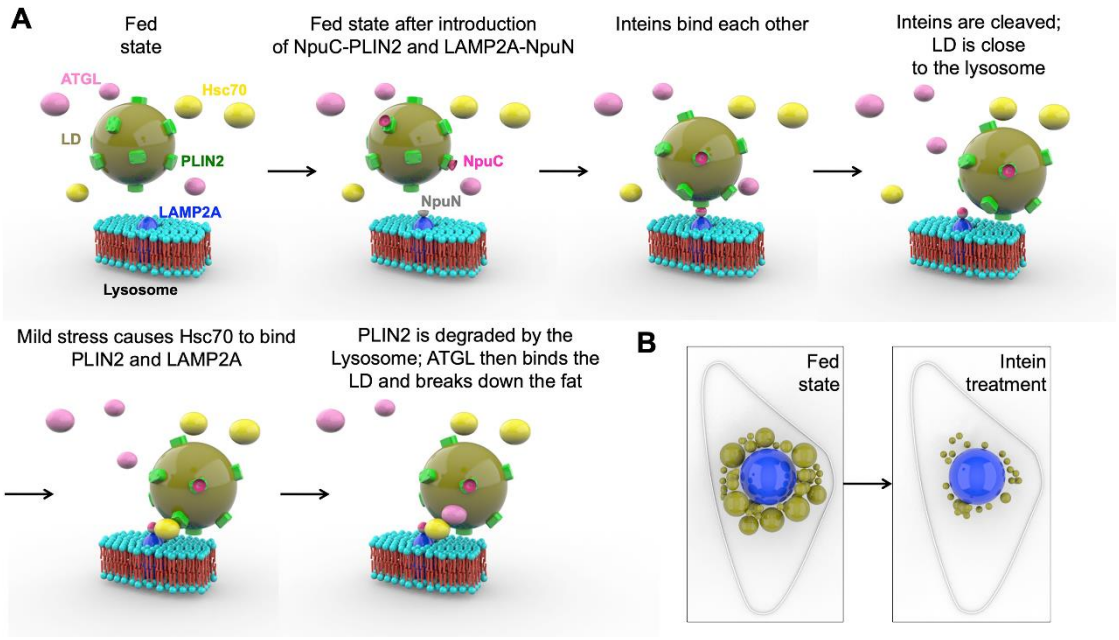

Figure 14. A Schematic illustrating the guidance of LDs to a lysosome with a split intein. (A) NpuC will be fused to the N-terminus of PLIN2 and NpuN will be linked to the C terminus of LAMP2A. This will cause the LD to be guided and subsequently freed near the LD surface. (B) We hypothesis this will result in fewer LDs.

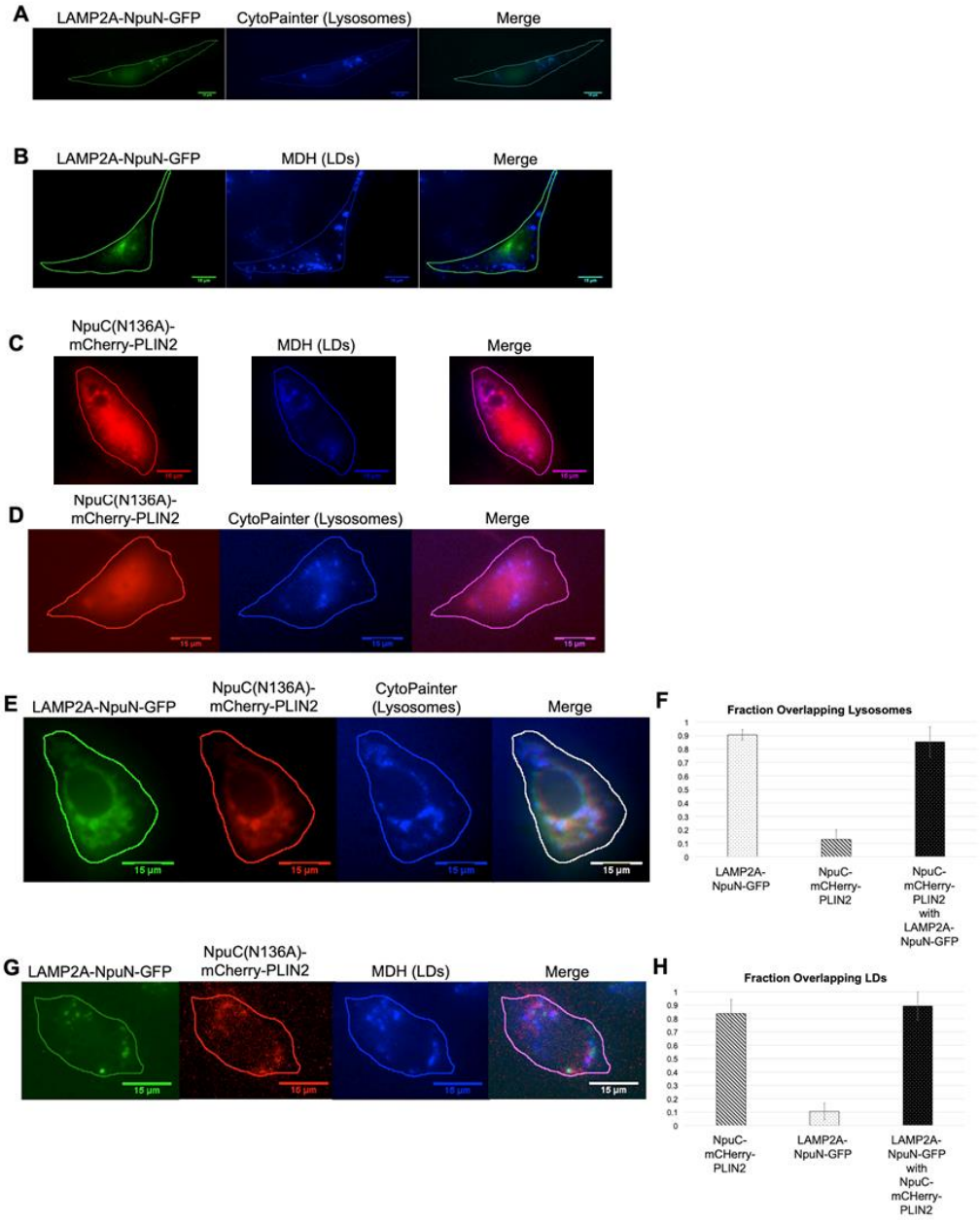

Figure 15. The Npu split intein causes LDs to be localized to lysosomes in NIH/3T3 fibroblasts. (A) NIH/3T3 cells expressing LAMP2A-NpuN-GFP show close overlap with lysosomes dyed with CytoPainter. (B) These cells do not show LDs localized to the lysosomes. (C) NIH/3T3 cells expressing NpuC-mCherry-PLIN2 showed mCherry puncta at LDs while also showing cytoplasmic signals. (D) These cells did not show an overlap between mCherry and lysosomes dyed with CytoPainter. (E) When LAMP2a-NpuN-GFP and NpuC-mCherry-PLIN2 are expressed, GFP and mCherry signals are localized at the lysosome. (F) The same cells also show that LDs are co-localized with LAMP2a-NpuN-GFP and NpuC-mCherry-PLIN2. Expressing the two modules together causes (G) NpuC-mCherry-PLIN2 to localized to lysosomes at the same fraction as LAMP2a-NpuN-GFP and (F) LDs to be overlapping LAMP2a-NpuN-GFP at the same fraction as NpuC-mCherry-PLIN2.

cytoplasm (Figure 15C). This is consistent with previously discussed effects of placing an N-terminal tag on PLIN2 [67]. NpuC(N136A)-mCherry-PLIN2 did not localize to lysosomes (Figure 15D). We then validated that split inteins could be used to target non-cleaving NpuC(N136A)-mCherry-PLIN2 to the lysosomal surface by co-expressing LAMP2A-NpuN-eGFP and NpuC(N136A)-mCherry-PLIN2. This insured mCherry would remain near the lysosome if targeting was successful. The signals from the two proteins overlapped (Figure 15E), signifying NpuC(N136A)-mCherry-PLIN2 was bound to LAMP2A-rich lysosomes. By expressing the two constructs together, we were able to increase the fraction of lysosomes overlapping NpuC(N136A)-mCherry-PLIN2 to comparable levels of the fraction overlapping LAMP2A-NpuN-GFP when singly expressed (Figure 15F). We then moved to see if LDs and lysosomes, could be targeted to each other with our split intein system. To do this, we expressed NpuC-mCherry-PLIN2 and LAMP2A-NpuN-GFP with oleic acid supplemented media to simulate a high fat diet. This will force the synthesis of TAG and promote the formation of LDs. Again, the NpuC intein was non-cleaving. We saw close overlap between the two fluorescent proteins and a LD dye (Figure 15G). Nearly all LDs appeared near the lysosome whereas cells expressing only LAMP2A-NpuN-GFP appear to have evenly distributed LDs. This is illustrated by the fractional signal overlap increase between LDs and LAMP2A-NpuN-GFP in cells expressing just LAMP2A-NpuN-GFP versus LAMP2A-NpuN-GFP and NpuC-mCherry-PLIN2 (Figure 15H). Our technology's ability to target organelles and protein complexes and guide them to lysosomes for degradation, may have many applications reaching beyond this work.

4.3.2 Lipid Droplets localized to the lysosome via the Npu split intein are degraded at a faster rate

To test the inteins' ability to increase LD degradation we used the cleaving variant – NpuC - over the noncleaving - NpuC(N136A). In CMA, LAMP2A must bring the target protein across the lysosomal surface for degradation. We hypothesize that the force generated by LAMP2A during the transmembrane step of CMA is not strong enough to overcome a strong association between PLIN2 on the LD, and LAMP2A in the lysosome membrane. Our hypothesis details that a bond between LAMP2A and PLIN2 will prevent transport across the lysosomal surface, thus preventing the occurrence of CMA. This led us to use the cleaving intein. A cleaving intein yields two protein elements that are close in spatial proximity but not physically or chemically linked. A split cleaving intein will cause the LD to be localized and then freed near the lysosomal surface to circumvent this.

NIH/3T3 fibroblasts expressing neither LAMP2A-NpuN-GFP nor NpuC-mCherry-PLIN2 and cells expressing LAMP2A-NpuN-GFP and the non-cleaving version of NpuC – NpuC(N136A)-mCherry-PLIN2– had ~4-fold more LDs than cells expressing the cleaving intein system - LAMP2A-NpuN-GFP and NpuC-mCherry-PLIN2 (Figure 16A-D). This may suggest that the translocation that the LAMP2A trimer preforms during CMA isn't strong enough to overcome the interaction between the intein segments. Though this hasn't been confirmed, it shows that intein technology may be ideal versus other methods, such as protein-peptide affinity pairs, for targeting molecular bodies to the lysosome to promote increased degradation through the CMA pathway. It is imperative that the tool used to attract the LD to the lysosome also has an "off" step. A technology that brings these organelles together in a permanent state will not yield an increase in LD degradation.

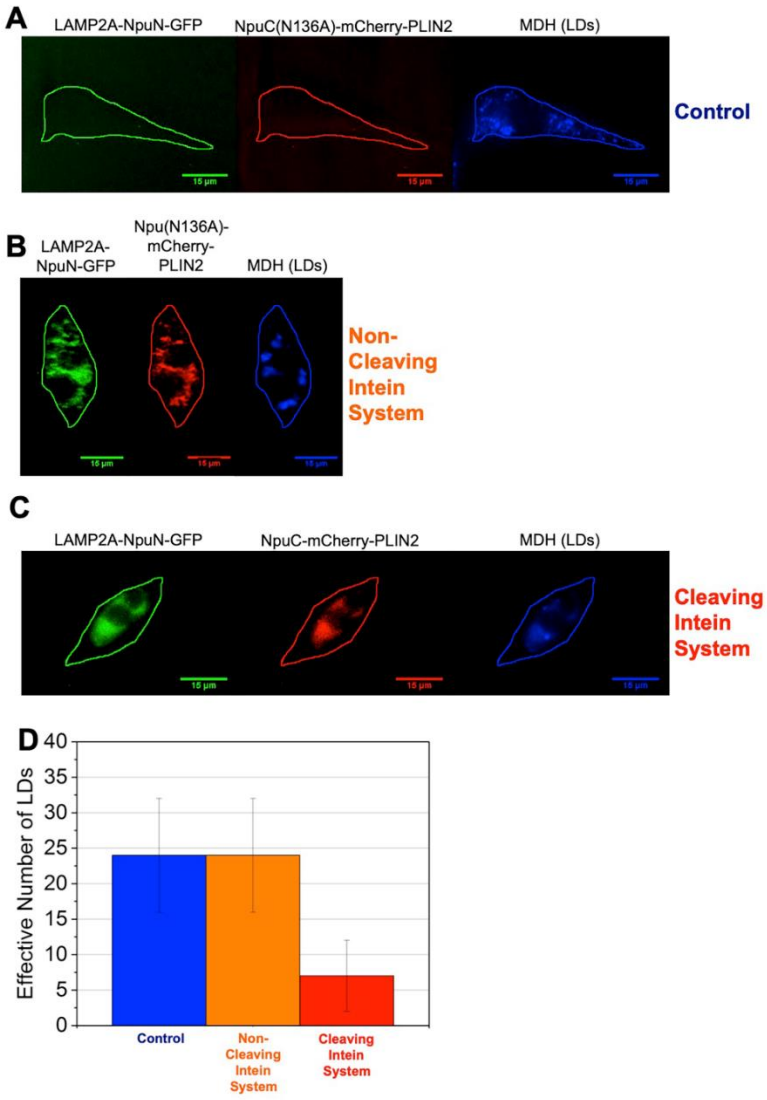

Figure 16. LD numbers are reduced with the cleaving intein system, but not the non-cleaving intein system in NIH/3T3 fibroblasts. (A) Fluorescence micrographs of fibroblasts that are not expressing LAMP2A-NpuN-GFP or NpuC(N136A)-mCHerry-PLIN2. (B) Fluorescence micrographs of fibroblasts that are expressing LAMP2A-NpuN-GFP and NpuC(N136A)-mCHerry-PLIN2. (C) Fluorescence micrographs of fibroblasts that are expressing LAMP2A-NpuN-GFP and cleaving NpuC-mCHerry-PLIN2. (D) Plot of the number of effective lipid droplets in the cells in A-C. N = 20 cells for each column.

4.3.3 A Truncated Split Intein Can be used to control the degradation rate of Lipid Droplets

Lipotoxicity from the free fatty acids of triacylglyceride is a concern when LDs are broken down. In an effort to prove that our system can break down some but not all the LDs in fibroblasts, we truncated the first 6 amino acids of NpuC (IKIATR) using PCR. This has previously been shown to decrease the affinity of the intein segments while maintaining activity [68]. We found that while this led to a higher number of LDs than the full length intein (15 versus 8), it was still effective in decreasing LD number (Figure 17A,B). This shows that in applications where high levels of lipolysis are not desired, the system can be tuned to generate the amount of LD degradation desired.

4.3.4 Lipid Droplet degradation can be triggered with chemical activation

We also investigated the ability to trigger LD breakdown on command without the need for a stress-induced reaction (i.e. starvation to induce AMPK activity). We used a known AMPK activator, Metformin-HCl [69]. AMPK phosphorylates PLIN2 before it binds Hsc70. Metformin was selected because it is approved for therapeutic use in humans.

An LD synthesis period in oleic acid-based media and sequential treatment with Metformin-HCl resulted in similar results as starvation (Figure 17D-F). This suggests our system of LD degradation is possible to trigger on demand and may be useful in selectively degrading other CMA substrates.

4.4 Conclusion

In conclusion, a split intein was used to localize LDs near the lysosome. After the onset of stress, this caused a rapid degradation of LDs. Through both manipulation of the intein and chemical measures, we have proved this system allows controllable degradation of LDs.

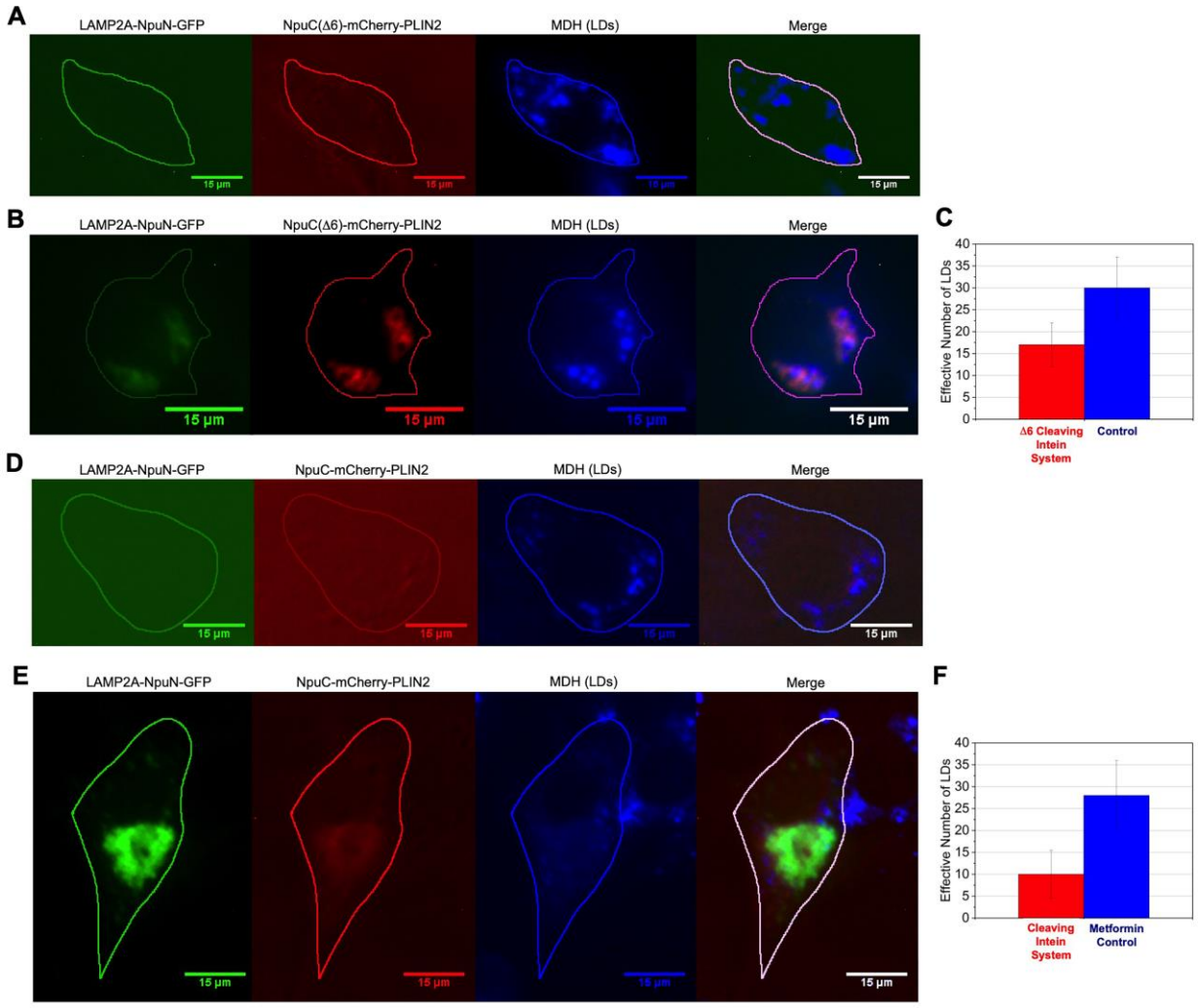

Figure 17. Enhanced split intein mediated LD degradation is controllable with both system modification and chemical activation in NIH/3T3 fibroblasts. (A) Fluorescence micrographs of fibroblasts that are not expressing LAMP2A-NpuN-GFP or NpuC(D6)-mCHerry-PLIN2. (B) Fluorescence micrographs of fibroblasts that are expressing LAMP2A-NpuN-GFP and NpuC(D6)-mCHerry-PLIN2. (C) Plot of the effective number of LDs in cells in (B) versus (C). N = 20 cells for each column. (D) Fluorescence micrographs of fibroblasts that have been exposed to 20 mM Metformin-HCl for 24hrs. (E) Fluorescence micrographs of fibroblasts that are expressing LAMP2A-NpuN-GFP and NpuC-mCHerry-PLIN2 cells that have been exposed to 20 mM Metformin-HCl for 24hrs. (F) Plot of the number of effective LDs in the cells represented in (D) versus (F). N = 20 cells for each column.

Importantly, this technology modulated an existing pathway, CMA. CMA is implicated in aging and its related disorders such as cancer and Alzheimer's Disease. Our technology may prove useful in treating these diseases.

References

1. Walther, T.C. and R.V. Farese, Jr., *The life of lipid droplets.* Biochim Biophys Acta, 2009. **1791**(6): p. 459-66.
2. Yen, C.L., et al., *Thematic review series: glycerolipids. DGAT enzymes and triacylglycerol biosynthesis.* J Lipid Res, 2008. **49**(11): p. 2283-301.
3. Meyers, A., T.M. Weiskittel, and P. Dalhaimer, *Lipid Droplets: Formation to Breakdown.* Lipids, 2017. **52**(6): p. 465-475.
4. Haas, J.T., et al., *DGAT1 mutation is linked to a congenital diarrheal disorder.* J Clin Invest, 2012. **122**(12): p. 4680-4.
5. Twilley, N., *A Pill to Make Exercise Obsolete*, in *The New Yorker*. 2017: Print.
6. Kaushik, S. and A.M. Cuervo, *Degradation of lipid droplet-associated proteins by chaperone-mediated autophagy facilitates lipolysis.* Nat Cell Biol, 2015. **17**(6): p. 759-70.
7. Chiang, H.L., et al., *A role for a 70-kilodalton heat shock protein in lysosomal degradation of intracellular proteins.* Science, 1989. **246**(4928): p. 382-5.
8. Tsai, T.H., et al., *The constitutive lipid droplet protein PLIN2 regulates autophagy in liver.* Autophagy, 2017. **13**(7): p. 1130-1144.
9. Kaushik, S. and A.M. Cuervo, *AMPK-dependent phosphorylation of lipid droplet protein PLIN2 triggers its degradation by CMA.* Autophagy, 2016. **12**(2): p. 432-8.
10. Zhang, Y.L., et al., *AMP as a low-energy charge signal autonomously initiates assembly of AXIN-AMPK-LKB1 complex for AMPK activation.* Cell Metab, 2013. **18**(4): p. 546-55.

11. Sambrook, J., *Molecular cloning : a laboratory manual / Joseph Sambrook, David W. Russell*, ed. D.W. Russell and L. Cold Spring Harbor. 2001, Cold Spring Harbor, N.Y: Cold Spring Harbor Laboratory.
12. Yang, H.J., et al., *Monodansylpentane as a blue-fluorescent lipid-droplet marker for multi-color live-cell imaging.* PLoS One, 2012. **7**(3): p. e32693.
13. Shah, N.H., et al., *Naturally split inteins assemble through a "capture and collapse" mechanism.* J Am Chem Soc, 2013. **135**(49): p. 18673-81.
14. Guan, D., M. Ramirez, and Z. Chen, *Split intein mediated ultra-rapid purification of tagless protein (SIRP).* Biotechnol Bioeng, 2013. **110**(9): p. 2471-81.
15. Orlicky, D.J., et al., *Multiple functions encoded by the N-terminal PAT domain of adipophilin.* J Cell Sci, 2008. **121**(Pt 17): p. 2921-9.
16. Wong, S., A.A. Mosabbir, and K. Truong, *An Engineered Split Intein for Photoactivated Protein Trans-Splicing.* PLoS One, 2015. **10**(8): p. e0135965.
17. Karise, I., et al., *Liver and Metformin: Lessons of a fructose diet in mice.* Biochim Open, 2017. **4**: p. 19-30.

Chapter 5 Conclusions and Recommendations

As a whole, the use of nanoparticles in medicine had seemed to hit a plateau in recent years. In almost forty years of development, there are still only 32 FDA approved nanoparticles therapies. This is bound to change after the large-scale use of liposomal nanoparticles in the global rollout of both the Pfizer and Moderna Covid-19 vaccines. It is likely the interest in nanoparticle-based drug delivery will be rejuvenated.

To use a nanoparticle in the clinic, it is important to know what cells natively remove the NPs from circulation and the mechanisms at play. This gives insight into how the NP can be used, especially if targeting is planned. Any native interactions must be overcome with targeting. I have described a novel interaction between PEGylated CNPs and SR-BI. This was confirmed to be valid with both *in vitro* and *in vivo* experimentation.

Potential increased use further creates the need to accurately predict how NPs will behave in a representative patient population. With the work presented here, I have shown that using obese mice in pre-clinical trials has vastly different outcome than using lean animals. While the fatty liver is common thought to have decreased over all activity, I have shown that CNPs are localized to the liver at an increased rate. This is because the fatty liver is comprised mostly of fatty deposits in misshapen hepatocytes and macrophages. I have shown that this can have different effects for different NPs. This needs to be effectively studied for each NP proposed for market.

The in future, the interplay because SR-BI needs to be further studied. My work has shown that obesity is leading to an increased expression level of SR-BI. This could be directing

CNP to the liver, but a double leptin/SR-BI knockout mouse should be generated to investigate this further. The PK profile of an obese SR-BI deficient mouse would give further insight into the driving force.

Attempts should be made to see if targeting strategies can be used to overcome the increased localization of CNPs to the liver. If CNPs will always be removed from the circulation at an increased rate in obese patients, they will have limited applications in the clinic.

Vita

Mitchell Raith earned his Bachelor of Science in Chemical Engineering from the Ohio State University in Columbus, OH during the Spring of 2017. During his undergraduate studies, he conducted research in the lab of Dr. David Wood. His research focused on purifying tagless and traceless protein for therapeutic use via a split intein system. After completing his B.S., Mitchell moved to Knoxville to pursue a PhD in Chemical and Biomolecular Engineering at the University of Tennessee. He joined Dr. Paul Dalhaimer's group in July of 2017 where his research was focused on better understanding soft nanoparticle drug delivery systems.